DESIGN AND DEVELOPMENT OF HIGH-EFFICIENCY CdS/CdTe THIN-FILM SOLAR CELLS BY ENHANCING ABSORPTION AND MINIMIZING RECOMBINATION

Janith Randima Wijesingha

218072V

Master of Philosophy

Department of Electrical Engineering
Faculty of Engineering

University of Moratuwa
Sri Lanka

December 2023

DESIGN AND DEVELOPMENT OF HIGH-EFFICIENCY CdS/CdTe THIN-FILM SOLAR CELLS BY ENHANCING ABSORPTION AND MINIMIZING RECOMBINATION

Janith Randima Wijesingha

218072V

Thesis/Dissertation submitted in partial fulfillment of the requirements for the degree

Master of Philosophy in Electrical Engineering

Department of Electrical Engineering

Faculty of Engineering

University of Moratuwa

Sri Lanka

December 2023

DECLARATION

I declare that this is my own work, and this thesis/dissertation does not incorporate without acknowledgement any material previously submitted for a degree or diploma in any other University or Institute of higher learning and to the best of my knowledge and belief it does not contain any material previously published or written by another person except where the acknowledgement is made in the text. I retain the right to use this content in whole or part in future works (such as articles or books).

Signature: Date: 01/09/2024

The above candidate has carried out research for the PhD/MPhil/Masters' thesis/dissertation under my supervision. I confirm that the declaration made above by the student is true and correct.

Name of Supervisor: …….. Date: 03/09/2024

Dr. R.M. Thushara Damayanthi

Name of Supervisor: …….. Date: 03/09/2024

Prof. Indika De Silva

ACKNOWLEDGEMENT

I would like to express my heartfelt gratitude to the individuals and organizations who have generously contributed to the successful completion of my thesis. Without their assistance, this journey would have been much more challenging.

First and foremost, I am deeply grateful to extend my sincere appreciation to my esteemed supervisors, Dr. R.M. Thushara Damayanthi (Department of Electrical Engineering, University of Moratuwa, Sri Lanka) and Prof. Indika De Silva (Department of Materials Science and Engineering, University of Moratuwa, Sri Lanka). Their mentorship, expertise, and continuous support have been instrumental in shaping this research and its outcomes.

I extend my special thanks to Professor D.S.M De Silva (Department of Chemistry at the University of Kelaniya) and Ms. Udani Gajanayake (Department of Chemistry at the University of Kelaniya) for their invaluable assistance in providing laboratory resources and equipment. Their generosity in facilitating crucial experiments and hands-on experience greatly contributed to the success of this study.

I am deeply grateful to Dr. Imalka Jayawardhane and Mr. Vinura Wickramasinghe from the Department of Computer Science and Electronic Engineering at the University of Surrey, United Kingdom. Their assistance in obtaining vital measurements for my samples, especially in a context where such facilities are limited in Sri Lanka, was pivotal to the progress of my research.

I would like to express my sincere appreciation to the Senate Research Grant of the University of Moratuwa under the grant number SRC/LT/2021/08 that financial support made it possible for me to undertake this study.

Finally, I extend my heartfelt thanks to my beloved parents and my dear wife for their understanding, unwavering encouragement, and constant support throughout this journey. Your love and patience were crucial in making this project a success.

ABSTRACT

Second-generation solar cells, known as thin-film solar cells, have emerged as promising alternatives to traditional silicon-based first-generation photovoltaic cells. As the solar cell arrangement, superstrate configuration is the widely used structure for constructing thin-film solar cells. Nevertheless, less broadband light absorption due to light reflection from the front cover glass surface and carrier recombination at absorber layer back surface mainly contributes to less performance in thin-film solar cells. Herein, ZnO anti-reflection (AR) coating was introduced using spin coating technique on glass/FTO/CdS/CdTe/Cu/Au substrate to enhance the power conversion efficiency of the solar cell through reduction of front surface reflectance. The ZnO layer deposited at 3000 rpm in 15 s showed the minimum reflectance and higher transmittance over the 500-900 nm wavelength region. Further, the thickness of the optimal condition film was 63.32 nm, which was compatible with the ideal theoretical AR coating thickness of 65 nm. Comparing the device performances of the CdS/CdTe solar cell with AR coating and without AR coating, all tested devices have shown an average short circuit current density improvement of 6.7%, and the overall power conversion efficiency enhancement of 9%. Furthermore, a simulation study for CdTe solar cells was conducted using parameters of laboratory-developed solar cells. The variation between simulated and experimental data was discussed. Subsequently, to mitigate recombination at the back surface, the study suggested a solution: the introduction of a SnS back surface field (BSF) layer between the absorber layer and the back contact layer. This investigation was carried out using the SCAPS-1D simulation platform. According to the results obtained, the average power conversion efficiency was improved by 38%. Moreover, the simulation suggested that this approach could reduce the thickness of the CdTe layer, subsequently lowering manufacturing costs.

Keywords: AR coating, BSF layer, CdS/CdTe solar cell, SCAPS-1D, Spin coating

TABLE OF CONTENTS

Declaration i

Acknowledgement ii

Abstract iii

Table of Contents iv

List of Figures vii

List of Tables x

List of Abbreviations xi

Chapter 1 1

INTRODUCTION 1

1.1. Global Energy Demand 2

1.1.1 Direction of energy sector in Sri Lanka 3

1.2. Solar energy 3

1.2.1. Solar Spectrum 4

1.2.2. Air Mass (AM) index 5

1.3. Photovoltaic (PV) cells 6

1.3.1 First generation 6

1.3.2 Second generation 7

1.3.3 Third generation 8

1.3.4 Fourth generation 8

1.4. Theoretical Background of photovoltaic solar cells 9

1.4.1 Theory of p-n junction and photogeneration 9

1.4.2 Surface recombination in a solar cell 10

1.4.3 Fill Factor (FF) and power conversion efficiency 11

1.4.4 Quantum efficiency (QE) and power conversion efficiency (PCE) 12

1.5. Introduction of Anti-reflection (AR) coating on solar cell 13

1.5.1 Theory of AR coating design 13

1.5.2 Literature review on AR coatings 15

1.6 Introduction of back surface field layer (BSF) on solar cell 21

1.6.1 Theory of BSF design 21

1.6.2 Review on BSF layer 22
1.7 Characterization technique 24
1.7.1 Optical properties (UV-visible spectroscopy, Bentham EQE setup) . 25
1.7.2 Thickness variation (Profilometry) 28
1.7.3 Composition analysis (EDX) 30
1.7.4 Surface analysis (AFM) 31
1.7.5 I-V measurements (Solar simulator) 32
1.8 Aim of the present study 32
1.8.1 Overview 32
1.8.2 Objectives 33
Chapter 2 34
FABRICATION OF SPIN-COATED ZnO AR COATING FOR CdS/CdTe SOLAR CELLS 34
2.1 Introduction 34
2.2 Design of single layer ZnO AR coating 35
2.3 Materials and methodology 37
2.3.1 Fabrication of ZnO layer using zinc oxide powder as zinc precursor 38
2.3.2 Fabrication of ZnO layer using zinc acetate as zinc precursor 39
2.4 Characterization 41
2.5 Results and discussion 42
2.5.1 The theoretical background of the formation of the ZnO 42
2.5.2 Optical properties 42
2.5.3 Variation of AR coating thickness 46
2.5.4 Surface analysis 47
2.5.5 Composition analysis 47
2.5.6 Device characterization (IV measurements) 48
2.6 Summary 49
Chapter 3 50
IMPROVEMENT OF CdS/CdTe SOLAR CELL'S PERFORMANCE USING SIMULATION STUDY 50
3.1 Introduction 50
3.2 Device and Simulation 50

3.2.1. SCAPS-1D simulation software 50
3.2.2. Data collection and executing the simulation 51
3.3 Results and Discussion 54
3.3.1 Numerical investigation of the laboratory developed CdS/CdTe solar cell 54
3.3.2 Influence of the absorber layer thickness on the device performance. 56
3.3.3 Introduction of SnS BSF layer for CdS/CdTe solar cell 57
3.4 Summary 61
Chapter 4 62
CONCLUSIONS 62
References 64

LIST OF FIGURES

Figure	Description	Page
Figure 1.1	Classification of energy sources	1
Figure 1.2	(a) Global energy demand by sources and (b) Precent of primary energy	2
Figure 1.3	The spectrum of solar radiation.	4
Figure 1.4	Representation of the different solar spectrums	5
Figure 1.5	The best recorded laboratory level power conversion efficiencies	6
Figure 1.6	(a) p-n junction before the diffusion (b) After equilibrium state	9
Figure 1.7	Energy band diagram of the solar cell	10
Figure 1.8	(a) Dangling bonds at the surface of the semiconductor (b) Recombination of electrons and holes at the surface	10
Figure 1.9	J-V characteristic of a solar cell	11
Figure 1.10	Structure of a solar cell with AR coating	13
Figure 1.11	(a) Reflection of light at top and bottom surfaces of the AR coating (b) Destructive interference between reflected beams	13
Figure 1.12	Reflectance spectrum obtained from PC1D simulation	15
Figure 1.13	Reflectance Spectrums (a) using theoretical equation and (b) using PC1D simulation	16
Figure 1.14	Structure of a solar cell with BSF layer	20
Figure 1.15	Arrangement of the band diagram of solar cell with BSF layer	21
Figure 1.16	Material and device characterization techniques	24
Figure 1.17	Schematic diagram of an UV-visible spectrophotometer	25
Figure 1.18	Tauc plot	26
Figure 1.19	Configuration of the DTR6 integrating sphere	27
Figure 1.20	Schematic diagram of SEM	28

Figure 1.21	Average thickness measurement from profilometry	28
Figure 1.22	The structure of profilometry	29
Figure 1.23	Phenomena of emitting electrons	30
Figure 1.24	The operation modes of AFM	30
Figure 2.1	(a) The structure of the solar cell and (b) the visual image of the solar cell	33
Figure 2.2	CdS/CdTe solar cell structure with AR coating	34
Figure 2.3	Absorbance spectrum of CdS and solar irradiance spectrum	35
Figure 2.4	Reflectance spectrum of CdS/CdTe solar cell with and without ZnO AR coating	36
Figure 2.5	The solubility of ZnO powder in various alcohols	37
Figure 2.6	ZnO Coating Deposited on Glass Substrate at various spin rates	37
Figure 2.7	The case of low $Zn(CH_3COO)_2$ concentration	38
Figure 2.8	The case of uniform ZnO layer	39
Figure 2.9	Optical absorbance vs. wavelength plot of the ZnO coatings at three different spin rates	39
Figure 2.10	The case of uniform ZnO layer due to higher solution drop height	40
Figure 2.11	Optical transmittance vs. wavelength plot of the ZnO AR coatings (S1 to S6)	42
Figure 2.12	(a) Absorbance vs wavelength plot and (b) Tauc plot for the ZnO AR coatings S1 to S6	42 43
Figure 2.13	Reflectance vs. wavelength plot of the ZnO AR coatings S1 to S6	44
Figure 2.14	Thickness of the ZnO AR coating vs. spin rate of deposition	44
Figure 2.15	**(a)** 3D and **(b)** 2D AFM images of ZnO surface deposited at 3000 rpm	45
Figure 2.16	J-V curves for the devices 1, 2 and 3	46 – 47
Figure 3.1	Thickness measurement of FTO/CdS/CdTe solar cell	50

Figure 3.2	Tauc plot of CdS	51
Figure 3.3	Tauc plot of CdTe	51
Figure 3.4	Software interpretation of the laboratory-developed solar cell	52
Figure 3.5	J-V characteristics curve for simulated and experimental CdS/CdTe solar cells	54
Figure 3.6	The cell performance on the energy band gap of the CdTe absorber layer	54
Figure 3.7	The performance of the device with the thickness of the CdTe absorber layer	55
Figure 3.8	Variation of quantum efficiency (QE) of the device w.r.t CdTe thickness	56
Figure 3.9	Software interpretation of the solar cell with BSF layer	57
Figure 3.10	J-V characteristic curves of reference structure and solar cell with BSF layer	57
Figure 3.11	The recombination current curves of reference structure and the solar cell with BSF layer	58
Figure 3.12	The performance of the proposed solar cell with the thickness of the CdTe absorber layer	58

LIST OF TABLES

Table	Description	Page
Table 2.1	Sample labeling with respect to the spin rate	40
Table 2.2	The energy band gap of the sample s1 to s6 w.r.t spin rate	43
Table 2.3	Minimum reflectance with corresponding wavelength of the samples s1 to s6	45
Table 2.4	Composition of ZNO sample grown on FTO/glass substrate	46
Table 2.5	Electrical properties of the device 1, 2 and 3	48
Table 2.6	Comparison of the performance of the devices	48
Table 3.1	Layer parameters	52
Table 3.2	Comparison of reference and proposed solar cell with respect to the CdTe thickness	58
Table 3.3	Enhancement of the electrical parameters of proposed solar cell with respect to the reference cell	59

LIST OF ABBREVIATIONS

Abbreviation	Description
AFM	Atomic Force Microscope
AM	Air Mass
AMPS-1D	Analysis of Microelectronic and Photonic Structures in 1 Dimension
AR	Anti-Reflection
a-Si:H	Amorphous Silicon
BSF	Back Surface Field
CBD	Chemical Bath Deposition
CdS	Cadmium Sulfide
CdTe	Cadmium Telluride
CEB	Ceylon Electricity Board
CIGS	Copper Indium Gallium Selenide
CVD	Chemical Vapor Deposition
DSSC	Dye-sensitized Solar Cell
EDX	Energy dispersive X-ray
EQE	External Quantum Efficiency
ETL	Electron Transparent Layer
FF	Fill Factor
GHG	Greenhouse Gas
IEA	International Energy Agency
I_{MP}	Current at Maximum Power Point
IQE	Internal Quantum Efficiency
I_{SC}	Short Circuit Current
I-V	Current-Voltage
J_{SC}	Short Circuit Current Density
LECO	Lanka Electricity Company (Private) Limited
LED	Light Emitting Diodes
LPD	Liquid Phase Deposition
MPM	Molecular Precursor Method

NDC	Nationally Determined Contributions
NSSP	Numerical Solar Cell Simulation
NZE	Net Zero Emissions by 2050 Scenario
PC1D	Personal Computer One-dimensional
PCE	Power Conversion Efficiency
PECVD	Plasma-Enhanced Chemical Vapor Deposition
P_{MP}	Power at Maximum Power Point
PSC	Perovskite Solar Cell
PV	Photovoltaic
PVD	Physical Vapor Deposition
QE	Quantum Efficiency
QDSSC	Quantum Dot Solar Cell
RF	Radiofrequency
RMS	Root Mean Square
RPM	Round Per Minute
R_s	Series Resistance
R_{sh}	Shunt Resistance
SEM	Scanning Electron Microscopy
SCAPS-1D	Solar Cell Capacitance Simulator in One-dimension
SnS	Tin Sulfide
SLSEA	Sri Lanka Sustainable Energy Authority
TSC	Tandem Solar Cell
UV	Ultraviolet
V_{OC}	Open Circuit Voltage
V_{MP}	Voltage at Maximum Power Point
XRD	X-ray Diffraction
XPS	X-ray Photoelectron Spectroscopy
ZnO	Zinc Oxide

CHAPTER 1

INTRODUCTION

Energy is a fundamental concept that plays a crucial role in human day-to-day lives. The basic concept of energy can be defined as “it cannot be created or destroyed, but can transform from one form to another”. Regarding energy sources, those are the places or things we get energy from and contribute to the world’s energy supply. Energy exists in various forms, each playing a crucial role in different processes and systems. The seven forms of energy are mechanical, thermal (heat), chemical, electrical, nuclear, radiant (light), and sound energy. These fundamental forms can be classified further into primary and secondary energy sources.

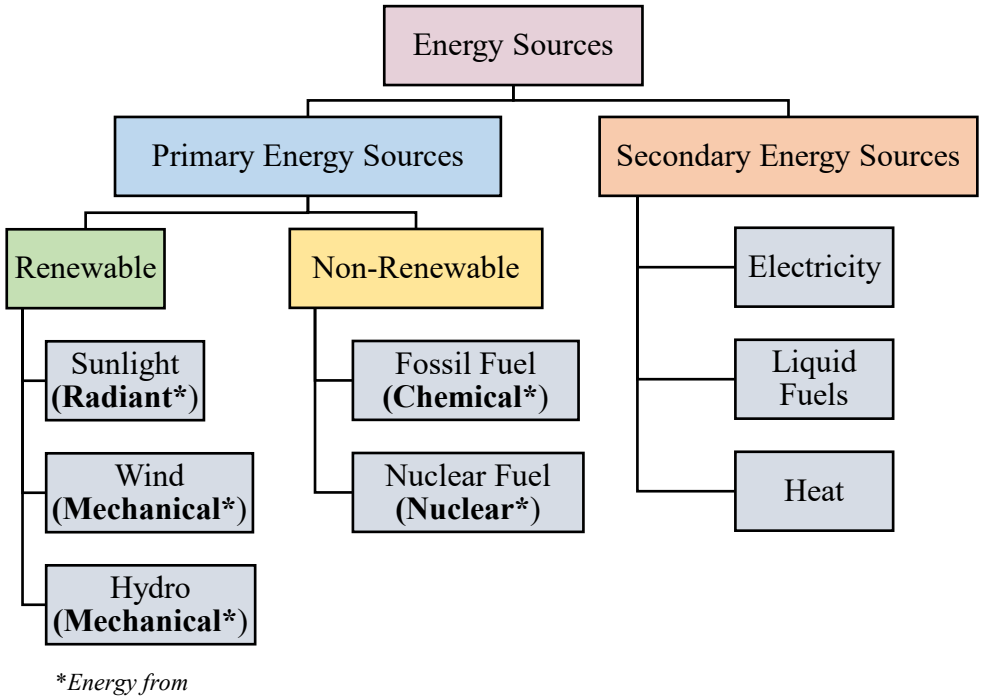

Fig. 1.1: Classification of energy sources [1], [2]

Fig. 1.1 shows the classification of energy sources. Primary energy sources are natural resources that can be found in the environment. These sources are needed for further conversion to make more usable and accessible forms of energy. Therefore, secondary energy sources are the forms of energy that result from converting primary energy sources. Primary energy sources can be categorized according to their renewable or non-renewable nature, determined by the time required for their regeneration. Among them, renewable energy sources can be naturally recreated over time. Moreover, they are considered as sustainable forms of energy. In contrast, non-renewable energy sources are finite and will eventually be exhausted over time. Moreover, fossil fuels contribute significantly to global warming and current commercial nuclear fission technology relies on solid fuel rods and water-cooled systems, which have low fuel efficiency and carry substantial risks of nuclear meltdown disasters.

At present, electricity consumption is increasing rapidly worldwide due to population growth, economic development, technological advancement, urbanization, and changing lifestyles. Hence, most countries search for other energy approaches to access the increasing demand through more sustainable and environmentally friendly energy sources. Among them, harnessing the sun's energy and converting it into electricity has proven to be one of the promising solutions.

1.1. Global Energy Demand

According to the report released on August 28th 2023 [3], by ExxonMobil, which is continually studying global energy demand, global demand will increase from 15% by 2050 compared to 2021. A growing population, economic revolution, and technological development mainly cause this. Electricity generation would be the largest and fastest-growing sector contributing to the upcoming energy demand. Fig. 1.2 illustrates the contribution of the energy sources to global energy demand and the percentage contribution between 2000-2050.

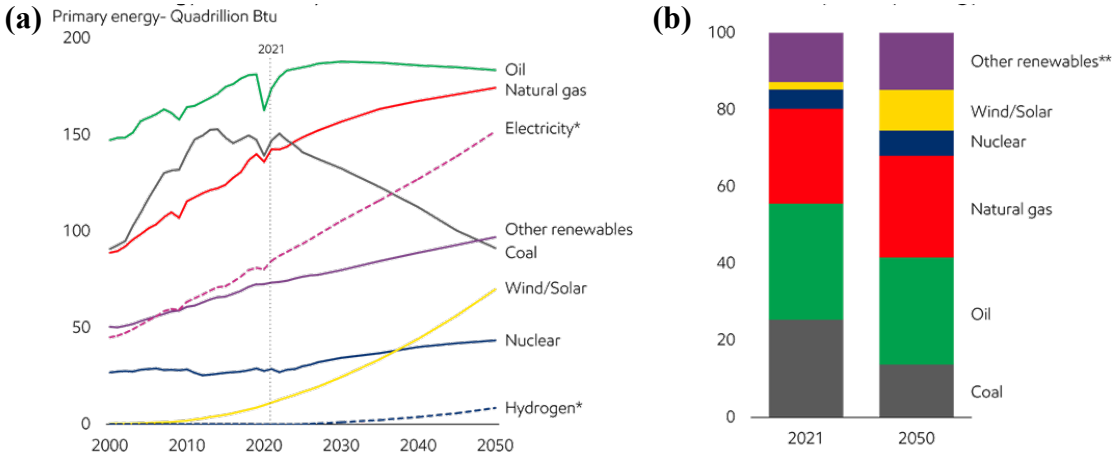

Fig. 1.2: (a) Global energy demand by sources and **(b)** Precent of primary energy. Adapted from [3]

Compared to other energy sources, renewables and nuclear show a 70% increment to meet the demand growth by 2050. At present, coal is still used as a major energy source in developing countries such as Sri Lanka. However, it will drop below 15% by 2050 because developed nations such as China shift towards low-emission energy sources such as nuclear and renewables.

According to the world energy outlook, 2022 [4], published by the International Energy Agency (IEA), per year total electricity generation will be improved by 3.3% by 2050. In 2021, annual renewable energy capacity additions are 290 GW and it will quadruple around 1 200 GW by 2030. Furthermore, according to IEA, the Net Zero Emissions by 2050 Scenario (NZE) would accelerate the lower carbon solutions, such as renewables, while reducing fossil fuels. Therefore, it predicts that investment in clean energy, such as solar photovoltaic (PV), will improve to nearly 4% by 2030. Among investments in clean energy sources, solar PV is the least costly option for

most countries. In 2022, an increase in solar PV generation was recorded as 270 TWH (26% improvement) and that growth surpassed wind generation for the first time in history. Moreover, global installed capacity of concentrating solar thermal power (CSP) increased by 200 MW in 2022 to reach a total of 6.3 GW [5].

Therefore, solar PV technologies will assume a significant role in meeting the world's growing energy needs.

1.1.1 Direction of energy sector in Sri Lanka

Energy demand is primarily fulfilled by three primary sources: hydropower, fossil fuels (coal and fuel oil), and renewable energy sources (solar and wind power) in Sri Lanka. According to the annual report of the Sri Lanka Sustainable Energy Authority, the energy balance in 2019 [6], petroleum continued to dominate the primary energy supply, with a share of 44%, while renewable energy accounts for 11%. Moreover, in 2019, electricity generation was 16,762.3 GWh, which mainly (about 66%) contributed from thermal power plants. Consequently, the unit price of energy rose as electricity demand in Sri Lanka increased. Utilizing renewable energy sources can be the solution to lowering these costs.

Nevertheless, according to the Nationally Determined Contributions (NDC) registry [7], Sri Lanka has promised to reduce Greenhouse Gas (GHG) that contributes to global warming by 14.5% by 2030. Furthermore, Sri Lanka aims to reach carbon neutrality by 2050. Since electricity generation is one of the contributor, Sri Lanka has also opted against expanding the capacity of coal-fired power plants any further, as part of this commitment. Therefore, it is required to enhance the renewable energy contribution to the energy market in Sri Lanka.

However, solar power is one of the most preferable sources for Sri Lanka due to the abundance of sunlight. Therefore, according to the project “Battle for Solar Energy” [8] conducted by Ceylon Electricity Board (CEB), Lanka Electricity Company (Private) Limited (LECO), and Sri Lanka Sustainable Energy Authority (SLSEA), The goal is to incorporate 1000 MW of solar power into the national grid by 2025, with an additional 1500 MW to follow by 2030.

In conclusion, not only in Sri Lanka but also worldwide, solar PV will become one of the major sources of power. Therefore, continuous efforts should be taken to manufacture alternative, highly efficient photovoltaic devices while lowering the cost of manufacturing.

1.2. Solar energy

Solar power, acknowledged as the most abundant and potent energy source globally, remains a trustworthy form of energy and harnessed through the use of PV cells, which convert sunlight directly into electricity. Its utilization carries minimal environmental risks, making it an environmentally friendly choice alongside with proper material life cycle management system. Note that several references such as “First Solar's

Recycling Program" [9] highlight successful recycling of PV materials including toxic elements from thin film solar cells.

In the solar PV cell design and development field, knowledge of the solar spectrum is more significant. Different photovoltaic materials have varying spectral sensitivities, which means those materials have varying efficiencies at certain wavelengths to convert light into electricity. Therefore, awareness of the solar spectrum is required for researchers and engineers to choose or design photovoltaic materials that match the spectral distribution of sunlight. For instance, silicon-based solar cells exhibit heightened sensitivity to visible and near-infrared light, which makes up a significant part of the solar spectrum. Moreover, knowledge of solar spectrum requires optimizing PV cells efficiently and designing anti-reflection (AR) coatings.

1.2.1. Solar Spectrum

The solar spectrum represents the distribution of electromagnetic radiation released by the sun based on its wavelength. It ranges from shorter wavelengths (higher energy) gamma rays to longer wavelengths (lower energy) radio waves. However, the most significant portion of the solar spectrum for practical purposes, such as solar PV, is in the visible (380 to 700 nm) and near-infrared (larger and close to 700 nm) range.

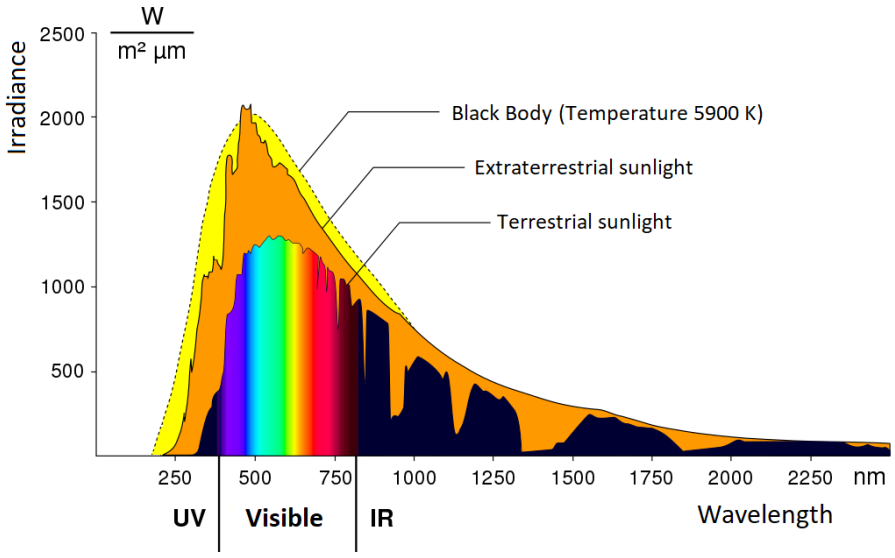

Fig. 1.3: The spectrum of solar radiation. Adapted from [10]

According to Fig. 1.3, three spectrums can be identified. Those can be listed as below.

- Black body (temperature 5900 K): The spectrum is similar to the ideal solar spectrum.
- Extraterrestrial sunlight: The spectrum at the upper end of the atmosphere of earth.
- Terrestrial sunlight: Sea level spectrum (Spectrum after it passed the earth's atmosphere).

Therefore, the terrestrial sunlight region is significant for the studies related to photovoltaic applications. Furthermore, according to the spectrum, terrestrial spectrum irradiance in the 400-900 nm wavelength range is highly intense. Therefore, optimization of photovoltaic applications within the range of the above wavelengths is crucial to get the best outcomes.

1.2.2. Air Mass (AM) index

The factors that can affect solar irradiance are latitude, time of the day and year, and weather conditions such as humidity and wind. To measure the performance of solar panels, an air-mass (AM) index is considered.

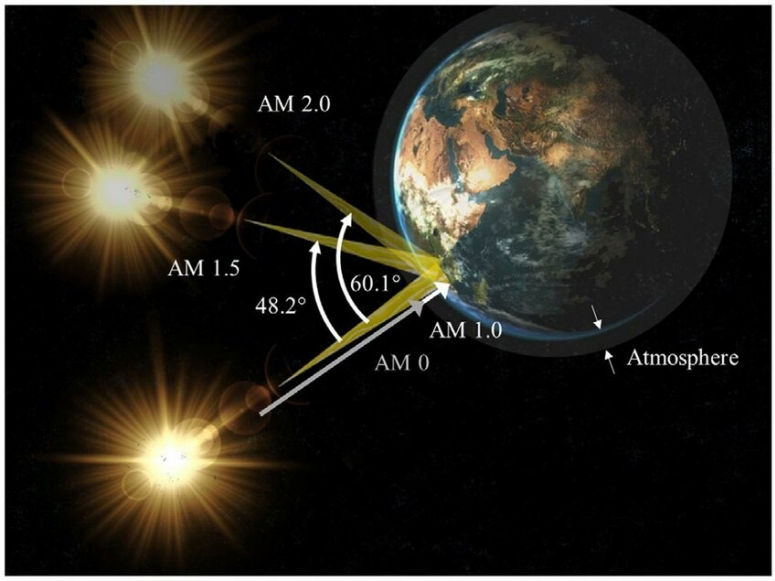

Fig. 1.4: Representation of the different solar spectrums. Adapted from [11]

This index has various values, such as AM 0, AM 1.0, AM 1.5, and AM 2.0, each representing the sunlight's behavior as it travels through the Earth's atmosphere at different angles (Fig. 1.4).

- **AM 0:** This refers to the solar spectrum in space before it encounters Earth's atmosphere. It is mostly used for satellites since it does not consider the atmosphere's effects.
- **AM 1.0:** This refers to sunlight that is directly overhead in equatorial or tropical regions. The sun's path is nearly straight through the atmosphere in these areas. This index is exact for solar devices in such regions but not fair enough for every location.
- **AM 1.5:** In most places on the Earth, the sunlight has to travel through a longer path (with an angle of 48.2^0) in the atmosphere due to the curvature of earth. Therefore, AM 1.5 spectrum representing the most relevant standard. Moreover, the intensity of AM 1.5 radiation is calculated by reducing 28% of AM 0 spectrum, where 18% is absorbed and 10% is scattered.

- **AM 2.0:** This refers to sunlight at a larger angle (60.1^0) through the atmosphere.

Therefore, the simulations of solar cells (SCAPS-1D, PC1D) and testing of the solar cells (solar simulator, UV visible) are conducted under the standard condition of AM 1.5.

1.3. Photovoltaic (PV) cells

In 1839, Alexandre Becquerel's discovery of the photoelectric effect laid the foundation for modern solar cell technology. This phenomenon involves specific materials releasing electrons upon exposure to light, effectively converting light energy into electrical energy. In 1883, Charles Fritt developed a photovoltaic cell by coating selenium with a thin layer of gold, yielding a 1% power conversion efficiency. In 1888, Aleksandr Stoletov developed a cell utilizing the outer photoelectric effect. Then, in 1954, Bell Laboratories introduced the first modern photovoltaic cell, achieving a power conversion efficiency of 4%.[12].

Solar cell technology steadily improved, making terrestrial use feasible by the 1970s. As the 21st century approached, solar cell technology gained momentum, driven by a growing awareness of environmental issues and the need for renewable energy sources. Considering the production principle, fabrication technology and type of materials, photovoltaic devices surpassed four generations. Fig. 1.5 shows the best-recorded laboratory-level power conversion efficiencies from the year 1975 to 2023.

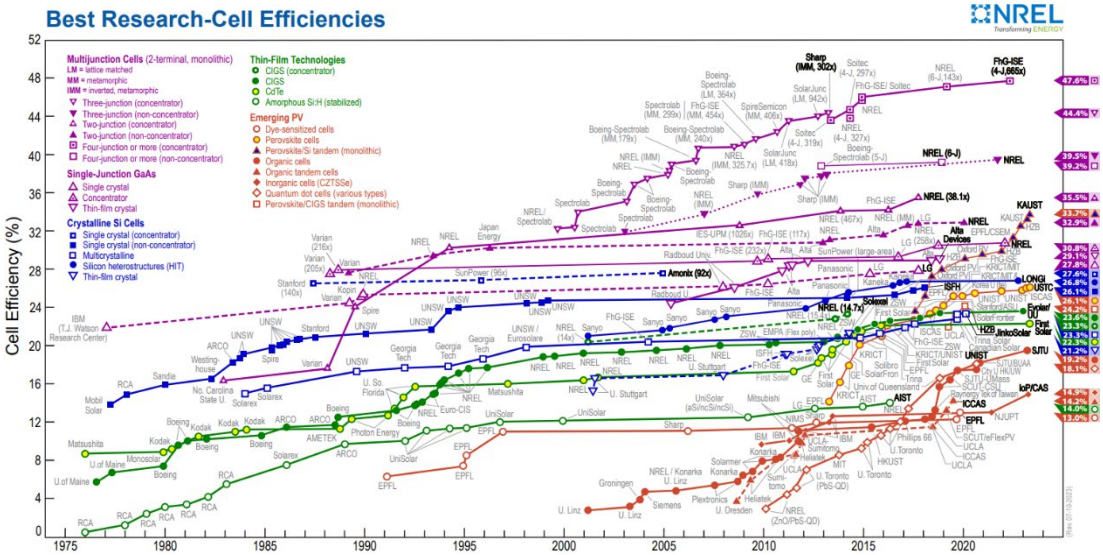

Fig. 1.5: The best recorded laboratory level power conversion efficiencies. Adapted from [13]

1.3.1 First generation

The earliest and most widely utilized type of photovoltaic devices for converting sunlight into electricity are referred to as first-generation solar cells or conventional solar cells. These solar cells are primarily made of silicon and can be further

categorized into two main types: Single-Crystal Silicon, which is made from a single-crystal structure of silicon and multi-crystal silicon, which is made from multiple small silicon crystals.

In 1953, the initial crystalline silicon solar cell was manufactured and the power conversion efficiency was recorded as 4.5%. By the subsequent year, this efficiency was improved to 6% [14]. In recent years, monocrystalline silicon solar cells and multi-crystalline silicon solar cells reached the power conversion efficiency of 27.8% and 26.1% at the laboratory level [13]. Nonetheless, the theoretical efficiency limit for first-generation photovoltaic (PV) cells is estimated at 29.4%, as established by the Shockley–Queisser (SQ) limit [15].

First-generation silicon solar cells are encountered for higher reliability and wide availability, but the manufacturing procedure of silicon-based solar cells can require significant energy inputs, leading to relatively high manufacturing costs. Therefore, ongoing research and development efforts are concentrating on enhancing the power conversion efficiency of solar cells while reducing costs.

1.3.2 Second generation

The second-generation solar cell, also referred to as a thin-film solar cell, is produced by depositing thin layers (one or more) of photovoltaic materials on the substrate. These solar cells have a much smaller thickness compared to conventional crystalline silicon solar cells. This characteristic enables thin-film cells to possess flexibility and lightweight, opening up numerous applications.

The first thin-film solar cell, Cu_2S/CdS, was fabricated using simple and cheaper technology known as the “Clevite process”, and power conversion efficiency was reported at a lower value of 10% [16]. Nevertheless, research on Cu_2S/CdS PV devices was very useful for later expansion of the thin-film industry. After that, another thin film technology called Amorphous Silicon (a-Si) was introduced. However, after several years, a-Si has failed to challenge the crystalline Si due to lower cost advantage, Lower power conversion efficiency and poor stability compared to crystalline Si. a-Si can only be used for niche applications due to its lower power conversion efficiency and instability. The reason behind low power conversion efficiency was identified as dangling bonds of the material. Afterwards, Hydrogenated Amorphous Silicon (a-Si:H) was invented and it increased the power conversion efficiency in small amounts by reducing dangling bonds, but it was insufficient to generate power on a large scale. Hence, a-Si and a-Si:H failed to compete with crystalline Si.

Later, Cadmium Telluride (CdTe) and Copper Indium Gallium Selenide (CIGS) thin film solar cells were invented and they offered unique benefits and have found their niches in the solar energy market. While CIGS is known for its potential for high power conversion efficiency and flexibility, CdTe is recognized for its cost-effectiveness and suitability for large-scale installations [17]. Among the three solar cell technologies,

a-Si has a negligible market share, while CIGS and CdTe have the largest global market share [18].

At the laboratory level, a-Si, CdTe and CIGS solar cells achieved the highest efficiencies of 14%, 22.3%, and 23.6%, measured at 25 ^{0}C under the AM1.5 spectrum [13]. However, the power conversion efficiency compared to the first-generation and second-generation solar modules, the first generation of crystalline silicon still leads. Therefore, power conversion efficiency enhancement of second-generation solar cells is a critical area of research to make solar energy more cost-effective and competitive.

1.3.3 Third generation

Third-generation solar cells refer to a new class of photovoltaic devices that aim to overcome the limitations of traditional solar cells by employing novel materials and designs to enhance efficiency and reduce costs. These cells are capable of achieving high power conversion efficiency while simultaneously maintaining lower manufacturing costs. Among the third-generation solar cells are Perovskite Solar Cells (PSC), Dye-sensitized Solar Cells (DSSCs), Quantum Dot Solar Cells (QDSSCs), and Tandem Solar Cells (TSC) [19].

In 2009, the first PSC solar cell was invented with a power conversion efficiency of 3.8%. After continuous efforts, the latest power conversion efficiencies for DSSC, PSC, QDSSC and TSC were recorded as 13%, 26.1%, 18.1%, and 14.2% [13].

While some third-generation technologies show high efficiency at the laboratory scale, ensuring these materials' long-term stability and durability is a significant challenge, especially for outdoor applications. Moreover, scaling up production to commercial levels while maintaining quality and cost-effectiveness remains another challenge. Despite these challenges, ongoing research and development efforts are actively addressing these issues, and now it become a rising interest in third-generation solar cells due to their potential to advance the efficiency and versatility of solar energy technology.

1.3.4 Fourth generation

After third generation, fourth-generation solar cells, alternatively identified as hybrid inorganic cells, were introduced and it is still in the research and development stage. The fourth generation of solar cells offers impressive affordability and flexibility through the utilization of thin polymer layers, metal nanoparticles, and a range of metal oxides, as well as carbon nanotubes, graphene, and their related materials. Recently, the laboratory-level power conversion efficiency of 20.3% was accomplished for the perovskite solar cells based on graphene.

These technologies aim to surpass the constraints of previous generations and enhance efficiency even further, cost-effectiveness, and versatility of solar energy conversion.

1.4. Theoretical Background of photovoltaic solar cells

1.4.1 Theory of p-n junction and photogeneration

The process of photogeneration of a solar cell relies on the operation of the p-n junction, a crucial element in the conversion of sunlight into electricity. This junction is established by combining p-type and n-type semiconductor materials. Within the p-type semiconductor material, a surplus of positively charged holes occurs due to doping with acceptor atoms. In contrast, in the n-type material, there is an excess of negatively charged electrons resulting from doping with donor atoms. Upon the establishment of contact between the p-type and n-type semiconductors, excess electrons in n-side diffuse to p-side, while excess holes in p-side diffuse to n-side. Concurrently, electrons which are diffused from n-side, recombine with free holes at the p-side, whereas diffusing holes recombine with free electrons at the n-side. Consequently, the majority of carriers near the p-n junction on each side are depleted, due to diffusion and recombination. This region is identified as a depletion region (Fig. 1.6).

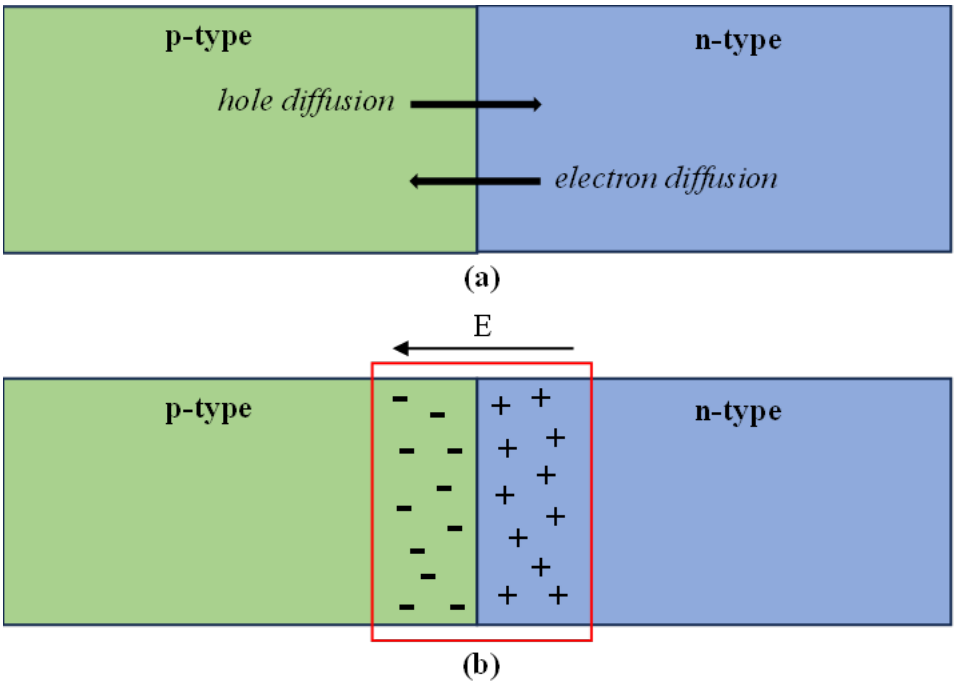

Fig. 1.6: (a) p-n junction before the diffusion **(b)** After equilibrium state

As a result of majority carrier diffusion, a positive charge accumulates on the n-side while a negative charge accumulates on the p-side of the p-n junction. This configuration generates an electric field at the p-n junction, which counteracts additional diffusion of holes and electrons.

When photons from sunlight interact with solar cell surface,

- Some of them reflect back from the surface.
- The photons bearing lower energy transmit through the semiconductor.

- The photons bearing higher energy than the bandgap of the semiconductor absorbs by itself.

Upon absorption of a photon with adequate energy, the semiconductor has the capacity to generate an electron-hole pair. Initially, this electron resides in the valence band of the semiconductor, and owing to the energy of the photon, that undergoes an "excitation" process, transitioning it to the conduction band. Because of the aforementioned built-in electric field, the photogenerated electrons are forced towards the n-side of the junction, while the holes are forced towards the p-side, as illustrated in Fig. 1.7. This separation of charges creates a flow of electrons and holes in opposite directions, which results in an electric current.

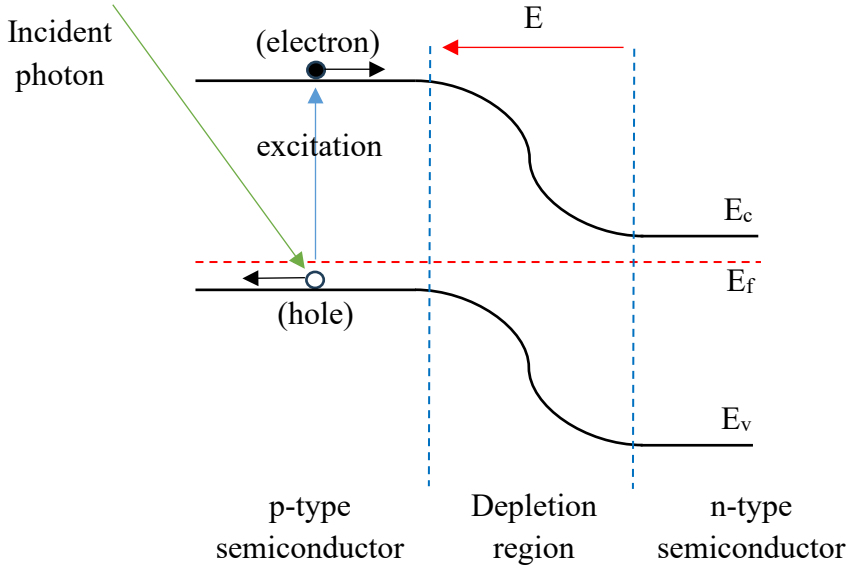

Fig. 1.7: Energy band diagram of the solar cell

1.4.2 Surface recombination in a solar cell

Surface recombination in solar cell is loss of charge carriers near the surface of the semiconductor material. Surface recombination can be identified as one of the foremost factors in diminishing the power conversion efficiency of a solar cell. That is caused by decreasing the number of charge carriers that cause to the generating electrical current [20].

In solar cells, Semiconductor material has a periodic structure, but the atoms at the surface have not fulfilled its bonding requirement. That causes dangling bonds at the surface of the semiconductor (Fig. 1.8 (a)). Dangling bonds can act as defects, also known as trapping states for electrons and holes. When charge carriers encounter these defects, they may become trapped, leading to surface recombination (Fig. 1.8 (b)).

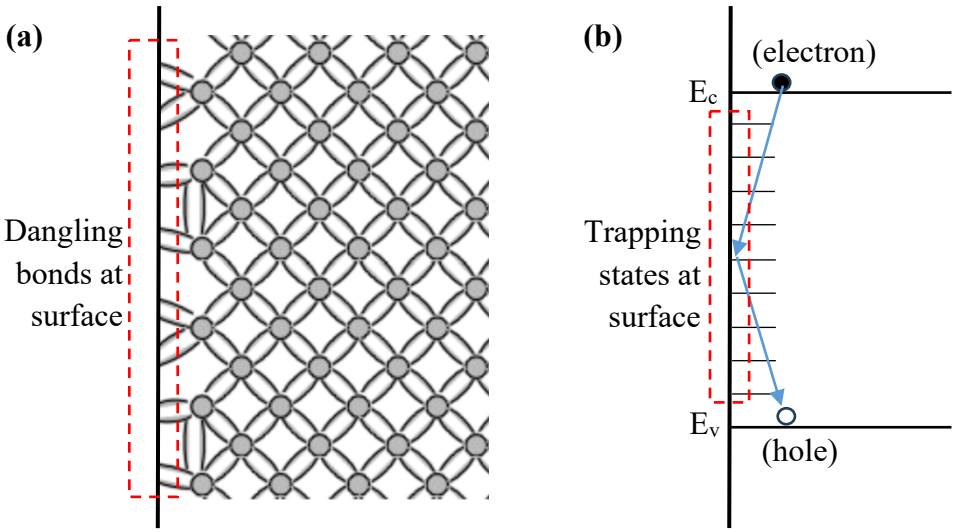

Fig. 1.8: (a) Dangling bonds at the surface of the semiconductor **(b)** Recombination of electrons and holes at the surface

strategies can be employed, such as the surface passivation and Back Surface Field (BSF) layer. Atteq ur Rehman *et al.* [21] reviewed the significance of surface passivation to improve PV cell efficiency. It entails applying a coating or treatment to the semiconductor surface to mitigate the density of surface defects and trap states. That will minimize the possibility of charge carriers being captured and recombined near the surface. Moreover, B. Barman *et al.* [22] explained the potential of mitigating surface recombination at the rear surface of a thin-film solar cell through utilization of BSF layer. The BSF layer is a high-doping region near the back surface and helps prevent charge carriers from reaching the rear surface and recombining.

Therefore, minimizing recombination losses and maximizing the power conversion efficiency of the solar cell would be significant for making them more effective for renewable energy applications.

1.4.3 Fill Factor (FF) and power conversion efficiency

In order to characterize the performance of a solar cell, fill factor (FF) plays a significant role and it can be defined as the ratio of the maximum power output to the product of open-circuit voltage (V_{OC}) and short-circuit current density (J_{SC}) of solar cell, as shown in Eq. 1.1. V_{OC} corresponds to the voltage when there is no current flowing through the device, while J_{SC} represents the current density when there is no voltage drop across the solar cell.

$$FF = \frac{P_{MP}}{V_{OC} \times J_{SC}} \times 100\% \qquad \textbf{Eq. 1.1}$$

$$P_{MP} = V_{MP} \times J_{MP} \qquad \textbf{Eq. 1.2}$$

Graphically, the FF of solar cell can be expressed as "squareness". In detail, it corresponds to the largest rectangle that can fit within the current density-voltage (JV) curve (Fig. 1.9).

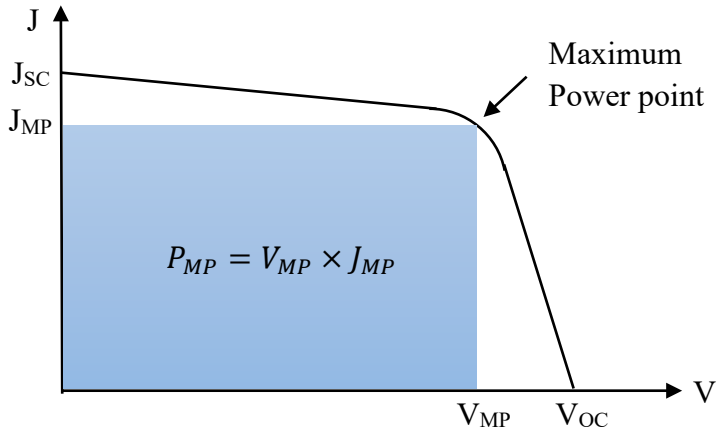

Fig. 1.9: J-V characteristic of a solar cell

1.4.4 Quantum efficiency (QE) and power conversion efficiency (PCE)

Quantum efficiency can be described as fraction of incident photons converted into electron-hole pairs, which can be stated as a function of a wavelength of incident photons. For instance, if all photons at specific wavelengths are absorbed by the semiconductor, QE at that wavelength is said to be unity. Moreover, QE is zero for the incident photons that are lower in energy than the bandgap of a semiconductor due to a lack of photogeneration. Further, the External Quantum Efficiency (EQE) and the Internal Quantum Efficiency (IQE) can be considered as the two types of QE parameters.

Therein, EQE denotes the efficacy of a solar cell in converting incident photons into electrical current across various wavelengths. EQE considers the entire external system, including the solar cell's interfaces, contacts, and losses, before the current is extracted. The IQE refers to the efficiency of converting absorbed photons into electrical current at different wavelengths. The equations for EQE and IQE are indicated in Eq. 1.3 (depending on the wavelength of photons).

$$EQE = \frac{electrons/s}{incident\ photons/s} \quad \& \quad IQE = \frac{electrons/s}{absorbed\ photons/s} \qquad \textbf{Eq. 1.3}$$

In measuring the solar cell's performance, power conversion efficiency stands out as one of the most significant factors. PCE quantifies how effectively a solar cell transforms incident sunlight into electrical power under standardized conditions. It can be described as a ratio between electrical power output of the solar cell and the total power input from sunlight. Moreover, PCE includes all losses within the cell, and it provides a single overall solar cell's efficiency irrespective of the wavelength of light. The mathematical representation of the PCE is shown in Eq. 1.4.

$$PCE = \frac{V_{OC} \times J_{SC} \times FF}{P_{in}} \times 100\% \qquad \textbf{Eq. 1.4}$$

Furthermore, PCE depends on the spectrum of solar irradiance, incident irradiance of sunlight, and temperature. The standard conditions for solar cell designing and laboratory-level fabrications are AM1.5, 300 K, 100 mW/cm^2.

1.5. Introduction of Anti-reflection (AR) coating on solar cell

Anti-reflection (AR) coatings are an essential component of modern photovoltaic technology that plays a crucial role in maximizing the power conversion efficiency of solar panels. The primary limitation on the power conversion efficiency of thin-film solar cells stems from its reflection of incident light from their front surface. AR coatings, which are ultrathin and transparent film coating applied on the solar cell's front surface (Fig. 1.10), can ensure high power conversion efficiency by reducing the reflectance. Introducing an AR coating is one of the most preferred technologies to improve the power conversion efficiency of thin film photovoltaic devices. The inclusion of an anti-reflective (AR) coating can induce destructive interference within the cell by altering the characteristics of the surface coating.

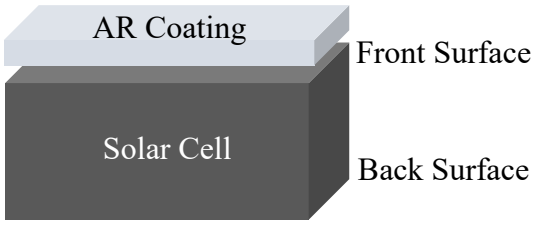

Fig. 1.10: Structure of a solar cell with AR coating

These coatings are developed using different materials, such as SiO_2, TiO_2, ZnS, ZnO, and MgF_2. Moreover, AR coatings are typically applied through chemical vapor deposition (CVD) and physical vapor deposition (PVD) techniques. Among PVD techniques, radio frequency magnetron sputtering is the most common physical method to fabricate AR coatings, and among CVD techniques, plasma-enhanced chemical vapor deposition (PECVD) method has become dominant. Furthermore, some wet chemical methods such as chemical bath deposition (CBD), spin coating, and screen-printing deposition methods can also be used for AR coating deposition.

While AR coatings offer significant advantages, they may not be equally effective for all wavelengths of light. Therefore, it should be optimized for specific parts of the solar spectrum. Therefore, the thickness and material properties should be precisely controlled during manufacturing to achieve the desired optical properties.

1.5.1 Theory of AR coating design

The primary objective of depositing AR coating on the surface of a substrate that minimizes the reflection of light over a specific wavelength range. Initially, designing single-layer AR coating using theoretical calculations would be favorable prior to the fabrication. The design of AR coatings is based on the interference principle.

Therefore, it considers the relative phase shift between the incident beam reflected at the upper and lower surface of the AR coating.

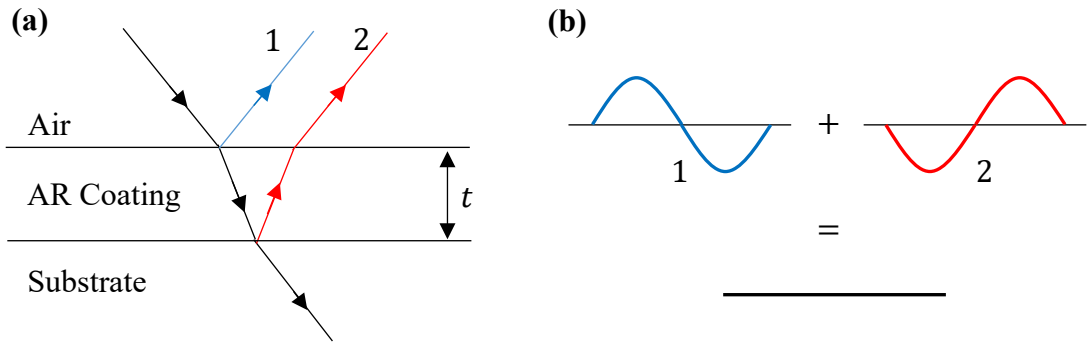

Fig. 1.11: (a) Reflection of light at top and bottom surfaces of the AR coating **(b)** Destructive interference between reflected beams

When incident light hits the AR coating, as shown in Fig. 1.11 (a), it partially reflects at the top of the AR coating (ray 1). The remains travel through the AR coating and again partially reflect at the bottom surface, and that portion will emerge from the top surface (ray 2). Herein, incident light enters the AR coating through the air medium, with the refractive index of air typically being lower than that of the AR coating. Therefore, rays 1 and 2 should have a 180º phase shift, equal to $\lambda_{AR}/2$ phase shift (where λ_{AR} is the light wavelength in the AR coating), as shown in Fig. 1.11 (b).

The thickness of the AR coating is a crucial factor for the specific wavelength in which destructive interference occurs. According to Fig. 1.11 (a), ray 2 travels approximately 2t (t is the thickness of the AR coating) distance than ray 1. Therefore, to obtain destructive interference between ray 1 and ray 2 could be mentioned as below.

$$2t = \frac{\lambda_{AR}}{2}$$

Moreover, the relationship between the incident wavelength (λ) and wavelength inside the AR coating (λ_{AR}) can be calculated as follow.

$$\lambda_{AR} = \frac{\lambda}{n_{AR}}$$

Where n_{AR} is refractive index of the AR coating. According to aforementioned formulas, AR coating thickness can be measured from the below equation.

$$t = \frac{\lambda}{4n_{AR}}$$

Therefore, the AR coating's optical thickness (multiplication of the physical thickness by refractive index of coating material) must be equal to the quarter of the incident light wavelength for obtaining zero reflectance, as indicated in Eq. 1.5.

$$n_{AR}t = \frac{\lambda}{4} \qquad \textbf{Eq. 1.5}$$

Furthermore, the reflectance of a single layer AR coating deposited on a substrate can be calculated according to the theory of reflection [23]. Eq. 1.6 depicts the mathematical equation for total reflectance of the incident light.

$$R = \frac{r_1^2 + r_2^2 + 2r_1r_2cos\theta}{1 + r_1^2 + r_2^2 + 2r_1r_2cos\theta} \qquad \textbf{Eq. 1.6}$$

Where, r_1, r_2 are the amplitudes of reflected beams from the AR coating top and bottom surface, respectively. θ is incident angle of the light. Then,

$$r_1 = \frac{n_0 - n_{AR}}{n_0 + n_{AR}}$$

$$r_2 = \frac{n_{AR} - n_S}{n_{AR} + n_S}$$

$$\theta = \frac{4\pi}{\lambda} n_{AR}t$$

Where, n_0 and n_S (≈ 1.5) are refractive indexes of air and substrate, respectively. Moreover, in a solar simulator, the incident light angle is typically set to be perpendicular to the surface for standard performance testing. Therefore, simulations should be done accordingly.

1.5.2 Literature review on AR coatings

The first AR coating was invented by British Physicist John William Strutt, who was the Nobel Prize winner in physics in 1904 [23]. However, the test was carried out on the glass substrate. After the early development of AR coatings, it became widespread use in the 21st century, especially in the field of photovoltaic. In recent years, both simulation and experimental research have been carried out based on AR coatings.

1.5.2.1 Simulation studies based on AR coatings

Simulating anti-reflective (AR) coatings is a critical step in the development and optimization of several photovoltaic applications. Devendra Kc *et al*. [24] conducted a review on the influence of various AR coatings on CdS/CdTe Solar Cells through simulation studies. The characteristics of the solar cells can be simulated using personal computer one-dimensional (PC1D) simulation software. Herein, different anti-reflection materials such as Aluminum Trioxide (Al_2O_3), Magnesium Fluoride (MgF_2), Magnesium Oxide (MgO), and Tin Oxide (SnO_2) were applied as an AR coating, and their reflectance properties were characterized. The thicknesses of the AR coatings were calculated using Eq. 1.5, and those values were applied to the PC1D software.

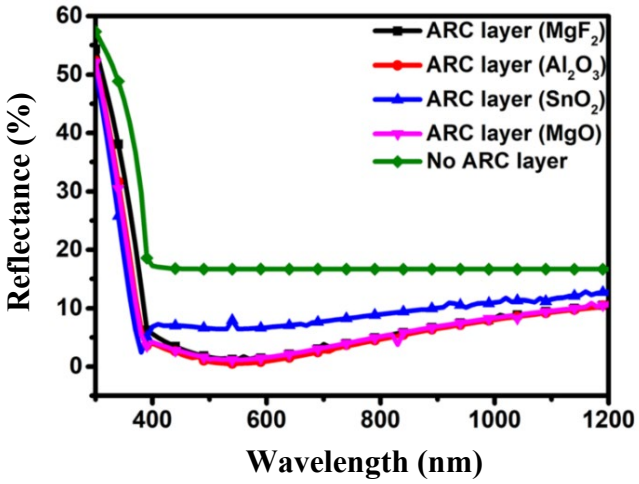

Fig. 1.12: Reflectance spectrum obtained from PC1D simulation. Adapted from [24]

Fig. 1.12 illustrates the reflectance spectrum obtained from the simulation. According to the reflectance analysis, it was identified that AR coatings can significantly reduce the reflectance, but reflectance is based on the material properties of AR coatings. Therefore, it was observed that materials such as SnO_2 were not ideal for AR coating of CdS/CdTe solar cells, while Al_2O_3 indicated the lowest average reflectance in 300 nm to 1200 nm wavelength range.

Moreover, R. Sharma *et al.* [25] analyzed the comparison between numerical calculations and simulation results on reflectance Silicon Solar cells. In the aforementioned study, authors have examined the effect of the set of AR coatings (MgF_2, SiO_2, Si_3N_4, Al_2O_3, TiO_2 and ZnS) using the mathematical equation for reflectance (Eq. 1.6), while a simulation study was carried out on PC1D simulation software. As the design of the AR coating is based on a particular wavelength range, the authors observed the relative spectral response of silicon cells as well as the distribution of the solar spectrum, while considering the peak energy of these spectrums. Fig. 1.13 shows the reflectance spectrum obtained from theoretical equation and PC1D simulation.

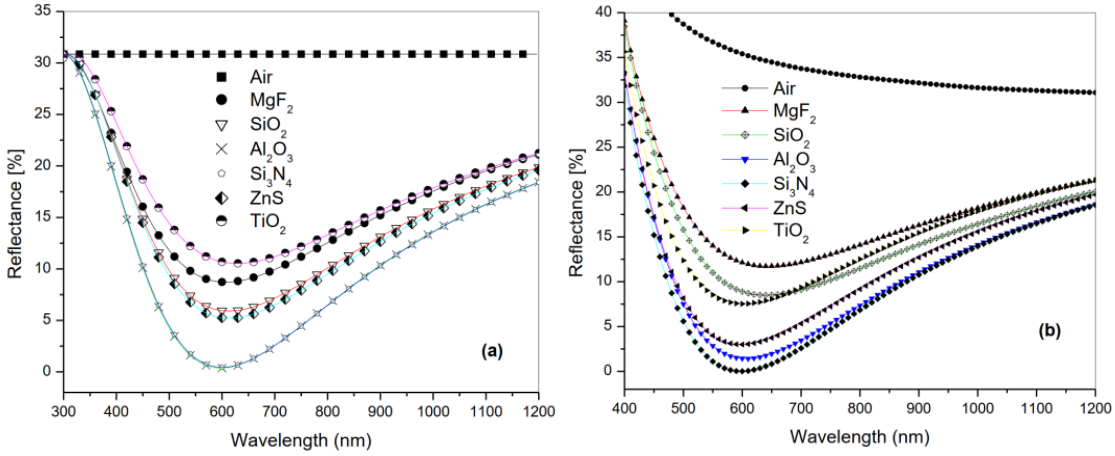

Fig. 1.13: Reflectance Spectrums **(a)** using theoretical equation and **(b)** using PC1D simulation. Adapted from [25]

However, there can be deviations between simulation results and experimental details. The accuracy of PC1D simulations heavily depends on the accuracy of the material properties and parameters entered by the user. If the material data is inaccurate or incomplete, it can lead to incorrect simulation results. Therefore, entering the possible actual parameters to the simulation measured from the experiment would be better for higher accuracy. Additionally, one of the recently developed simulation software, the Solar Cell Capacitance Simulator in one-dimension (SCAPS-1D), is utilized for analyzing and optimizing the CdTe-based solar cells in this investigation. Moreover, SCAPS-1D developed at the University of Gent in Belgium, providing free of charge to the PV research community.

1.5.2.2 Laboratory experiments on AR coatings

Experiments based on different AR materials, such as ZnS, TiO_2, SiO_2, ZnO, and SiN_x, have been the dominant field of photovoltaic research. These studies have included various analyses such as reflectance measurements, structural analysis, thickness optimization, concentration analysis, electrical measurements, durability testing, etc. Therefore, in this exploration, identifying the previous effort would be favorable before the experiment.

U. Gangopadhyay *et al.* [26] fabricated the low-cost ZnS AR coating for mono-crystalline silicon solar cells using the chemical bath deposition (CBD) technique. Authors have used zinc sulfate and thiourea as Zn^{2+} and S^{2-} precursors, respectively. This experiment identified that refractive index and thickness depend on the mounting angle of wafers in a CBD bath. Moreover, thickness could be proportionally varied w.r.t deposition time. As the outcome, I_{SC} and PCE improved by 6.5% and 5% respectively. However, there can be some practical issues in the CBD process for AR coating fabrication. When fabricating the AR coating on the Si wafer in the CBD bath, the whole substrate was covered by ZnS during deposition. Therefore, it should be concerned about the safety of solar cells. Another experiment based on ZnS AR coating was done by Ammar T. Salih *et al.* [27] using the thermal evaporation technique. For the thermal evaporation technique, the source material is required as a solid (ZnS powder). Therein, thickness, surface roughness, and average grain size were discussed. In this experiment, the authors proposed the deposition of ZnS layers in individual evaporation sessions to reduce the surface roughness and average grain size. That resulted in a reduction in the reflectivity of the front surface.

Minghua Li *et al*. [28] fabricated the SiO_2 AR coating using an electron-beam evaporation technique for silicon solar cells. In this experiment, the authors employed the commercially available substrate, which already included SiN_x AR coating deposited by plasma-enhanced chemical vapor deposited (PECVD). Therein, the addition of another AR coating (SiO_2) was investigated. According to the electrical characterization, the J_{sc} was improved from 36.74 to 37.77 mA/cm^2, and PCE was enhanced slightly from 17.48% to 17.8%. In a nutshell, the enhancement of J_{sc} and PCE was relatively lower than expected by adding a second AR coating. It may occur due to using commercially available substrates instead of laboratory-developed

substrates. However, the electron-beam evaporation technique is more favorable for AR coating depositions due to precise control, uniform deposition, wide material compatibility and low-temperature process. However, it can be expensive to purchase and maintain. Moreover, SiO_2 can be used as AR coating in photovoltaic applications. Wei Zhang *et al.* [29] deposited a thin SiO_2 coating on a soda lime glass substrate using a simplest technique of spin coating technique. Therein, tetraethoxysilane (TEOS) was used as the SiO_2 precursor, and ethanol was used as the solvent. Moreover, hydrochloric acid was employed for catalysis. In this experiment, the optical transmittance of soda lime glass substrate was improved by 5% in the 300 to 1300 nm wavelength range. Therefore, the authors provided good evidence for employing SiO_2 as AR coating.

Apart from the materials mentioned above, Jui-yu Wang *et al.* [30] experimented using TiO_2 as an AR coating. This study used the liquid phase deposition (LPD) technique to deposit a TiO_2 thin layer. Therein, $(NH_4)_2TiF_6$ was used as a Ti precursor, and H_3BO_3 was employed to control the deposition rate of the TiO_2. This experiment was done for silicon substrate, and the average minimum reflectance and transmittance were recorded as 2.7% and 96.5%, respectively. These values depicted good evidence for TiO_2 to be employed as AR coatings. Additionally, in LPD technique substrate is immersed in the chemical solution as CBD. However, LPD is known for its excellent control over film thickness than CBD.

Radiofrequency (RF) sputtering technique is another common technique that can be employed for fabricating AR coating. However, this technique requires a solid form of material because the process involves sputtering atoms or molecules from a solid target material. For instance, using the RF-sputtering technique, Raghavendra Sagar and Asha Rao [31] fabricated ZnO, MgO and Al_2O_3 AR coatings for silicon solar cells. Therein, the thicknesses of the AR coatings were calculated using Eq. 5, and it was controlled by varying base pressure and sputtering power. In this experiment, the uncoated solar cell's PCE of 8.29%, 8.33% and 8.38% enhanced to 9.63%, 9.86% and 9.13%, using ZnO, MgO and Al_2O_3 AR coatings, respectively. Since RF sputtering is a valuable technique for producing high-quality thin films with precise control over properties like thickness, it may not be a cheap technique due to equipment, target material, operational, and maintenance costs.

Moreover, ZnO thin film can be deposited using both chemical deposition and physical deposition techniques. Radio frequency magnetron sputtering is the most common physical technique to fabricate ZnO thin film [32]. Among chemical deposition techniques, chemical bath deposition (CBD) [33], spin coating [34], doctor blade [35], and screen-printing [36] deposition techniques could be used to deposit on both conductive and non-conductive substrates. Herein, the spin coating technique can be identified as cheapest and easiest way to fabricate an ultrathin ZnO layer, which can further be employed as an AR coating for second generation thin film solar cells.

1.5.2.3 Fabrication of ZnO thin film coating using spin coating technique

Among AR coating materials such as SiO_2, TiO_2, ZnS, ZnO, and MgF_2, ZnO is a nontoxic, low-cost, wide band gap (Eg~3.37 eV) [37] semiconductor material at ambient temperature in the crystalline form. Moreover, in the photovoltaics industry, ZnO is used as a transparent conductive oxide (TCO) layer, electron transparent layer (ETL), and AR Coatings due to its natural n-type electrical conductivity, excellent optical transmittance in visible light, and optimum refractive index (n~2.0) [37], respectively. In addition, due to its excellent optical transparency, low resistance, and ability to grow using low-temperature deposition techniques, it finds widespread application in optoelectronic devices such as photovoltaic solar cells, laser diodes, field emission, absorption devices, light emitting diodes (LED), and acoustic–optical devices [38]. Moreover, the spin coating technique can achieve consistent and reproducible film thickness by precisely controlling parameters such as spin rate, spin time, and solution concentration. Furthermore, this technique is more applicable where low deposition temperature is required.

Nilam B. Patil *et al.* [39] fabricated a ZnO thin film on a glass substrate. Therein, the authors used zinc acetate dihydrate ($Zn(CH_3COO)_2.2H_2O$) as Zn precursor and absolute ethanol with m-cresol as solvent. The solution was maintained at 0.2 M concentration. During spin coating, drop volume, spin rate and spin time were maintained at 0.5 ml, 2000 rpm and 40 s, respectively. After the deposition, samples were transferred to annealing process at 400 ^{0}C for 2 hours. These samples were subjected to X-ray diffraction (XRD) and X-ray photoelectron spectroscopy (XPS) to identify the grown layer and surface composition. Accordingly, the authors made a good agreement with the standard values of ZnO. Moreover, from optical analysis, it was found that the bandgap value was 3.21 eV, which was closer to the theoretical bandgap of ZnO (3.37 eV). In [40], the authors explored the material properties concerning different solution concentrations. Therein, zinc acetate dihydrate ($Zn(CH_3COO)_2.2H_2O$) was used as Zn precursor and isopropanol (IPA) was used as solvent. During the experiment, the concentration changed from 0.3 M to 0.7 M, and all samples were post-annealed at 450 ^{0}C for 1 hour. Subsequently, samples were subjected to an atomic force microscope (AFM) scan to analyze surface roughness. It was identified that surface roughness was improved with the concentration of solution due to a higher crystal growth rate at the liquid-solid interface at a higher solution concentration.

The post-annealing temperature of the experiments may be a crucial factor in optical performance. Mursal *et al*. [41] fabricated a set of ZnO samples by varying post-annealing temperature from 300 to 700 ^{0}C at 100 ^{0}C steps. The authors used zinc acetate powder as Zn precursor dissolved in ethanol, and stearic acid. Here, stearic acid was used as stabilizer. The samples were subjected to UV visible spectrometer analysis to measure transmittance and absorbance. It was observed that the transmittance decreases slightly, while absorption increases with an increase in post-annealing temperature. However, after 350 nm wavelength, absorption is closer to zero. Moreover, the authors discovered that the band gap of ZnO decreased slightly

while increasing post-annealing temperature, because higher temperatures can lead to increased grain size and improved crystallinity. This reduces grain boundary defects, which can influence the electronic properties and band structure, resulting in a slight decrease in the band gap. Therefore, it would be better to maintain an appropriate post-annealing temperature.

The ZnO thin film thickness with spin rate was reported by M. Smirnov et al. [42]. Therein, the spin rate ranged from 700 to 1600 rpm and deposition duration was maintained at 10 s. The authors observed that film thickness was almost proportional to the spin rate, and the value varied from 1300 to 300 nm. The concentration of the solution was 0.55 M. Moreover, the authors suggested a coating drying cycle method for increasing film thickness. Here, the same procedure was repeated several times on one substrate and the substrate was heated to 100 ^{0}C between two adjacent depositions. The outcome was that film thickness could be proportionally improved with the deposition cycles.

Theopolina Amakali et al. [43] reported a comparison of ZnO fabrication using spin coating technique and molecular precursor method (MPM). Based on the crystallite size, dislocation density, and surface roughness, the research findings indicate that the ZnO thin films produced through the spin coating method exhibited superior quality and crystallinity compared to those fabricated using the MPM approach. Furthermore, the bandgap obtained through the MPM method was 3.75 eV, exceeding the theoretical ZnO bandgap of 3.37 eV, whereas the bandgap achieved via the spin coating technique was 3.25 eV, approaching the theoretical value. Hence, in the fabrication of ZnO thin layers, the authors provided compelling evidence for the suitability of spin coating.

Generally, solar cells are manufactured for long-term usage. Therefore, the durability of spin-coated ZnO coatings should be a concern. Gerald Womack *et al.* [44] did standard tests on ZnO AR coating fabricated on a glass substrate and observed a 69-74% reduction in reflection losses. The coatings were then subjected to cross-hatch test and pull test methods to measure the adhesion. The AR coating remained adhered to the substrate even after the pull test, with the highest recorded pulling strength that did not result in coating delamination being 4.92 MPa. The Cross-hatch test was done by creating scratched parallel lines in a cross-hatch pattern. Therein, zero damage was reported. According to the high-temperature test, the properties of the samples did not change in atmospheric conditions. However, the authors observed the damages in ZnO coatings after 100 ^{0}C. Moreover, the authors suggested not using ZnO AR coatings for CdTe superstrate configuration if the exposed temperature exceeds 500 ^{0}C. Further, the samples depicted good resistance to the humidity (measured at RH ~ 85%). Moreover, the stability in the acid environment was analyzed. The samples were immersed in dilute sulfuric acid (pH ~ 3.5), and it was noted that ZnO coatings exhibited susceptibility to degradation in acidic environments. In addition, the coatings can be damaged by abrasion if aggressive cleaning techniques are utilized.

In summary, spin rate, spin time, and solution concentration should be considered to fabricate the ZnO layer at desired thickness using the spin coating technique.

According to this literature review, the thickness of the AR coating was calculated from theoretical formula, and fabrication was done based on the calculated thickness. However, variation of reflectance with the thickness should be analyzed separately, because there can be some deviation in the fabrication setup.

1.6 Introduction of back surface field layer (BSF) on solar cell

The BSF layer is a crucial component in enhancing the efficiency of solar cells by addressing key performance challenges. Fig. 1.14 illustrates the structure of a solar cell with BSF layer. Positioned at the rear of the solar cell, the BSF layer creates a potential barrier that reflects minority carriers such as electrons in p-type materials back into the active region of the cell. Accordingly, this layer plays a significant role in enhancing performance by improving charge extraction, promoting exciton dissociation, and acting as a hole-transporting layer.

.

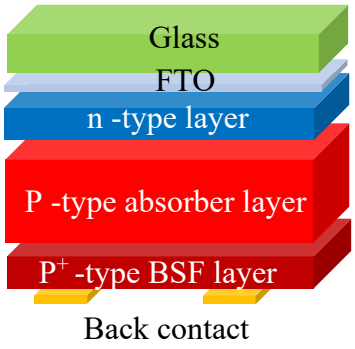

Fig. 1.14: Structure of a solar cell with BSF layer

1.6.1 Theory of BSF design

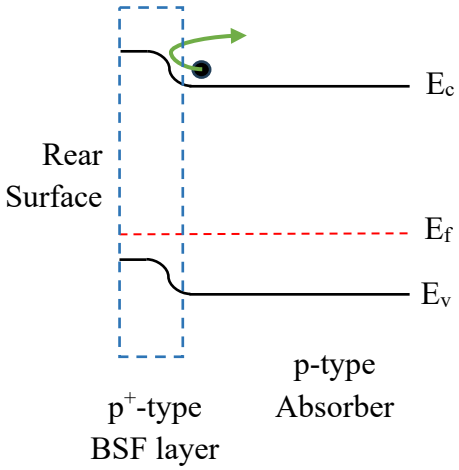

Fig. 1.15: Arrangement of the band diagram of solar cell with BSF layer

higher hole concentration (P+ region) adjacent to the absorber layer, which is also P-type. The transition from P+ to P creates a junction with a gradient in hole concentration, forming a P+ - P high-low junction. The P+ - P high-low junction

establishes a localized electric field within the BSF layer. This electric field is directed towards the solar cell's rear surface, creating a potential barrier. Here's how it acts as a charge extraction layer, promotes exciton dissociation, and functions as a hole-transporting solid electrolyte:

- **As Charge Extraction Layer**

Due to the potential barrier at the back surface of the cell, which reflects minority carriers (electrons in p-type material and holes in n-type material) back into the active region. In detail, according to Fig. 1.15, the barrier for electrons makes it more challenging to recombine at the rear surface. This reflection increases the likelihood of these carriers being collected at the respective electrodes, leading to improved charge extraction and overall cell efficiency.

- **Promoting Exciton Dissociation**

In photovoltaic devices, excitons (bound electron-hole pairs) need to be dissociated into free charge carriers to contribute to the electric current. The BSF layer can enhance the internal electric field within the device, which helps in the separation of excitons into free electrons and holes. Moreover, by passivating defects at the back surface, the BSF layer reduces recombination sites, allowing more excitons to dissociate effectively.

- **As Hole-Transporting Solid Electrolyte**

The BSF layer material is chosen for its good hole transport properties, ensuring efficient movement of holes towards the back contact. Normally, hole mobility of the BSF layer is often higher the hole mobility of absorber layer.

1.6.2 Review on BSF layer

Studies on BSF layers have mostly occurred in recent years in simulation studies. These simulations can provide a valuable impact on the different design choices, such as optimize material properties, and predict the solar cell's performance with BSF layers under different conditions. Currently, there are several freely accessible and commercially available software for modeling and simulating solar cells. PC1D, AMPS, SCAPS, NSSP and MSCS software are available free of cost, while GPVDM and SETFOS software are available as paid one-dimension simulation tools for thin film solar cells [45]. Among them, Solar Cell Capacitance Simulator in One Dimension software (SCAPS-1D) and Personal Computer one Dimensional software (PC1D) are a widely used software for modeling thin film solar cells.

Devendra KC *et al.* [46] reviewed the graphene as a BSF Layer material for CdS/CdTe solar cell using PC1D simulation. This study investigated the BSF layer properties, such as doping concentration and thickness. It was observed that, with a higher doping concentration of the BSF layer, the efficiency of the cell remained at higher values. However, a further increase in doping concentration did not affect the efficiency enhancement. Therefore, there should be an optimum value for BSF layer doping

concentration. Regarding BSF layer thickness, the J_{SC} value and the *PCE* increased slightly when the BSF layer thickness increased. Moreover, the V_{OC} and *FF* value did not show any notable variation. Finally, the author has proven that graphene as the ultrathin BSF layer could be used for producing highly efficient CdTe/CdS solar cells.

Virang Shukla *et al.* [47] investigated the impact of Cu_2Te BSF layer on the CdS/CdTe solar cells using SCAPS-1D simulation. After adding the of 0.1 μm thick BSF layer, the possibility of thickness reduction of the absorber layer (CdTe) was 4 μm to 1 μm, while keeping the good power conversion efficiency. This reduction of thickness would reduce the cost of manufacturing solar cells. Moreover, the effect of the BSF layer resulted in an enhancement of the *PCE* from 14.87 to 19.06%. Furthermore, in [48], the authors conducted a SCAPS-1D simulation to analyze the effect of PbTe BSF layer on CdS/CdTe solar cell performance. The thicknesses of the layers were 30 nm CdS, 1 μm CdTe, and 0.1 μm PbTe. In this study, PCE was enhanced from 15.05 to 19.28% with the effect of the BSF layer. Therefore, it was clear that the addition of the BSF layer is efficient and exhibits a more excellent cost-effective structure than the reference structure.

In addition, the effect of other solar cells' electrical parameters (J_{SC}, V_{OC} and FF) with the absorber layer thickness is observed in several studies. For instance, Sayed Rezwanul *et al.* [49] simulated the impact of the $BaSi_2$ as BSF layer on second-generation CIGS solar cells. Therein, the BSF layer thickness was kept at 0.3 μm and variation of electrical parameters with the thickness of the absorber (CIGS) layer was investigated. The authors observed that when the thickness of absorber layer increased from 0 to 0.8 μm, J_{SC}, *FF,* and *PCE* sharply increased, whereas V_{OC} showed only slight variation was sharply increased, whereas V_{OC} showed only slight variation. However, after the point of 0.8 μm, not only V_{OC} but also J_{SC}, *FF,* and *PCE* were slightly increased, which was negligible. Therefore, 0.8 μm thickness was identified as the optimum thickness for the absorber layer. In this study, the reference structure obtained 25.1% with the 3 μm absorber layer thickness, while the proposed structure with the BSF layer obtained 26.24% only with 0.8 μm absorber layer thickness. Further, the same kind of research was carried out by B. Barman *et al.* [22]. Therein, the PbS layer was considered the BSF layer. In this experiment, J_{SC}, V_{OC}, *FF,* and *PCE* variations made better promise with previously reviewed literature. The results obtained were PCE of 24.22% with a 1.5 μm CIGS absorber layer and 0.15 μm PbS BSF layer. Therefore, according to the literature, the authors agreed to a cost-effective structure by lowering the manufacturing cost of the absorber layer.

Since SCAPS-1D is the most popular software for designing thin-film solar cell structures, there can be found some other simulation tools that are employed in BSF layer designs. Nowshad Amin *et al.* [50] investigated the improvement of CdS/CdTe cell efficiency with the ZnTe BSF layer using the Numerical Solar Cell Simulation (NSSP) Program. Therein, the authors considered the reference structure as the experimental results available in [51]. In reference, the reordered efficiencies were 15.3% with a 7 μm CdTe layer and 11.5% with a 1.2 μm CdTe layer thickness. Initially, the reference structure was modeled via simulation and obtained that there

was no such variation of the electrical parameters in the region of 3 to10 μm CdTe layer thickness. Moreover, the lower generation rate at the back surface (CdTe/metal interface) was found to be the reason for this behavior of the solar cell. Then, a 0.2 μm ZnTe BSF layer was introduced to reduce recombination at the back surface. Accordingly, a 1 μm thin CdTe cell has demonstrated an enhancement in efficiency, reaching approximately 20%. In this study, the authors made a good approach to making a numerical study, starting with experimental-related details and obtaining an optimum result via a simulation platform. Furthermore, Sabrina Benabbas *et al.* [52] reported a simulation study based on SnS as a BSF layer. Therein, Analysis of Microelectronic and Photonic Structures in 1 Dimension (AMPS-1D) was employed for analysis of the structure. The introduction of a SnS layer in the proposed cell has yielded an efficiency of 21.83%, employing only 1 μm for the CdTe layer and 0.4 μm for SnS. Herein, the reference achieves an efficiency of 17.40% with a 1 μm-thick CdTe absorber layer, comparatively. In addition, it was observed that the variation of electrical parameters (J_{SC}, V_{OC}, *FF,* and *PCE*) obtained from NSSP and AMPS-1D were almost similar to the results obtained from SCAPS-1D-based works of literature.

Furthermore, BSF layer fabrication for a solar cell is a crucial step to enhance the performance of solar cells. Nonetheless, literature that extensively discusses the fabrication of BSF layers is rare to find. However, only some experimental studies are based on BSF layers for the first-generation Silicon solar cells. Xueliang Yang *et al.* [53] fabricated the ZnS thin film as a BSF layer for Silicon solar cell. This particular study was carried out in two phases; in the first stage, the solar cell structure was simulated with the ZnS BSF layer [54], and in the next stage, fabrication was executed. The BSF layer was fabricated using radio frequency magnetron sputtering, and the Si solar cell was fabricated using the PECVD technique. According to the results, the authors identified that V_{OC} and *FF* were clearly enhanced, whereas J_{SC} did not show any notable variation. Moreover, the reference structure baring 6.40% efficiency enhanced to 8.97% after introducing the BSF layer. In [55], the authors deposited Al as a BSF layer using the sputtering technique. Therein, *PCE* was enhanced from 12.96 to 13.75%. However, there was not any clear variation in *FF*, but V_{OC} and I_{SC} were clearly enhanced.

Therefore, these experiments are evident in using the BSF layer to enhance the performance of thin film solar cells. Since the thin-film industry is a wide research area, numerical investigations on efficiency enhancement methods such as BSF layers would be useful in the future.

1.7 Characterization technique

Characterization of a material involves analyzing and evaluating its properties to better understand its composition and behavior. This sub-section briefly describes the characterization techniques classified in Fig. 1.16 that will be used in this study.

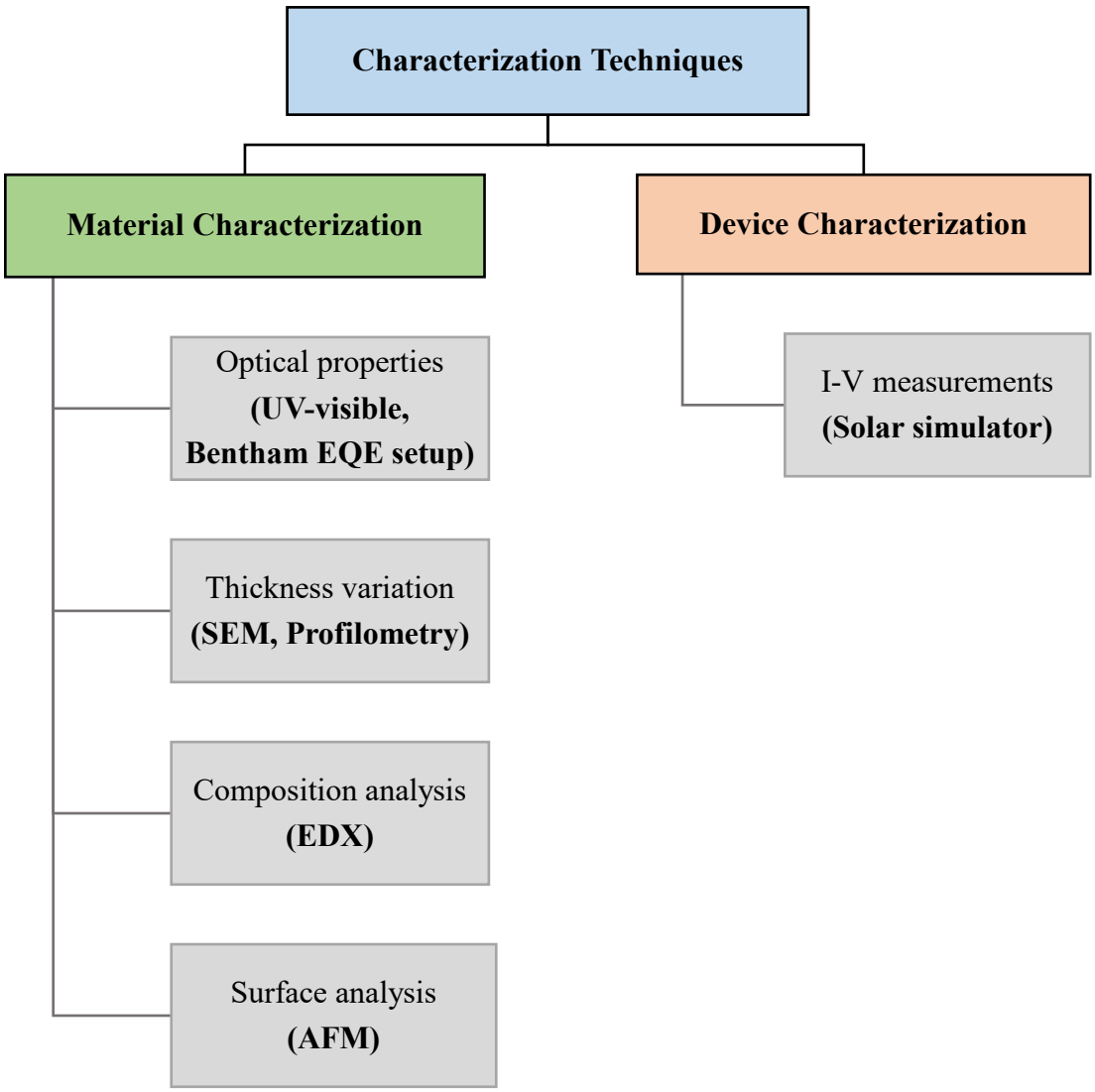

Fig. 1.16: Material and device characterization techniques

1.7.1 Optical properties (UV-visible spectroscopy, Bentham EQE setup)

1.7.1.1 UV-visible spectroscopy

In this research, a UV-visible spectrophotometer will be used to measure the absorbance and transmittance of an AR coating. The sample can be exposed to various wavelengths encompassing the near-ultraviolet (200-400 nm), the visible (400-700 nm), and the near-infrared (700-1000 nm).

Fig. 1.17 illustrates a schematic diagram of the UV-visible spectrophotometer employed. The instrument is controlled via a computer, and its light source comprises tungsten-halogen lamps, emitting visible and near-infrared light within the range of approximately 320 to 1100 nm, and deuterium lamps, which emit ultraviolet light in the 190-370 nm range [56]. The optical pathway begins with the entrance slit, which narrows the broad-spectrum white light from the light source. The narrowed beam then encounters a collimator lens and transforms it into a parallel incident light beam. Subsequently, the prism creates monochromatic light or the component wavelengths.

The exit slit is positioned to focus this monochromatic light onto the sample as required for the investigation. Finally, a photodetector identifies the fraction of light absorbed by the sample, which is achieved by detecting the intensity of the transmitted light beam.

In solid-state physics and material science, a graphical method called "Tauc plot" is

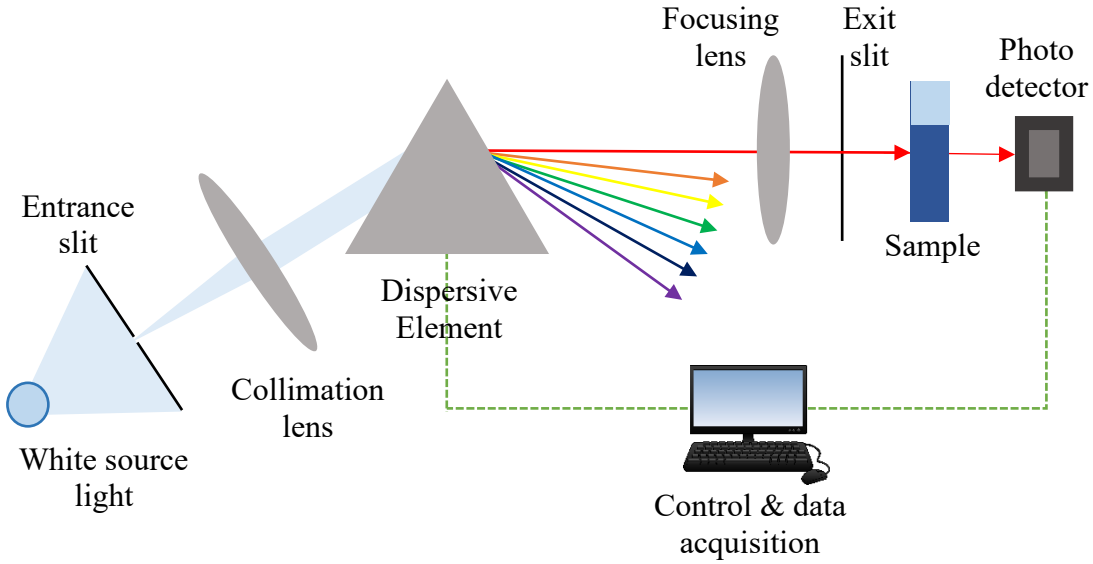

Fig. 1.17: Schematic diagram of an UV-visible spectrophotometer

used to determine the optical bandgap of a material. Tauc's equation depends on the correlation between band gap energy (E_g), absorption coefficient (α), incident photon, Planck's constant (h) and frequency (ν) as indicated in Eq. 1.7 [56]. Here, k represents the proportionality constant, depends upon the refractive index of the sample.

$$\alpha = \frac{k(h\nu - E_g)^m}{h\nu} \qquad \textbf{Eq. 1.7}$$

The value m can be defined as 1/2 for direct bandgap and for the indirect band gap materials it can be considered as 2. Then, Tauc equation for direct bandgap material can be written as Eq. 1.8.

$$(\alpha h\nu)^2 \propto h\nu - E_g \qquad \textbf{Eq. 1.8}$$

Therefore, Tauc's plot of $(\alpha h\nu)^2$ against hν can be drawn. Herein, the photon energy(hν) can be calculated as follows.

$E = h\nu$; where h and ν are Planck constant and frequency of light, respectively.

$c = \nu\lambda$; where c is speed of light.

Then,

$$E = \frac{hc}{\lambda}$$

$h = 6.626 \times 10^{-34} Js,\ \ c = 3 \times 10^{8} ms^{-1},\ \ 1ev = 1.6 \times 10^{-19} J$

Therefore,

$$E = \frac{6.626 \times 10^{-34} \times 3 \times 10^{8}}{1.6 \times 10^{-19} \times \lambda} \times 10^{9}$$

$$E = hv = \frac{1240}{\lambda} \qquad ;\lambda \ in \ nm \qquad \textbf{Eq. 1.9}$$

The absorbance spectrum measured from UV-visible provides the spectrum of absorbance of material (α) with respect to the wavelength (λ). Therefore, the corresponding axes values of the Tauc plot can be calculated using Eq. 1.9. Moreover, the x-intercept of the linear portion corresponds to the bandgap energy (E_g) of the material (Fig. 1.18).

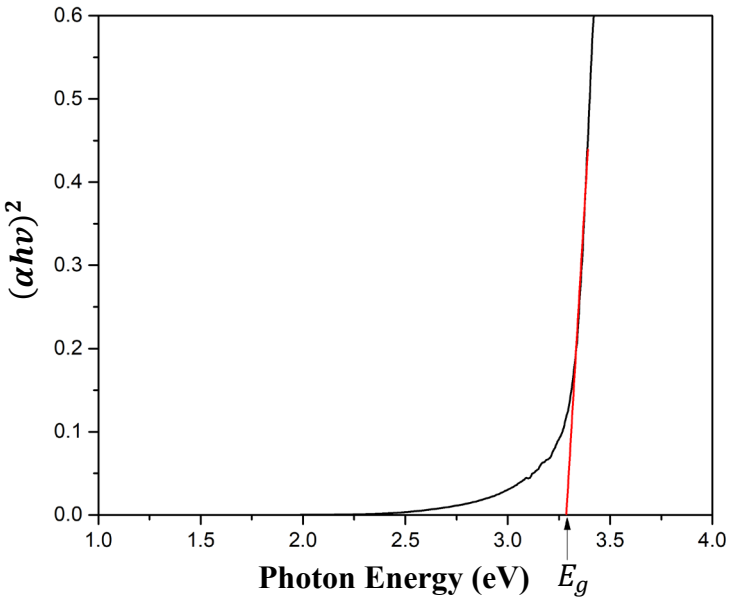

Fig. 1.18: Tauc plot

1.7.1.2 Bentham EQE setup

The DTR6 integrating sphere, a component of Benthem EQE setup (PVE300) [57, 58]. This equipment ensures accurate measurement of the diffuse transmittance and reflectance of a wide range of materials. In this study, it will be used to measure the reflectance of AR coating. The configuration diagram of DTR6 is shown in Fig. 1.19. The DTR6 integrating sphere is an optical instrument designed to capture and measure the total integrated reflection from a sample across the 300 to 2000 nm wavelength range. It is beneficial for samples with various surface textures or materials. In Fig 1.19, specular reflection refers to the smooth reflection of light from a surface, while diffuse reflection occurs when light strikes an irregular surface and scatters in various directions. The detector measures the total integrated reflectance.

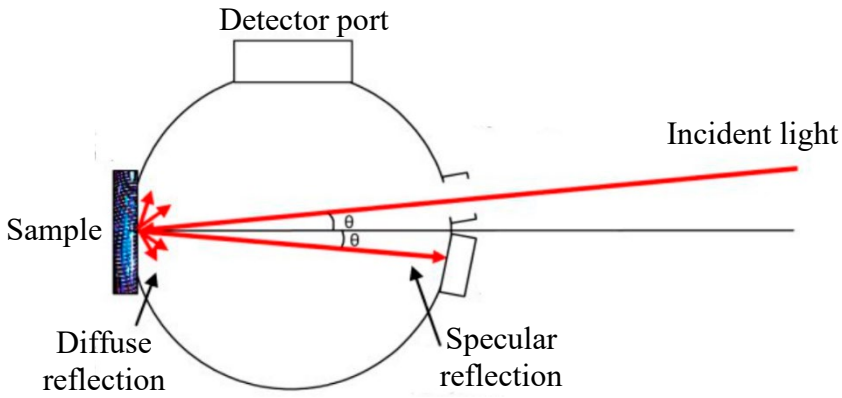

Fig. 1.19: Configuration of the DTR6 integrating sphere. Adapted from [58]

1.7.2 Thickness variation (Profilometry)

1.7.2.1 Scanning Electron Microscope (SEM)

Scanning electron microscopy (SEM) is utilized to measure the semiconductive thin films thickness and that can be applicable to both single- and multi-layer materials. This method is well-suited for both conductive and semiconductive materials with thickness ranging from 20 nm to 100 μm. However, for non-conductive materials, effective analysis is attainable by preparing the sample with a conductive thin layer material deposited on its surface.

The electron source of the SEM projects a focused electron beam through the anode and other lenses over the surface of a sample (Fig. 1.20). The electrons in the beam engage with the atoms in the sample, giving a variety of signals. Among these signals, secondary electrons play a crucial role in the creation of SEM images. Additionally, backscattered electrons arising from the interaction can be utilized alongside secondary electrons in the production of detailed SEM images. Using this high-resolution image, the thicknesses of each layer of multi-layer cross section can be measured. However, this technique doesn't provide average layer thickness, and it can be obtained by taking the measurement at more places of same sample.

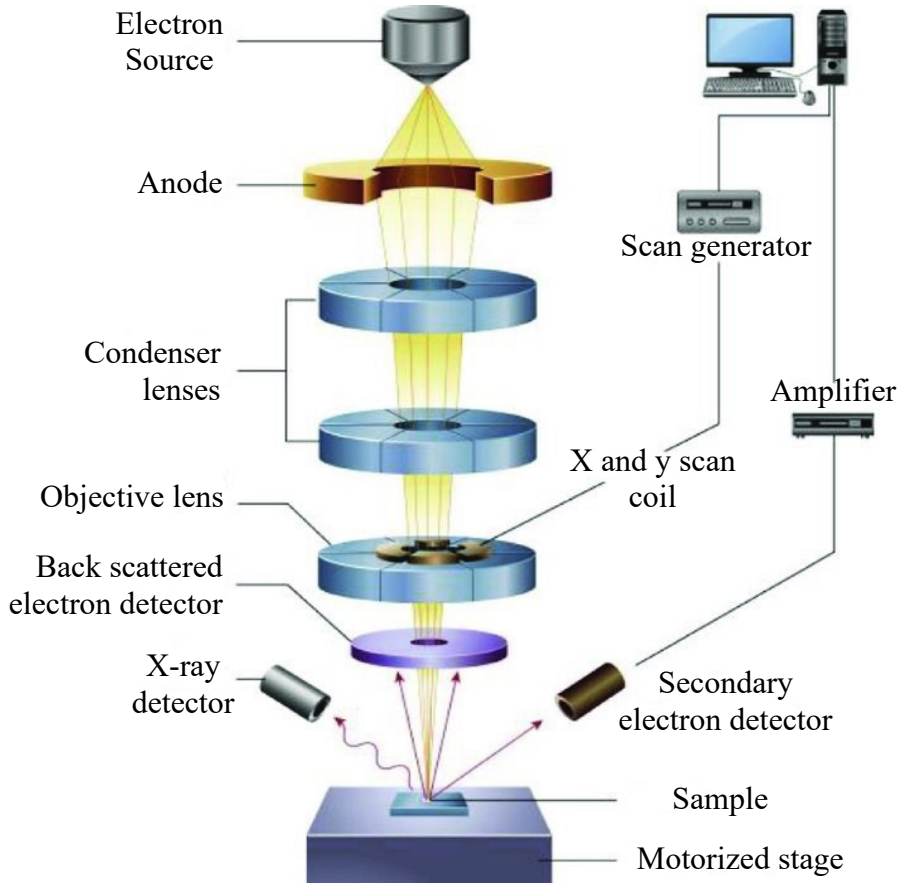

Fig. 1.20: Schematic diagram of SEM. Adapted from [59]

1.7.2.2 Profilometry

Profilometry is widely used for measuring the thickness of thin films. It requires only a step from an uncoated region to a coated region, enabling the determination of step height and, consequently, the thickness of the layer. In the spin coating deposition technique, stepping can be obtained by applying thermal tape on the substrate before the fabrication, and after, it can be removed. Since profilometry measures the average thickness of the selected area (Fig. 1.21), this method ensures higher accuracy in the measurement.

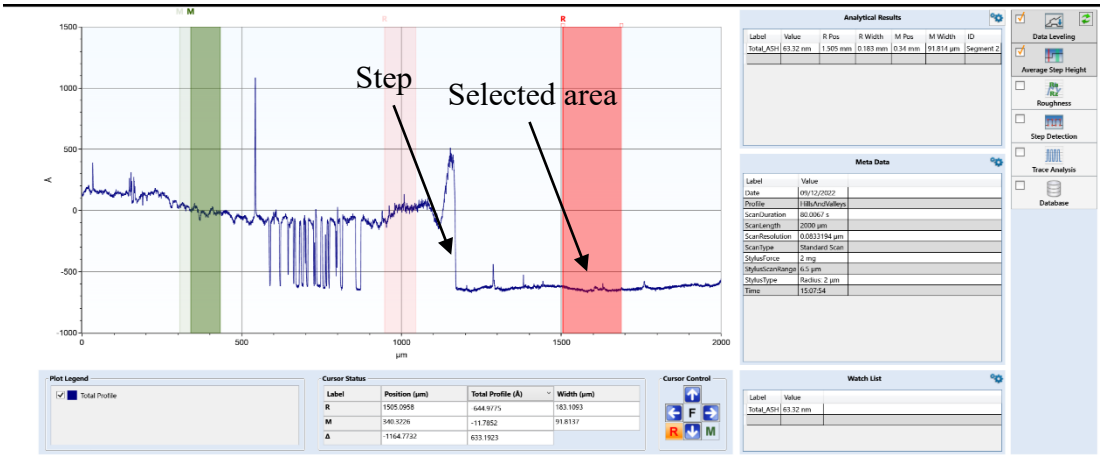

Fig. 1.21: Average thickness measurement from profilometry.

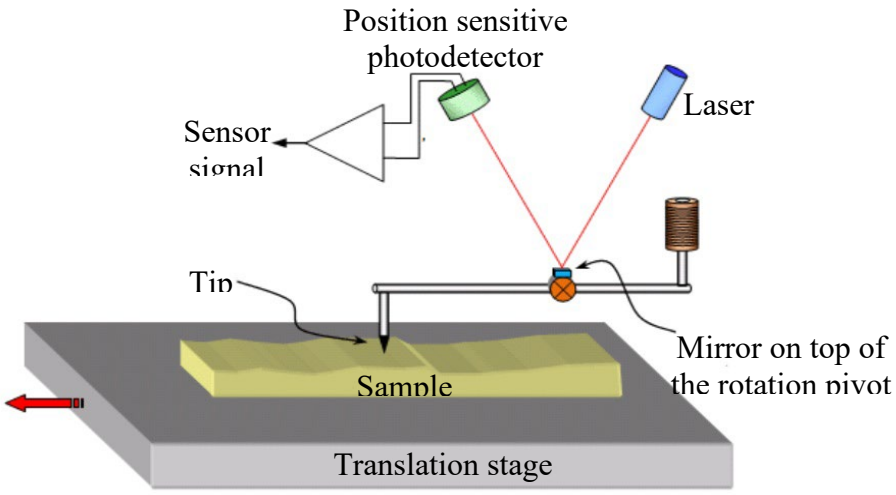

Fig. 1.22: The structure of profilometry. Adapted from [60]

Fig. 1.22 illustrates the structure of profilometry [60]. Therein, a tip makes direct contact with the sample surface. When the tip moves vertically, the sample and its stage are simultaneously shifted horizontally, enabling the vertical measurement spanning from less than 1 nm to 1 mm.

1.7.3 Composition analysis (EDX)

Energy dispersive X-ray analysis (EDX) is a compositional elemental identification technique. In EDX, an electron source is used to generate an electron beam. The electron beam accelerates to high energy and then reduces the beam's diameter. Subsequently, the beam focused on the specific position of the sample. Once electron beam coming from the microscope interacts with the sample, it can cause the sample's electrons to become excited or ionized. The high-energy electrons from the electron beam collide with the sample atoms' inner shell (K, L, M) electrons. These collisions result in the ejection of inner shell electrons. When an inner shell electron is ejected, it leaves behind a "core hole" in the atom's electron structure. An outer shell electron may transit to the inner shell to fill the core hole and achieve a stable electronic configuration. As this outer shell electron drops to a lower energy state, it releases energy as an Auger electron. In addition to Auger electrons, the transition of an outer shell electron to fill the core hole can also lead to the emission of X-rays. These are known as "characteristic X-rays." Fig. 1.23 illustrates the electron transition between energy states and the emission of the X-rays ($L_\alpha, K_\alpha, K_\beta$) [61].

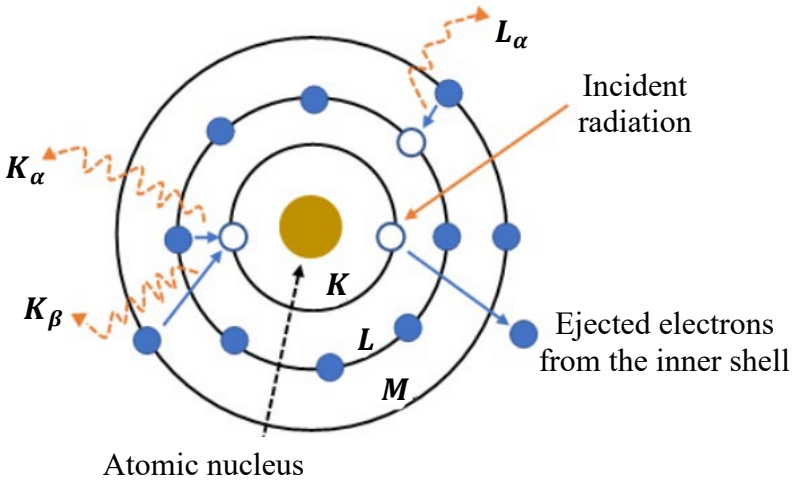

Fig. 1.23: Phenomena of emitting electrons. Adapted from [61]

The energy of X-rays emitted is specific to the involved element and corresponds to the energy difference between its electron shells. An EDX detector detects the emitted characteristic X-rays, measuring their energy. The system subsequently analyzes the energies of the detected X-rays. Each element generates characteristic X-rays at distinct energies, enabling the identification of elements within the sample.

1.7.4 Surface analysis (AFM)

Atomic force microscopic (AFM) analysis is considered as a core technique to be identified the topography of a conductive or a nonconductive sample surface by the deflection of a cantilever. Herein, a laser beam focused on the backside of the cantilever is used to detect the deflection of the cantilever. As the cantilever bends, its deflection is measured with high precision. In this regard, the deflection of the cantilever is indicated by the movement of the laser spot on the detector. The collected height and deflection data are used to reconstruct a high-resolution, three-dimensional topographical image of the sample.

Basically, AFM can operate in three various modes, tapping mode (intermittent contact), contact mode (constant force), and non-contact mode. Fig 1.24 illustrates the different modes of operation of AFM.

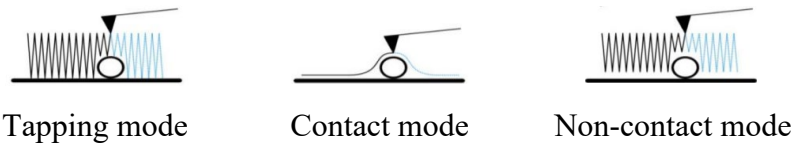

Fig. 1.24: The operation modes of AFM

In contact mode, the tip of the cantilever is subjected to remain as constant contact with the sample surface, in contrast in non-contact mode, the tip is positioned at a distance of 50-150 Å above the surface of the sample. However, the tip of the cantilever makes contact with the sample surface intermittently in tapping mode. The contact mode and tapping modes have fast scan rates and higher image resolution than

non-contact mode. Also, the soft samples can be damaged in contact mode than the tapping mode.

1.7.5 I-V measurements (Solar simulator)

After the fabrication of solar cells (without and with AR coating), devices will be measured using a solar simulator under the illumination of 1.5 AM. Prior to the measurement, a "1.5M standard cell" is used as a reference photovoltaic cell to calibrate the device for AM1.5 conditions.

Measuring the current-voltage characteristics involves varying the voltage across the solar cell while simultaneously measuring the resulting current. This test provides data, including the short-circuit current density (J_{SC}), short-circuit current (I_{SC}), open-circuit voltage (V_{OC}), fill factor (FF), power conversion efficiency (PCE), maximum power output (P_{MP}), current at maximum power point (I_{MP}), Voltage at maximum power point (V_{MP}), series resistance (R_s), and shunt resistance (R_{sh}). The obtained results can be used to compare solar cell performance under various modifications.

1.8 Aim of the present study

1.8.1 Overview

Nowadays, most countries search for additional energy approaches to access the increasing demand through renewable sources, especially solar energy. Photovoltaic cells are the pivotal technology that directly transforms solar energy into electricity, enabling a sustainable and clean energy source. Crystalline silicon is the most common and widely available semiconductor material commercially applied to manufacture solar cells. However, the growth of crystalline silicon wafers is highly expensive and therefore, the manufacturing cost of a solar cell is comparatively high. Recently, thin-film solar cell technologies such as cadmium telluride and copper indium gallium selenide cells are emerging as low-cost alternatives. However, efficiency still lags behind the conventional silicon solar cells.

According to literature, the key factors of the lower efficiency of thin-film devices are the reflection of the incident light occures at the front surface of the solar cell and surface recombination occurs at the rear surface of the absorber layer. Therefore, this study aims to fabricate AR coating using a low-cost deposition technique to minimize the reflection at the front surface and conduct a simulation study for the BSF layer to minimize surface recombination for the laboratory developed CdS/CdTe thin film solar cells.

Accordingly, the present work, Zinc Oxide (ZnO) is to be selected as AR coating, and the cheapest manufacturing method of the spin coating technique is to be selected for the growth of ZnO material. Moreover, Tin Sulfide (SnS) will be introduced as a BSF layer, and a simulation study will be conducted from SCAPS-1D simulation software. Finally, the performance of the proposed structures will be analyzed.

1.8.2 Objectives

In this research, the primary objective is to design an efficiency enhanced structure for selected thin-film solar cell technology. Hence, the specific objectives are:

1. To identify the most suitable efficiency enhancement technologies for thin film solar cells based on comprehensive literature review as well as simulation studies.
2. To fabricate the best possible Anti-Reflection (AR) coating on a selected thin film solar wafer.
3. To investigate possible other technologies to further enhance efficiency using simulation studies.

CHAPTER 2

FABRICATION OF SPIN-COATED ZnO AR COATING FOR CdS/CdTe SOLAR CELLS

2.1 Introduction

As per the literature, the variants of thin film solar cell technologies are a-Si, CIGS and CdTe. Moreover, aforementioned cells can be arranged as substrate or superstrate configurations [62]. In a substrate configuration, the incident light traverses the substrate after reaching the semiconductor layer, while in a superstrate configuration, the incident light hits the superstrate before reaching the semiconductor layer. Among them, the widely used configuration for thin-film solar cells are superstrate configuration due to the possibility of increased light absorption of the device, protection, and durability.

Currently, many experiments are going on about thin-film photovoltaic technologies to improve efficiency, cost-effectiveness, and sustainability. In Sri Lanka, the University of Kelaniya and the University of Peradeniya contributed together for developing an inexpensive strategy for fabricating the laboratory scale CdS/CdTe solar cells (superstrate configuration). Therein, the CdS thin films were grown using the chemical bath deposition (CBD) technique at the University of Kelaniya, and CdTe films were grown by the close-spaced sublimation (CSS) technique on top of the CdS layer at University of Peradeniya [63–65]. In this study, aforementioned laboratory-developed glass/FTO/CBD-CdS/CSS-CdTe/Cu/Au solar cell is used for the experiments of ZnO AR coating and experiments were conducted at the University of Kelaniya laboratory. The structure of solar cell and the visual image of the solar cell are shown in Fig. 2.1 (a) and (b), respectively.

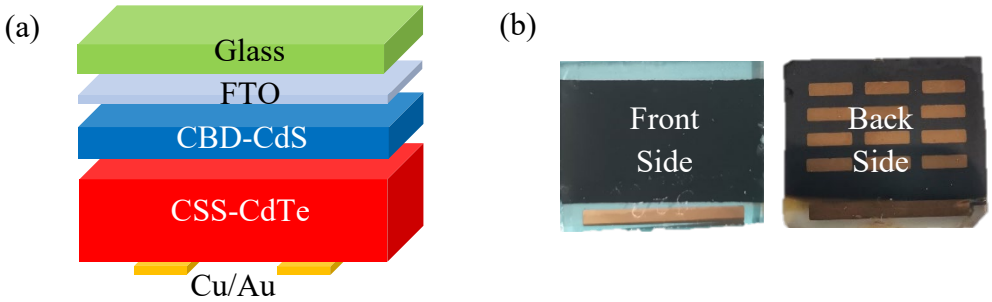

Fig. 2.1: (a) The structure of the solar cell and **(b)** the visual image of the solar cell

This study intends to lessen reflection at the front surface of solar cells fabricated in a superstrate configuration. Therefore, the AR coating is to be deposited on the glass substrate and that would be a non-conductive surface. Herein, the expected structure of the solar cell with the AR coating is illustrated below as per the Fig. 2.2.

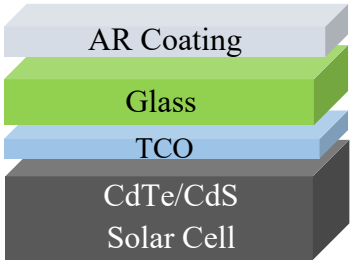

Fig. 2.2: CdS/CdTe solar cell structure with AR coating

In this regard, there are two methodologies for AR coating deposition on the glass substrate: before fabricating the solar cells or else on top of the device fabricated. However, the growth of the AR coating on the top of the side of the glass substrate prior to the device fabrication can damage AR coating throughout the solar cell material deposition process as it includes several deposition and annealing steps. Note that in the process of CdS deposition, CBD is a solution-based process where the substrate is immersed in a chemical bath, leading to deposition on both sides of the substrate. If a ZnO layer is deposited first, it will be covered by the CdS during the CBD process. The CdS will then form a layer over the ZnO, complicating the intended use of ZnO as an AR coating. Hence, it is advantageous to follow the latter.

2.2 Design of single layer ZnO AR coating

Designing single-layer AR coating using theoretical calculations would be favorable prior to the fabrication. AR coatings are designed considering the relative phase shift between the incident beam reflected at the upper and lower surface of the AR coating. Therefore, the AR coating's optical thickness must be equal to a quarter of the incident light wavelength for obtaining zero reflectance, as mentioned in Eq. 1.5, Chapter 1.

The wavelength range considered in this experiment was 300-900 nm. However, a single-layer AR coating meets the minimum reflectivity only in a single wavelength, not over the whole wavelength range. Consequently, the initial design focusing on a narrow wavelength band where the higher radiation intensities of the solar spectrum occur. However, this would be crucial in obtaining relatively low reflectivity in a specific wavelength range to achieve maximum power conversion efficiency of the solar cell.

Since the CdS window layer absorbs the higher portion of incident light at the 300-520 nm wavelength range before reaching the CdTe absorber layer, this study focused on the 500-900 nm wavelength range (Fig. 2.3) to minimize the front surface reflectivity and enhance the power conversion efficiency of solar cell. According to Fig. 2.3, the maximum radiation intensity of the solar spectrum occurs between 450-550 nm wavelength. Therefore, obtaining minimum reflectance at 520 nm is better for the initial design of AR coating. Furthermore, according to Eq. 1.5, the thickness of AR coating should be around 65 nm, assuming the refractive index of ZnO is about 2 [37].

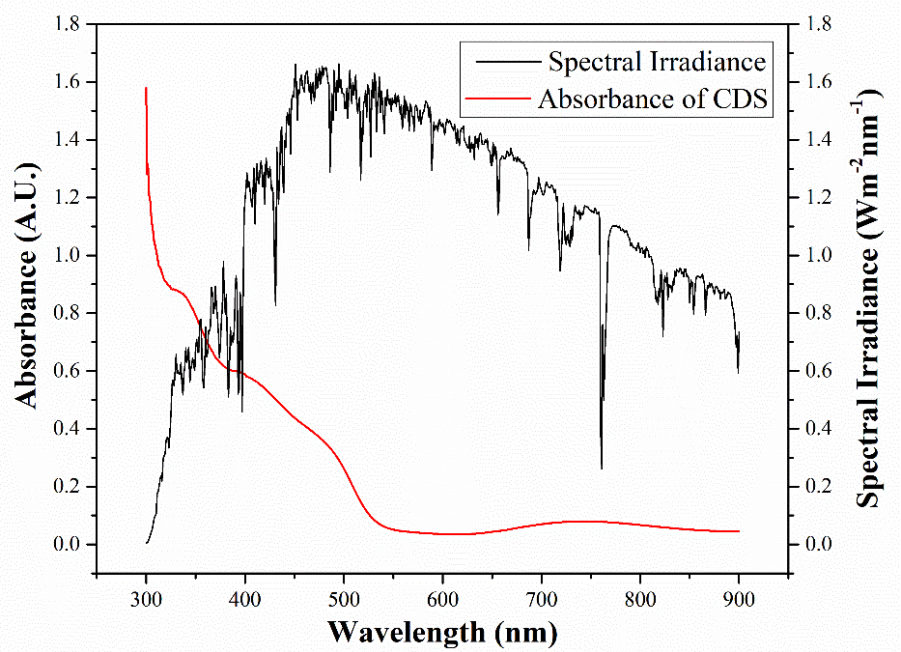

Fig. 2.3: Absorbance spectrum of CdS and solar irradiance spectrum

Using theoretical calculations, a simulation was carried out from PC1D simulation software. The PC1D numerical simulation software is extensively utilized for modelling solar cells. This software was created at the University of New South Wales [66], a globally recognized institution for its contributions to solar cell research. PC1D offers commendable speed, precision, and user-friendliness in its simulations. In this study, PC1D simulation was employed to obtain the reflectance spectrum.

Therefore, the front surface is set as "optically coated" by the ZnO layer. As the layer parameters, thickness and refractive index were entered as 65 nm and 2, respectively. The aim of this simulation study was to validate the theoretical values before the experiment and obtain minimum reflectance between 450-550 nm, where the maximum radiation intensity occurs.

According to Fig. 2.4, bare cells exhibit about 17% reflectance between selected wavelength region. After adding ZnO AR coating, reflectance shows less than 2.5% in the region of 450-550 nm. In particular, the minimum reflectance of 2.25% is obtained at 520 nm wavelength. Therefore, since this numerical simulation agrees with the theoretical results, it would be favorable to fabricate a ZnO coating with a thickness of around 65 nm. Note that, PC1D simulation was carried out just for validation of the theoretical value. The optimization will be done using more test cases in experiment.

However, PC1D is primarily a single-dimensional simulation tool, meaning it assumes that the behavior of carriers and light absorption in the solar cell is primarily one-dimensional along the device's thickness. Moreover, the exact values of material parameters, i.e., thickness and refractive index of ZnO AR coating, can be deviated from the values entered into the simulation software by the user. Therefore, there can be some deviation between simulation results and experimental results.

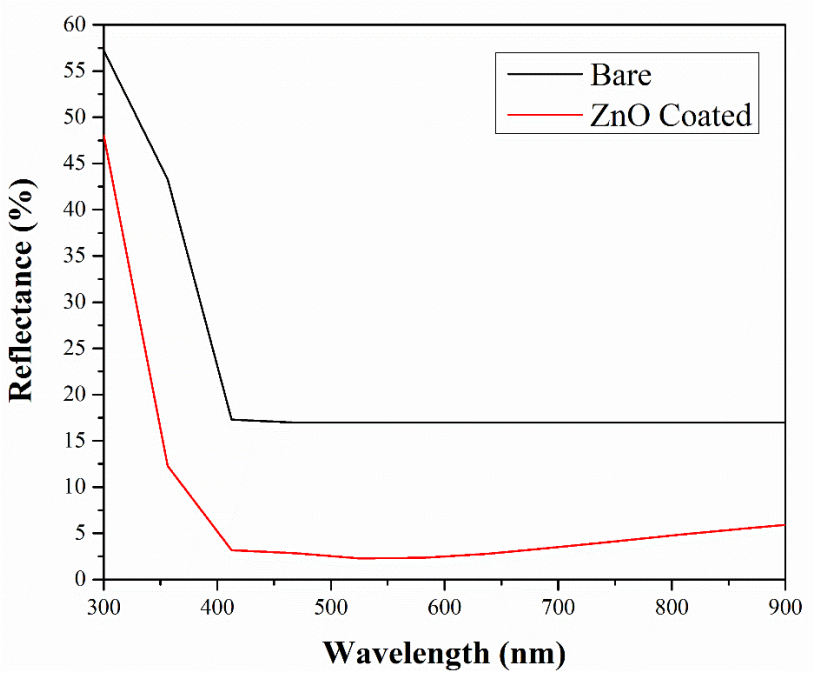

Fig. 2.4: Reflectance spectrum of CdS/CdTe solar cell with and without ZnO AR coating

2.3 Materials and methodology

The thin film ZnO layer was deposited on the borosilicate glass substrate (2.2 x 2.5 cm^2), using the spin coating technique. The spin coating machine (Ossila) used in this experiment has a speed range from 120 to 6000 rpm. The experiment aimed to find the optimum spin rate, solution concentration, and spin time to reach minimum reflectance at 520 nm. The spin rate was obtained from the material characterization in order to achieve minimum reflectance. Moreover, solution concentration and the spin time were kept at a constant value throughout the experiment.

Initially, the glass substrates were subjected to the cleaning process. Herein, glass substrates were washed with detergent, and then, ultrasonically cleaned samples were immersed in acetone, methanol, and 2-propanol at a temperature of 80°C for 5 minutes, respectively, and finally, air-dried. In this study, two methods were tested for depositing a ZnO thin layer on a glass substrate. In the first experiment, ZnO powder was employed as a zinc precursor, and the second experiment used Zinc Acetate as a zinc precursor.

The maximum allowable temperature of the CdS/CdTe solar cell was 150 ^{0}C [63, 64]. Therefore, the post-annealing temperature of the AR coating deposited on the solar cell should be less than 150 ^{0}C; otherwise, the solar cell's performance would be degraded. In this study, the annealing temperature was selected as 100 ^{0}C. Since this temperature is not much higher value, the annealing time was kept at a longer duration (120 minutes).

2.3.1 Fabrication of ZnO layer using zinc oxide powder as zinc precursor

A solubility test was conducted prior to the spin coating process to determine the appropriate alcohol for preparing a ZnO solution. As alcohols, Ethylene glycol, Ethanol, Methanol, Acetone, Dichloromethane, and 2-propanol were considered. Initially, 1 g of ZnO was gradually introduced into 10 ml of the alcohol solutions mentioned above. Subsequently, the mixture underwent a 2-hour heating and stirring process. Figure 2.5 depicts the solubility of ZnO powder after 24 hours waiting period in different alcohol types.

Fig. 2.5: The solubility of ZnO powder in various alcohols

According to the solubility test, the best solubility was obtained from ZnO powder in ethylene glycol, and all other solutions showed suspension at the bottom of the volumetric flask. Then ZnO powder dissolved in an ethylene glycol solution was subjected to a filtering process.

In the next step, ZnO layers were deposited via the spin coating technique by applying a ZnO powder dissolved in ethylene glycol. After the deposition, ZnO films were subjected to post-annealing at 100 ^{0}C for 120 minutes. Fig. 2.6 shows the spin-coated ZnO thin films at 1000 to 3000 rpm at 500 rpm steps.

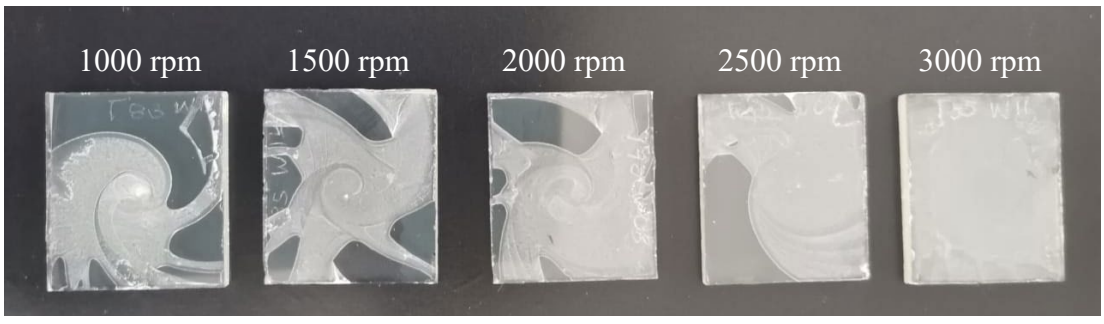

Fig. 2.6: ZnO Coating Deposited on Glass Substrate at various spin rates

According to Fig. 2.6, it is clear that the uniformity of the layer is increased with the spin rate. However, the transparency of the layer was not sufficient for the AR coating because a high-quality AR coating is transparent, meaning it does not significantly

affect the clarity of the underlying material while reducing reflections. Moreover, the deposited layer was not adhere well and at 100°C, ZnO may not fully crystallize, resulting in an amorphous or poorly defined film. Therefore, this layer could not be used for the AR purpose with the limitations of the deposition methodology.

Subsequently, zinc acetate was employed as a zinc precursor.

2.3.2 Fabrication of ZnO layer using zinc acetate as zinc precursor

A ZnO solution was prepared by dissolving 1 g of zinc acetate ($Zn(CH_3COO)_2$) in 25 ml of methanol, and then it was gravity-filtered. Prior to the spin coating process, boro-silicate substrates were subjected to plasma cleaning in O_2 ambient. Thereafter, spin coating was performed at 2000 rpm. The ZnO thin layer was developed by adding 0.75 ml of aforesaid $Zn(CH_3COO)_2$ drops into the center of the substrate immediately starting the spinning, and it was maintained for 15 s. After the deposition, samples were heat treated at 100 ºC for 120 min in atmospheric pressure by tube furnace (GSL-1700X). The visual image showed that the coated layers were not uniform and contained some holes throughout the layer (Fig. 2.7).

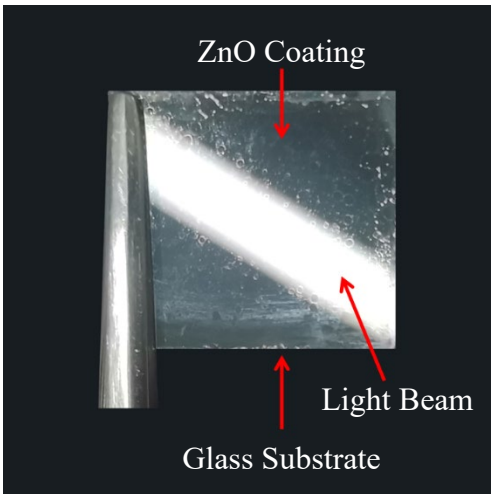

Fig. 2.7: The case of low $Zn(CH_3COO)_2$ concentration

Subsequently, the $Zn(CH_3COO)_2$ quantity was increased to 1.7 g in 25 ml of methanol. Fig. 2.8 shows the visual image of ZnO coating coated at 2500 rpm. According to the image, it can be identified that the uniformity of the layer is good, and therefore, $Zn(CH_3COO)_2$ concentration was set as the aforementioned value for further experiments. Note that, the first goal of this deposition was depositing uniform ZnO layer for visible eye and then thickness and reflectance were considered.

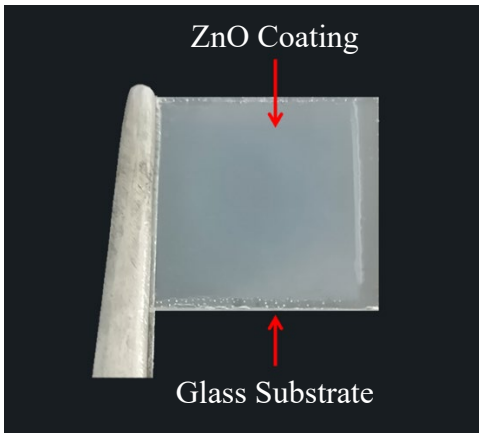

Fig 2.8: The case of uniform ZnO layer

After identifying the optimum concentration of the ZnO solution, three separate spin times were considered. Herein, three ZnO layers were deposited at 2500 rpm and spin time set as 5, 10 and 15 s, respectively. Fig. 2.9. shows the absorbance spectrum of three samples.

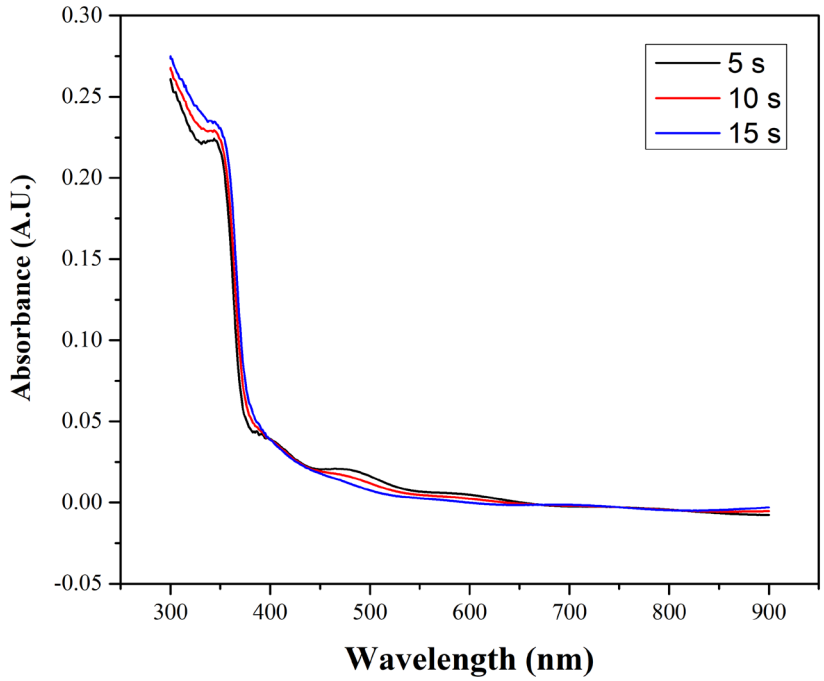

Fig. 2.9: Optical absorbance vs. wavelength plot of the ZnO coatings at three different spin rates

As depicted in Fig. 2.9, the absorbance spectra exhibit minimal variation. Nevertheless, it can be observed that the curve associated with a 5 s spin time displays irregularities between 350-650 nm wavelength region, which may be due to a interference fringes and it is an indication that there is a thickness variation. Consequently, in order to ensure uniformity and the better spreading area of the layer, a spin time of 15 seconds was chosen for subsequent experiments.

Apart from the optimum concentrations and spin time, an unusual parameter to consider is the drop height from the tip of the pipette to the substrate. Since the

deposited layer is extremely thin, in the nanometer range, it is crucial to ensure that the solution drop, released from the pipette, falls from a height of less than 1 cm. Fig. 2.10 illustrates a visual representation of the ZnO layer deposited at 2500 rpm, with the drop height being maintained at a higher level.

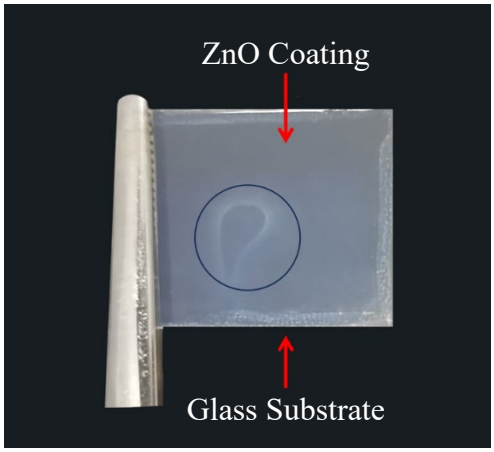

Fig. 2.10: The case of uniform ZnO layer due to higher solution drop height.

After identifying all concerning factors, a set of thin film ZnO samples was spin coated at speeds of 1000-3500 rpm at a step of 500 rpm while maintaining other parameters constant. The samples denoted as S1, S2, S3, S4, S5, and S6 as shown in Table 2.1.

TABLE 2.1: SAMPLE LABELING WITH RESPECT TO THE SPIN RATE

Spin rate (rpm)	Label
1000	S1
1500	S2
2000	S3
2500	S4
3000	S5
3500	S6

The characterization was carried out for the ZnO layers deposited at aforementioned rpm values. Therefore, the aim was to select the best rpm value to fabricate ZnO AR coating on a laboratory-developed glass/FTO/CBD-CdS/CSS-CdTe/Cu/Au substrate.

2.4 Characterization

The absorbance and transmittance spectrum of the ZnO layer was obtained by UV visible spectroscopy (PerkinElmer UV/VIS Lambda 365) in the wavelength range of 300 to 900 nm. The front surface reflectance spectrum of the coated substrate was carried out by Bentham EQE setup (PVE300) to identify the best rpm value of the spin coater in order to achieve minimal reflectance. Moreover, the thickness of the ZnO coating was measured by a profilometer (DektacXT). The atomic force microscope (AFM) (Bruker AFM dimension edge) analysis was performed to analyze the RMS roughness and the energy-dispersive X-ray spectroscopic (EDAX ELEMENT)

analysis was performed to and identify the composition of the grown material of the optimized sample. Ultimately, the performance of the solar devices, glass/FTO/CdS/CdTe/Cu/Au, with and without the AR coating, were measured under the illumination condition of AM 1.5, (100 mW/cm²) using a solar simulator (PEC-L12).

Note that, for optical measurements (UV visible), the effect of substrate was calibrated before taking the measurements. This calibration helps to account for any absorbance or reflectance contributions from the substrate itself.

2.5 Results and discussion

2.5.1 The theoretical background of the formation of the ZnO

The chemical reaction of zinc acetate ($Zn(CH_3COO)_2$ (s)) and methanol (CH_3OH (aq)) is an esterification reaction that produces byproducts of methyl acetate (CH_3COOCH_3 (aq)) and zinc hydroxide ($Zn(OH)_2$ (aq)) as represented in reaction Eq. 2.1.

$$Zn(CH_3COO)_2\,(s) + 2\,CH_3OH\,(aq) \rightarrow 2\,CH_3COOCH_3\,(aq) + Zn(OH)_2\,(aq) \qquad \textbf{Eq. 2.1}$$

Since the boiling point of CH_3COOCH_3 (aq) is about 57°C [67] at standard atmospheric pressure (1 atm), at temperatures above 57 °C, methyl acetate is vaporized (reaction Eq. 2.2). Herein, when the spin coated material is subjected to thermal annealing at 100 °C, ZnO (s) film is formed by dehydration of $Zn(OH)_2$ (aq) (reaction Eq. 2.3).

$$CH_3COOCH_3\,(aq) \rightarrow CH_3COOCH_3\,(g) \qquad \textbf{Eq. 2.2}$$

$$Zn(OH)_2\,(aq) \rightarrow ZnO\,(s) + H_2O\,(g) \qquad \textbf{Eq. 2.3}$$

2.5.2 Optical properties

The optical transmittance of the ZnO layers, grown under the different spin rate, are shown in Fig. 2.11. Herein, the ZnO layer deposited with low spin rates (S1 and S2) showed over 95% transmittance of light in the wavelength range of 500–900 nm. However, when the spin rate increased, the maximum transmittance (>95%) was occurred at a broader wavelength range. Consequently, the samples obtained at high spin rates (S5 and S6) showed over 95% transmittance of light in the wide optical range of 400–900 nm.

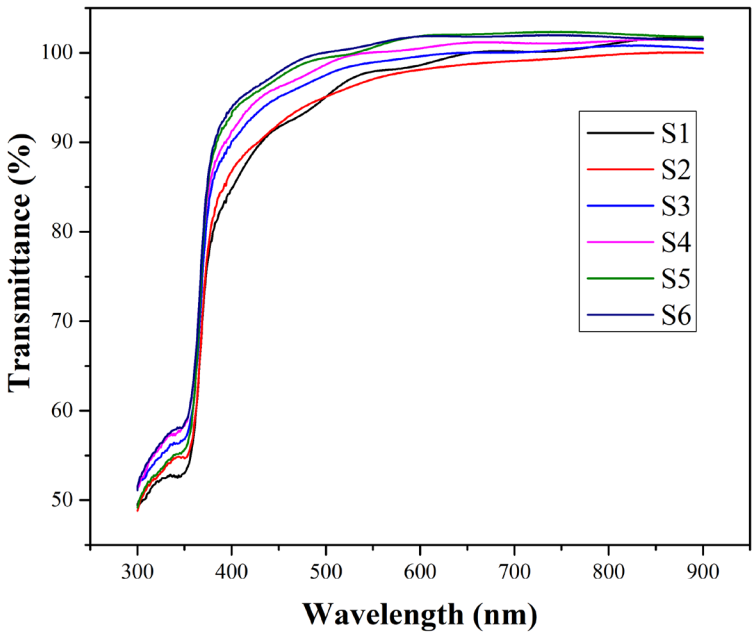

Fig 2.11: Optical transmittance vs. wavelength plot of the ZnO AR coatings (S1 to S6)

Fig. 2.12 (a) depicts the optical absorbance of the growth ZnO layers, while Fig. 2.12 (b) represents the relevant Tauc plots for the samples deposited in different spin rates. The ideal AR coating shows minimal absorbance across the spectrum, allowing most incident light to pass through the layer. The theoretical band gap energy of the ZnO is about 3.37 eV [68], corresponding to the wavelength of 368 nm. In detail, ZnO is more transparent to light in wavelengths longer than 368 nm and absorbs light with shorter wavelengths (less than 368 nm). According to the absorbance spectrum, all samples delivered 0.225-0.35 A.U. (absorption units) absorbance in the wavelength of 300-350 nm. The absorbance of the sample S6 to S1 further declined closer to zero when the wavelength varied from 500 nm to 900 nm. The samples S5 and S6, of which the ZnO layers were coated at 3000 and 3500 rpm and had higher light transmittance, were identified as the best AR coating in this study and further analysis is to be done for selecting optimum parameters.

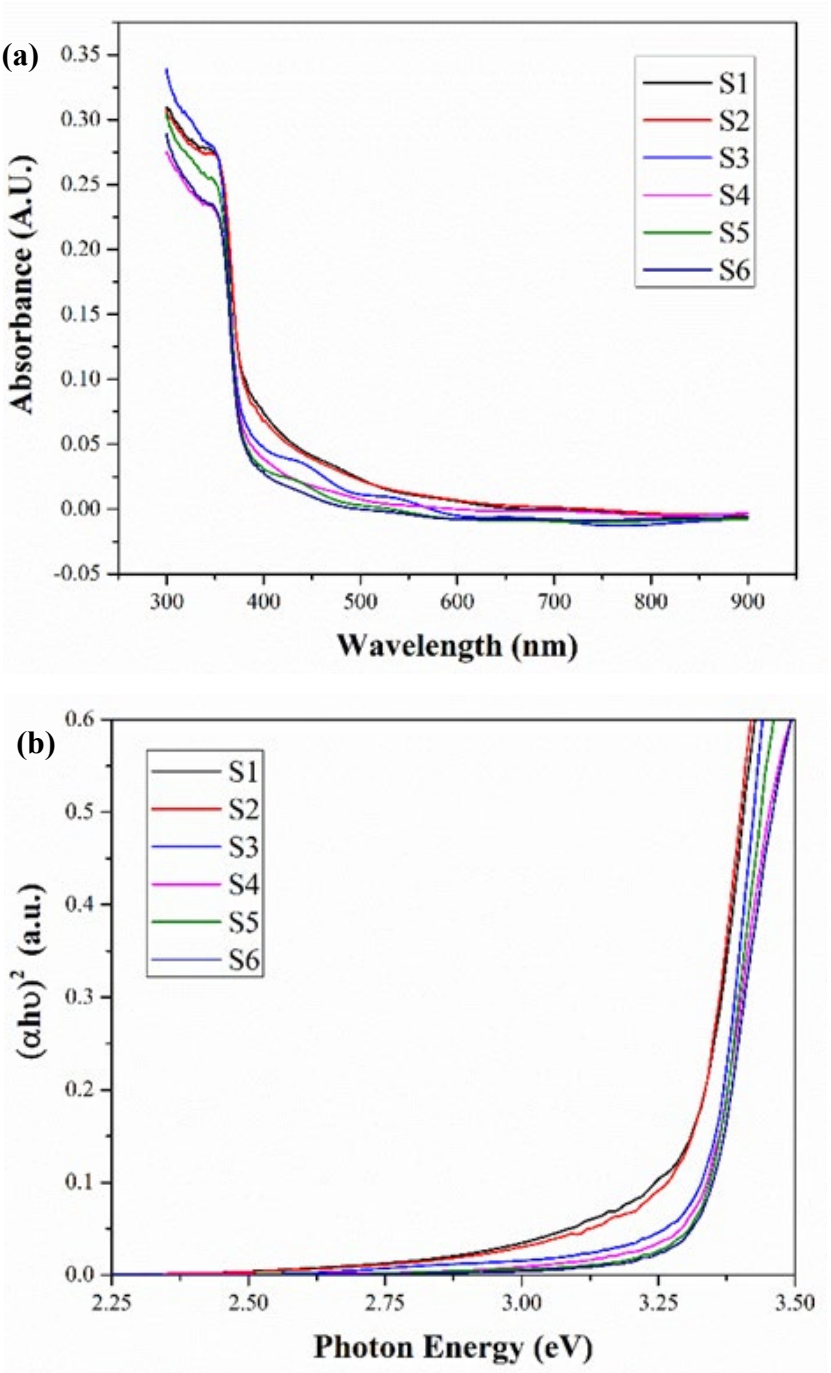

Fig. 2.12: (a) Absorbance vs wavelength plot and **(b)** Tauc plot for the ZnO AR coatings S1 to S6

Table 2.2 illustrates the energy band gap values (E_g) of samples S1 to S6 determined from the Tauc plots. Here, using the extrapolate method, extend the linear portion of the plot to intersect the x-axis and the point where the line intersects the x-axis corresponds to the optical bandgap of the material. It observes that the band gap value slightly increased proportional to the spin rate. The ZnO in S0 and S1 have lower band gap values than its theoretical value (3.37 eV). However, the band gaps of S4 to S6 reached the theoretical value of ZnO. Note that, thinner films can exhibit larger bandgaps due to quantum confinement effects [69] (quantum confinement refers to the phenomenon where the electronic and optical properties of a semiconductor material

change when its dimensions are reduced). In these films, the reduced thickness leads to increased energy levels for the electrons, which can cause a widening of the bandgap. Moreover, higher RPMs often lead to more uniform and smoother films. Better uniformity can reduce the occurrence of structural defects and improve the optical properties of the film.

Accordingly, the optical properties of samples S4 to S6 serve as an excellent representation to ensure the growth material is similar to the ZnO.

TABLE 2.2: THE ENERGY BAND GAP OF THE SAMPLE S1 TO S6 W.R.T SPIN RATE

Sample	S1	S2	S3	S4	S5	S6
Spin rate (rpm)	1000	1500	2000	2500	3000	3500
Energy bandgap (eV)	3.29	3.28	3.31	3.32	3.32	3.32

The reflectance spectrum of samples S1 to S6 between the wavelength range of 300-900 nm is shown in Fig. 2.13. The highest intensity peak of reflectance was observed at a particular wavelength due to the phenomenon of constructive interference. Constructive interference occurs when waves reflected from the front and back surfaces are in the same phase and results in an intense peak in the spectrum.

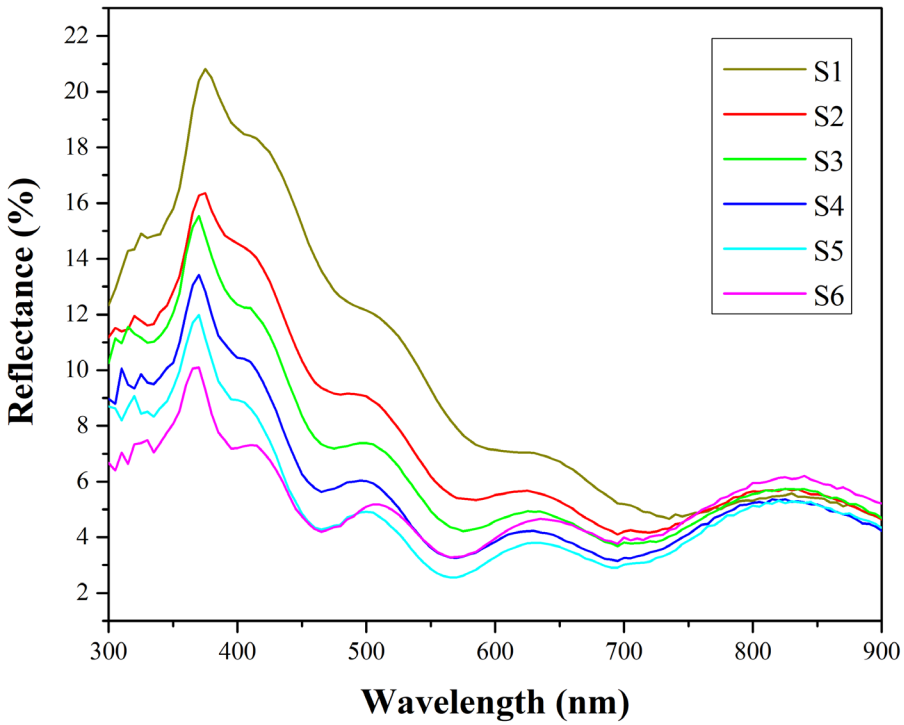

Fig 2.13: Reflectance vs. wavelength plot of the ZnO AR coatings S1 to S6

As Fig. 2.13, the lower reflectance was observed by the samples S5 and S6 at the wavelength of 375 nm. Further, the sample S5 has the lowest reflectance over the wavelength range of 500-900 nm. Lower the reflectance, better the light transmission. Therefore, S5 was identified as the ideal AR coating among the studied samples.

2.5.3 Variation of AR coating thickness

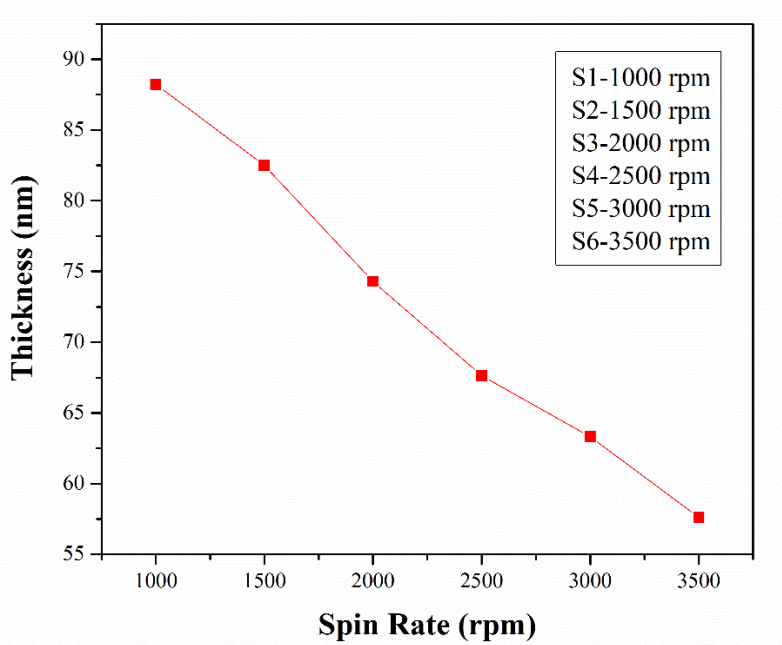

Fig 2.14: Thickness of the ZnO AR coating vs. spin rate of deposition

Fig. 2.14 shows the variation in thickness of the ZnO layer with the spin rate. Therein, the thickness of the AR coating decreased (from around 90 nm to 55 nm) with the increase of the spin rate (1000-3500 rpm). When the thickness increases from 55 to 90 nm, the variation of light reflectance around 375 nm (Fig. 2.13) ranged in 21% (S1, 88.22 nm) to 10% (S6, 57.62 nm). Moreover, when the thickness of the AR coating increases, the optical path length that the light waves traverse through the coating also increases, which leads to maximizing the peak reflectance.

The reflectance of all samples tends to decline further after the peak point of the spectrum. This may occur due to destructive interference. As the thickness changes, minimum reflectance due to destructive interference occurs at different wavelengths of the samples S1 to S6 in 300-900 nm wavelength region as shown in Table 2.3.

TABLE 2.3: MINIMUM REFLECTANCE WITH CORRESPONDING WAVELENGTH OF THE SAMPLES S1 TO S6

Sample	S1	S2	S3	S4	S5	S6
Thickness (nm)	88.22	82.5	74.3	67.64	63.32	57.62
Wavelength (nm)	735	720	695	690	570	565
Minimum reflectance (%)	4.6	4.1	3.6	3.1	2.5	3.2

According to Table 2.3, the minimum reflection was shifted towards a shorter wavelength when thickness was reduced. The minimum reflectance of 2.5% at 570 nm was observed from sample S5, which has a thickness of 63.32 nm. Hence, sample S5 fulfilled the requirement of AR coating having closer value to the calculated theoretical value (65 nm) in the initial experimental design. This further validated the results of the initial design. However, according to Fig. 6 and Table 2, sample S6 shows more

reflectance than sample S5 despite the thickness being lower than S5. Therein, further reduction of the thickness beyond 63.32 nm may not be effective in reducing the reflectance. Therefore, there is an optimum thickness for AR coating that maximizes destructive interference and provides minimum reflectance.

2.5.4 Surface analysis

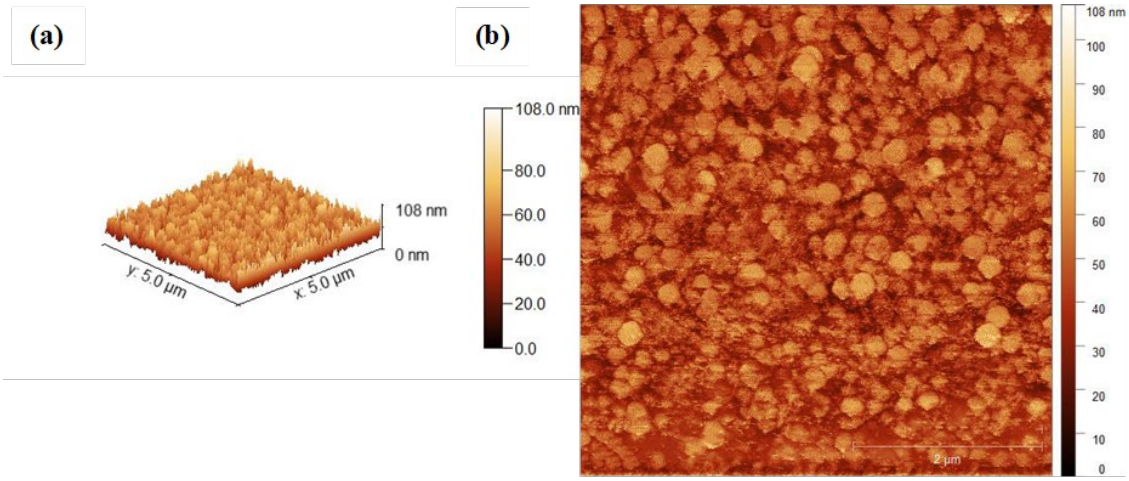

Fig 2.15: (a) 3D and **(b)** 2D AFM images of ZnO surface deposited at 3000 rpm

After identifying the best AR coating, the sample S5, further analysis was performed to determine the surface topography and its elemental analysis. Fig. 2.15 Shows the AFM images of the spin coated ZnO at 3000 rpm (S5). The root mean square (RMS) roughness of sample S5 was measured as 11.44 nm, while the roughness of the bare surface was 7.86 nm. Hence, it is evident that the resultant increase of the substrate roughness is due to the ZnO AR coating. This AR coating may enhance the light-trapping ability of the device. When light hits the device, some can be reflected due to the refractive index difference between the two mediums. The presence of a rough surface can cause multiple reflections and increase light entering the device, leading to improved current density and power conversion efficiency.

2.5.5 Composition analysis

The composition of glass/FTO/ZnO is indicated in Table 2.4. Therein, the ZnO layer was deposited on the FTO layer (because FTO is conductive and glass is nonconductive) for the convenience of the measurement from EDX equipment. Accordingly, the formation of the ZnO was confirmed.

TABLE 2.4: COMPOSITION OF ZNO SAMPLE GROWN ON FTO/GLASS SUBSTRATE

Element	Weight (%)	Atomic (%)	Error (%)
O	13.75	48.55	8.92
Si	5.09	10.23	8.11
Sn	74.47	35.44	1.83
Zn	6.68	5.77	10.56

2.5.6 Device characterization (IV measurements)

The laboratory developed device glass/FTO/CBD-CdS/CSS-CdTe/Cu/Au [65] was then completed by depositing the AR coating of ZnO following the sample preparation of S5. Fig. 2.16 shows the J-V curves of three devices with and without AR coating.

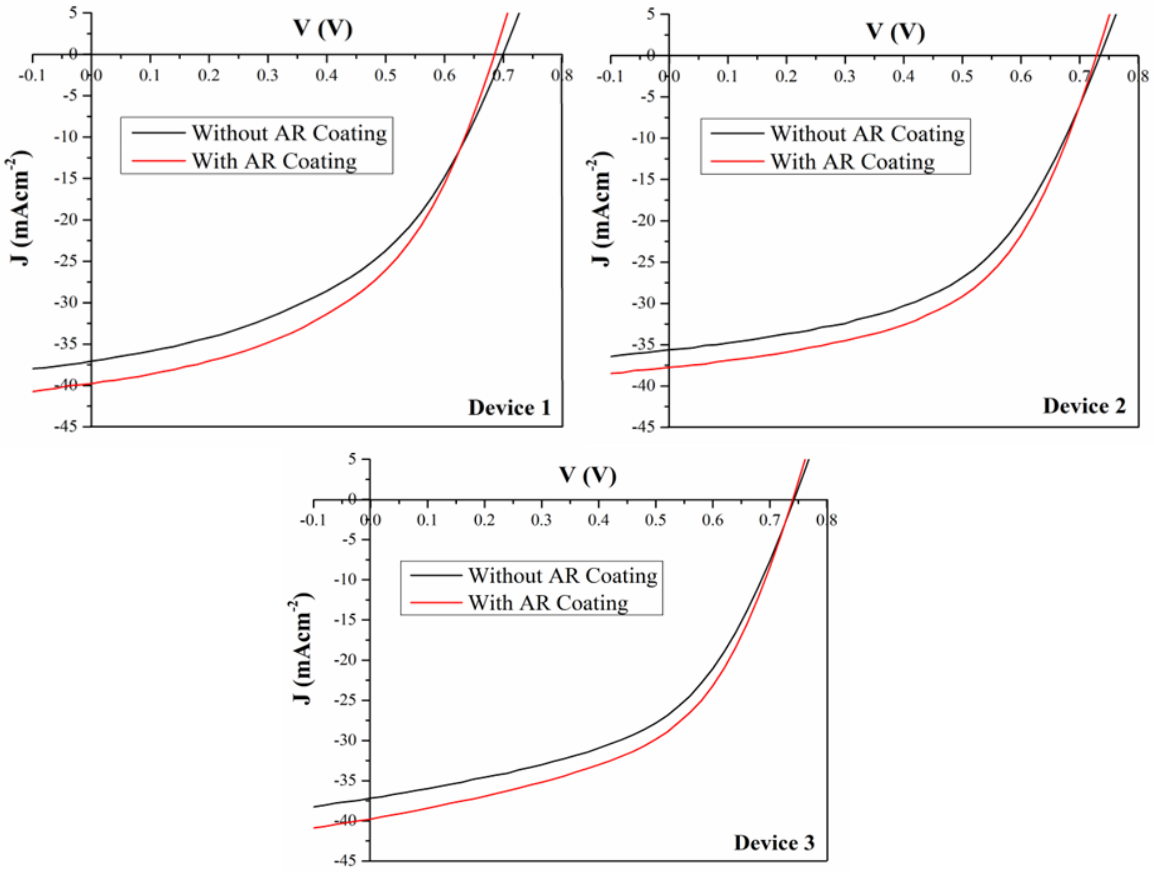

Fig. 2.16: J-V curves for the devices 1, 2 and 3

After introducing the AR coating, the light passed through the coating and into the cell was increased due to a reduction of reflectance, which caused more photons to absorb into the device, leading to a higher generation of electron-hole pairs. As a result, more charge carriers are available and hence increase the current density. Table 2.5 illustrates the measured electrical parameters of aforementioned devices with and without AR coating.

TABLE 2.5: ELECTRICAL PROPERTIES OF THE DEVICE 1, 2 AND 3

		J_{SC} ($mAcm^2$)	V_{OC} (V)	FF (%)	PCE (%)
Device 1	Bare	37.1	0.699	46.1	11.9
	With AR	39.8	0.685	48.2	13.2
Device 2	Bare	35.5	0.734	51.3	13.4
	With AR	37.7	0.729	53.2	14.6
Device 3	Bare	37.2	0.742	50.6	13.9
	With AR	39.8	0.740	51.1	15.0

According to Table 2.5, it is clear that enhancement of *PCE* is occurred due to the improvement of J_{SC}. Additionally, the enhancement of J_{SC} and *PCE* is shown in Table 2.6 up to six devices.

TABLE 2.6: COMPARISON OF THE PERFORMANCE OF THE DEVICES

		J_{SC} ($mAcm^2$)	J_{SC} Improvement	PCE (%)	PCE Improvement
Device 1	Bare	37.1	**7.3%**	11.9	**10.9%**
	With AR	39.8		13.2	
Device 2	Bare	35.5	**6.2%**	13.4	**9.0%**
	With AR	37.7		14.6	
Device 3	Bare	37.2	**6.2%**	13.9	**7.9%**
	With AR	39.8		15.0	
Device 4	Bare	34.8	**7.7%**	12.2	**9.8%**
	With AR	37.6		13.4	
Device 5	Bare	37.2	**6.7%**	13.3	**8.2%**
	With AR	39.7		14.4	
Device 6	Bare	37.7	**6.9%**	12.3	**9.8%**
	With AR	40.3		13.5	
	Average		**6.8%**		**9.3%**

2.6 Summary

In this chapter, optimal condition for the growth of ZnO AR coating using the spin coating technique was identified as 3000 rpm for 15 s using the zinc acetate precursor dissolved in methanol. Furthermore, minimal reflectance (2.5%) and surface roughness (11.44 nm) confirmed the suitability of the growth ZnO as an AR coating. Additionally, after introducing the optimized ZnO AR coating, the overall current density and power conversion efficiency of the laboratory developed CdS/CdTe solar cells were enhanced by 6.8% and 9.3%, respectively. Therefore, the spin coated ZnO is a suitable AR coating for the CdS/CdTe solar cell devices.

CHAPTER 3

IMPROVEMENT OF CdS/CdTe SOLAR CELL'S PERFORMANCE USING SIMULATION STUDY

3.1 Introduction

The major reasons for a significant drop in the efficiency of the thin-film solar cell were determined to be a reflection at the front surface and recombination. In the previous chapter, AR coating was introduced to reduce the reflection at the front surface. Therefore, this chapter discusses the introduction of the back surface field (BSF) layer to address the recombination issue at the back surface of the absorber layer in the CdS/CdTe solar cell using a simulation study.

Numerical simulation is an essential modelling tool to examine the performance of solar cells with the variation of the properties of the materials and the structural changes of the solar cell. In this study, Solar Cell Capacitance Simulator – One Dimension (SCAPS-1D) simulation software was utilized to interpret the device parameters of the CdS/CdTe solar cell.

When simulating solar cells, there can be discrepancies between the simulation results and experimental measurements. Therefore, prior to this investigation, a simulation will be performed using the actual laboratory developed CdS/CdTe solar cell's parameters for the purpose of software validation. Thereafter, the optimized values of possible layer parameters, such as layer thickness and material concentration, that can be considered for further experiments will be obtained. Finally, using the optimized results, the effect of the BSF layer will be analyzed.

3.2 Device and Simulation

3.2.1. SCAPS-1D simulation software

The SCAPS-1D software is the solar cell simulation software developed to predict cell performance based on the material properties, invented at Belgium's University of Ghent [70]. The working principle of the SCAPS-1D software is built on the Poisson's equation represented in Eq. 3.1, and the continuity equations for electrons and holes are denoted in Eq. 3.2 and 3.3 [70, 71].

$$\frac{\partial^2 \Psi}{\partial x^2} + \frac{q}{\varepsilon \varepsilon_0}\left[P(x) - n(x) + N_D^+ - N_A^- + \frac{\rho_{\text{def}}(n,p)}{q}\right] = 0 \qquad \textbf{Eq. 3.1}$$

The symbols Ψ, ε, ε_o and q denote the electrostatic potential, dielectric constant, permittivity in vacuum and electron charge, respectively. Similarly, n, p are electron and hole concentrations, N_D and N_A are donor and acceptor densities, and ρ_{def} is the defect density.

$$\frac{dn}{dx} = \frac{1}{q}\frac{dJ_n}{dx} + (G_n - R_n)$$ **Eq. 3.2**

Here, $J_n = -\frac{\mu_n n}{q}\frac{\partial F_{En}}{\partial x}$

$$\frac{dp}{dx} = \frac{1}{q}\frac{dJ_p}{dx} + \left(G_p - R_p\right)$$ **Eq. 3.3**

Here, $J_p = +\frac{\mu_p p}{q}\frac{\partial F_{Ep}}{\partial x}$

Where, R_n, R_p are the recombination rate of electrons and holes, G_n, G_p, are the generation rate of electrons and holes and J_n, J_p is the current density of electrons and holes, respectively. Moreover, μ_n, μ_p are electron and hole mobility and F_{En}, and F_{Ep} are Fermi levels of n-type and p-type carriers of materials. Finally, the software algorithm generates a set of coupled differential equations with boundary conditions at the front and rear contact surfaces and computes the quasi-fermi level and electrostatic potential at all solar cell points for the holes and electrons.

3.2.2. Data collection and executing the simulation

The first stage of the simulation study was based on comparing CdS/CdTe solar cells under simulated and experimental conditions. Therefore, the most critical parameters, such as bandgap and layer thickness that affect the solar cell performance, were measured, and those measured values were used for the simulation study. Fig. 3.1 depicts the thicknesses of each layer in the FTO/CdS/CdTe solar cell.

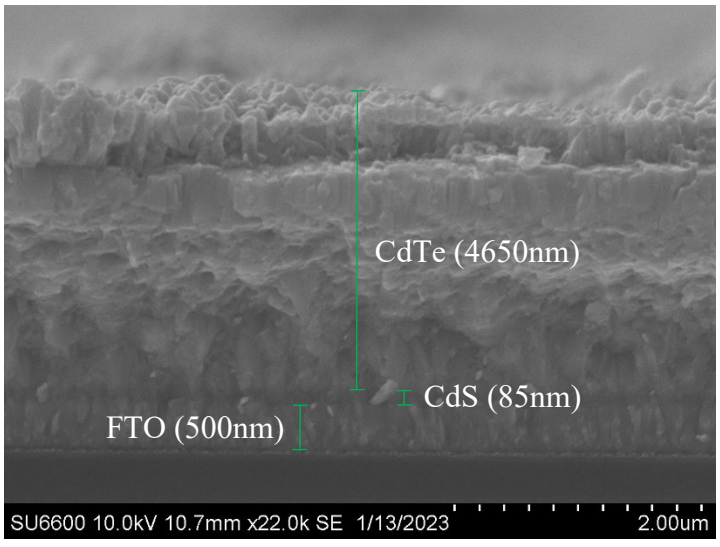

Fig. 3.1: Thickness measurement of FTO/CdS/CdTe solar cell

The bandgap of the CdS and CdTe layers was obtained from the tauc plots of each layer shown in Fig. 3.2 and 3.3, respectively.

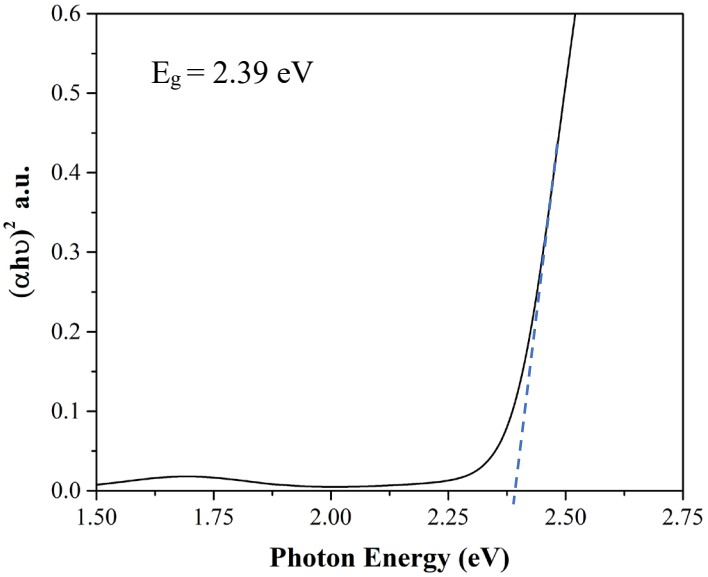

Fig. 3.2: Tauc plot of CdS

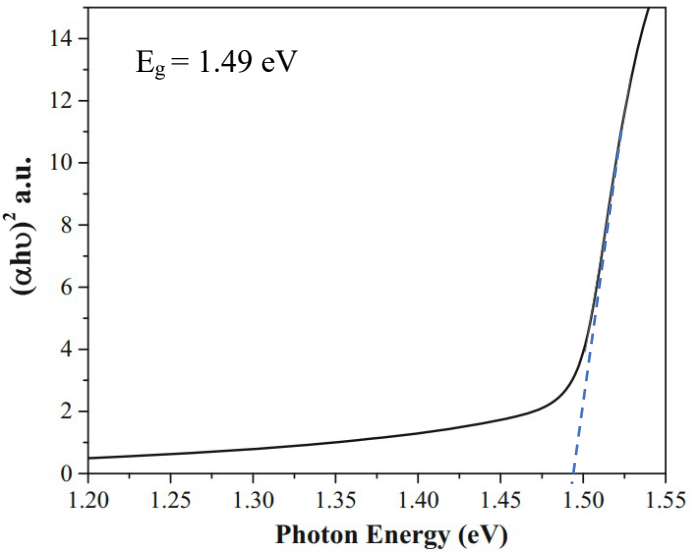

Fig. 3.3: Tauc plot of CdTe

Additionally, the bandgap of the FTO layer was extracted from the manufacturers' data sheet, and the donor density of the CdS layer and acceptor density of the CdTe layer were actual measured values during the fabrication of the solar cell [63, 64]. Moreover, other parameters were selected based on the literature, and simulation were performed under the experimental illumination condition of 100 mW/cm^2 (1.5 AM) at 300 K. Moreover, other parameters were selected based on the literature [72–76]. The parameters of the conductive (FTO), window (CdS) and absorber (CdTe) layers as mentioned in Table 4.1.

TABLE 3.1: LAYER PARAMETERS

Parameters	FTO	CdS	CdTe
Thickness (nm)	500	85	4650
Bandgap (eV)	3.5	2.39	1.49
Electron affinity (eV)	4.5	4.5	4.28
Dielectric permittivity	10	10	9.4
CB effective density states ($1/cm^3$)	$2*10^{18}$	$2.2*10^{18}$	$8*10^{17}$
VB effective density states ($1/cm^3$)	$1.8*10^{19}$	$1.8*10^{19}$	$1.8*10^{19}$
Electron mobility (cm^2/Vs)	100	100	320
Hole mobility (cm^2/Vs)	20	25	40
Shallow uniform donor density N_D ($1/cm^3$)	10^{15}	10^{18}	0
Shallow uniform acceptor density N_A ($1/cm^3$)	10^{15}	0	10^{17}
Defect type	-	Donor	Acceptor
Defect density ($1/cm^3$)	-	10^{17}	10^{15}

The laboratory-developed device structure, glass/FTO/CdS/CdTe/back contact, illustrated in Chapter 2, Fig. 2.1, and Fig. 3.4, shows the software representation of the solar cell.

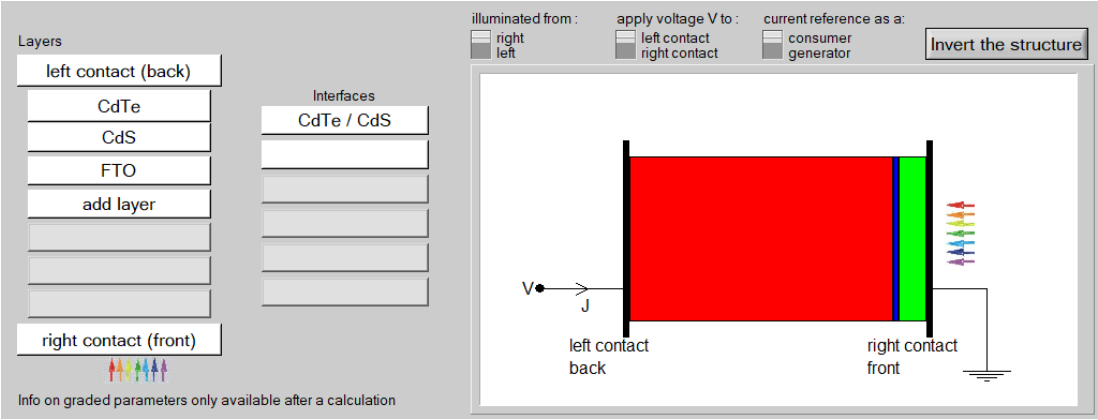

Fig. 3.4: Software interpretation of the laboratory-developed solar cell

In the subsequent phase of this study, Tin (II) Sulfide (SnS) was investigated as a potential back surface layer in CdTe solar cells via simulation study. The goal was to minimize the thickness of the CdTe absorber layer and enhance the overall efficiency of CdTe solar cells by reducing the recombination at back surface of the absorber layer.

Herein, the choice of a BSF layer depends on several factors, including the material properties, ease of deposition, cost, and the specific requirements of the solar cell fabrication methodology. SnS (Tin Sulfide) is a semiconductor that has become one of the top choices for the absorber layer in thin-film solar cells over recent years [77–79]. Therefore, SnS can be considered as one of the best materials for BSF layer given that the BSF layer shares the same p-type characteristics.

SnS emerges as a promising alternative for second-generation photovoltaic solar cells due to its composition of cost-effective, abundant, and environmentally friendly

materials. Specifically, SnS exhibits a notable optical absorption coefficient exceeding 5×10^4 cm^{-1} and a direct energy bandgap ranging from 1.00 to 1.32 eV [80].

Regarding deposition methods, various chemical deposition techniques have been employed for the fabrication of SnS thin films. Among those methods, that are available in Sri Lanka include, chemical bath deposition [81], electrodeposition [82], and spin coating [83]. Notably, sol-gel spin coating stands out as a straightforward and cost-effective approach compared to other chemical methods. Moreover, the deposition of layers of the laboratory-developed device starts with the CBD-CdS and then CSS-CdTe. Hence, the fabrication of the SnS layer should be employed after the aforementioned layers and on the back surface of the CdTe layer. Since the p-n junction is already created at this point, the device performance should be secured upon fabrication of the SnS layer. Therefore, the simplest spin coating technique method can be proposed, which also ensures cost-effective fabrication. According to the literature [84], the solvents for fabricating SnS can be proposed as Tin(II) chloride dihydrate ($SnCl_2$ $2H_2O$) for tin and thiourea (CH_4N_2S) for sulfide. Therefore, using P^+ SnS layer alongside the CdTe absorber provides an opportunity to reduce the thickness of the CdTe layer, consequently lowering manufacturing costs.

3.3 Results and Discussion

3.3.1 Numerical investigation of the laboratory developed CdS/CdTe solar cell

The simulated and the experimental short circuit current density vs voltage (J-V) characteristic curves are shown in Fig. 3.5. Herein, the experimental data was extracted from device 3 mentioned in the section 2.5.6. The J_{SC}, V_{OC}, *FF*, and *PCE* of the simulated and experimental conditions were 27.7 $mAcm^{-2}$, 0.71 V, 77.8%, 15.2% and 37.2 $mAcm^{-2}$, 0.74 V, 50.6%, 13.9%, respectively. Therein, the experimental values of *FF* and *PCE* are lower than those of the simulated results. The experimental value of V_{OC} shows slight variation, which can happen due to simulation limitations. However the experimental value of J_{SC} is higher than the simulated and theoretical value (30 $mAcm^{-2}$) [85].

The reason for the high current density is the presence of defect levels within the CdTe material [86]. These defects introduce additional energy states within the bandgap, which can enhance the absorption of light and increase the generation of electron-hole pairs. As more carriers are created, the current density rises because more electrical current is generated. Hence, it may happen in the dramatic increment of the J_{SC} than its theoretical value in the experiment.

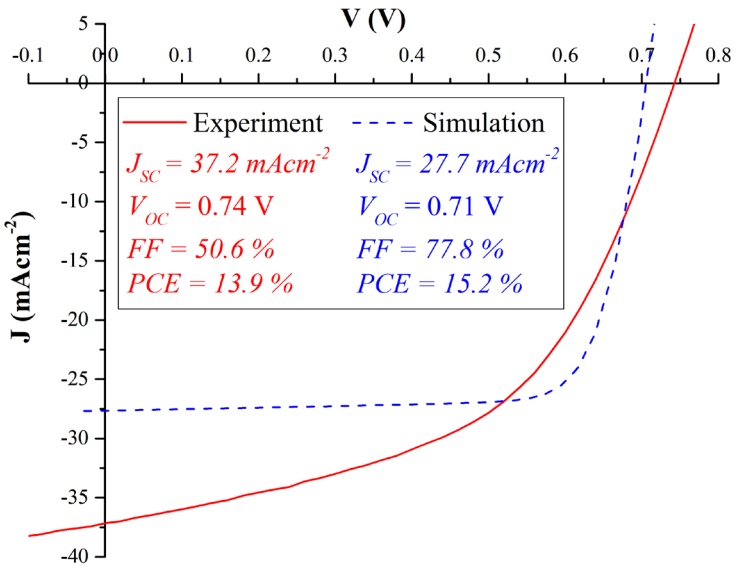

Fig. 3.5: J-V characteristics curve for simulated and experimental CdS/CdTe solar cells

The simulated results represented in Figure 3.6 show the variation in the J_{SC}, V_{OC}, *FF*, and *PCE* with respect to the energy band gap (E_g) of the CdTe within the range of 1.1–1.7 eV while keeping other parameters constant. According to the simulation, J_{SC} increases while decreasing the E_g of the absorber layer, and it exceeds 30 mA/cm^2 below the E_g value of 1.45 eV (< 1.45 eV). When the E_g of the absorber material is low, less energy is required to excite electrons from the valence band to the conduction band. This results in the improvement of the number of carriers generated, which is directly proportional to the higher J_{SC} in the solar cell. Therefore, the reason for the higher J_{SC} in the experiment might be the presence of a defect state, which is lower than the energy band gap of CdTe (1.49 eV). Therefore, it should be considered about the formation of defect levels in future experiments.

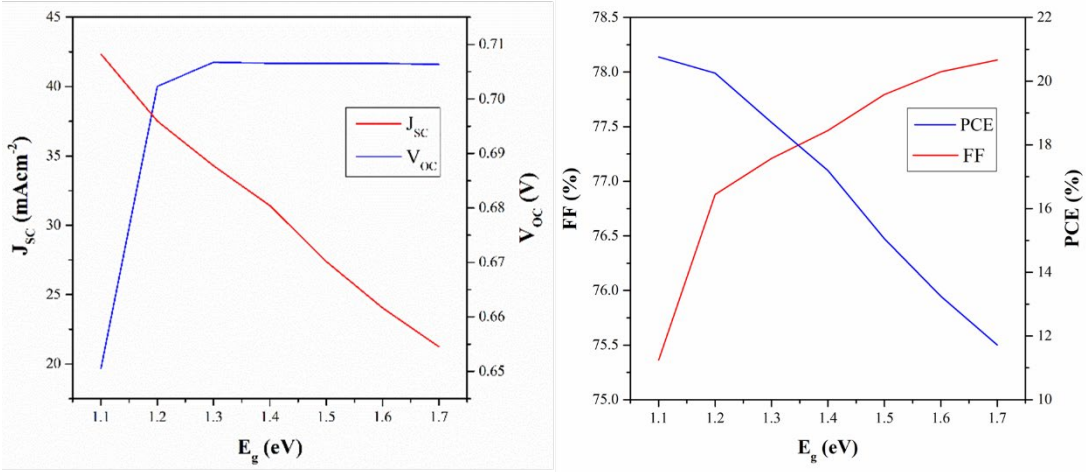

Fig. 3.6: The cell performance on the energy band gap of the CdTe absorber layer

Furthermore, the value of *FF* and *PCE* in the experiment is lower than the simulated values. The *FF* mainly depends on the series (R_s) and shunt resistance (R_{sh}) of the solar cell. In an idealized solar cell model, the R_s is often assumed to be zero, and R_{sh}

assumes to be infinite. However, in a practical scenario, R_s should be as small as possible, and R_s should be higher. In this experiment, R_s and R_{sh} were measured as 67 Ω and 839 Ω, respectively, and that needed to be optimized in future. Therefore, this resulted in the lower FF in the experiment. To improve the *FF*, we can consider the purity of the material, the design of electrical contacts, advanced junction design such as the BSF layer, and the use of additional light absorption techniques such as AR coating, etc. According to Eq. 1.4, *PCE* depends on the J_{SC}, V_{OC} and *FF* and the variation of simulated and experimental values are caused by the difference aforementioned factors.

3.3.2 Influence of the absorber layer thickness on the device performance.

The CdTe absorber layer thickness changed from 0.3 to 4.65 µm, and Figure 3.7 depicts the variation of the J_{SC}, V_{OC}, *FF*, and *PCE* with the layer thickness. As the simulated results J_{SC}, V_{OC}, *FF*, and *PCE* have exhibited a proportional relationship with the increment of the layer thickness.

As the thickness of the absorber layer (CdTe) increases, the optical path for incident photons within the material is increased and more photons are absorbed by the material, leading to a higher generation rate of electron-hole pairs. This can increase J_{SC} as more current is generated under illumination. Moreover, increased generation can reduce surface and interface recombination, leading to improved V_{OC}. Finally, maximizing light absorption and minimizing carrier recombination contributes to an improved *FF*. According to Eq. 1.4, *PCE* will be increased with the increment of absorber layer thickness.

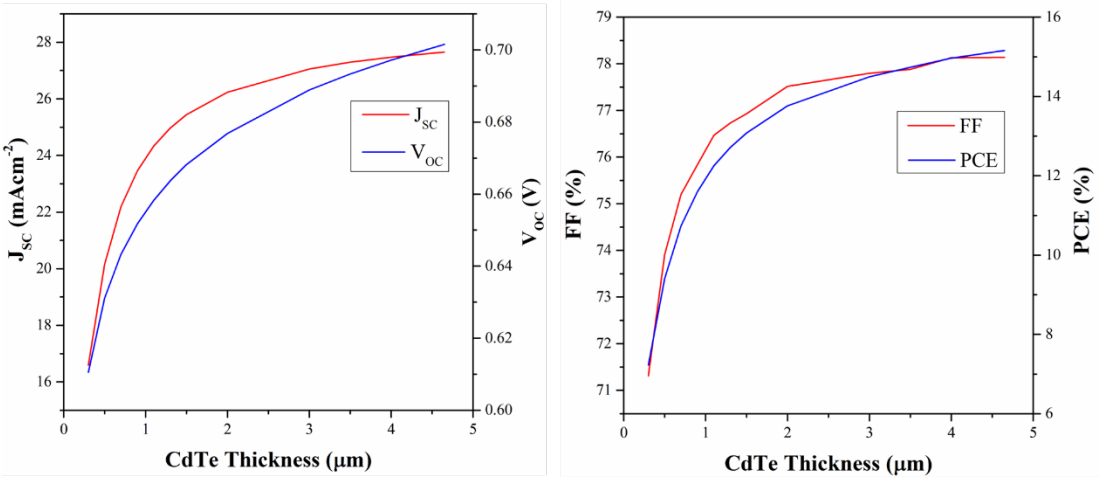

Fig. 3.7: The performance of device with the thickness of CdTe absorber layer

The improvement of the photon absorption with the increment of absorber layer (CdTe) thickness can be explained by the Quantum Efficiency (QE) diagram. The QE of a solar cell represents the fraction of incident photons converted into electrical current. According to Fig. 3.8, as the thickness increases, the portion of photons converted into electrical current goes high. Therefore, absorption should be enhanced with the thickness of the CdTe layer.

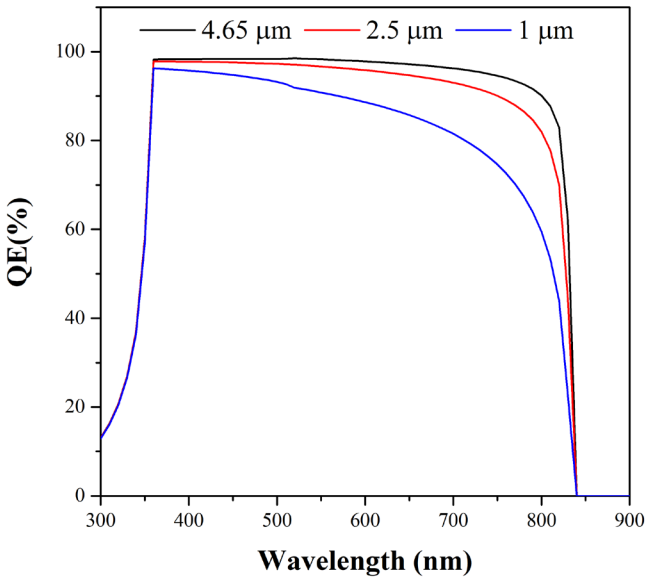

Fig. 3.8: Variation of quantum efficiency (QE) of the device w.r.t CdTe thickness

In the second-generation solar cells and this laboratory-developed device, the problem is associated with efficiency. As discussed earlier, enhancing the device performance with the increment of absorber layer thickness is possible. However, when the absorber layer thickness improves, the manufacturing cost will rise because higher thickness means higher material cost, deposition time, and energy consumption. The cost of second-generation solar cells should be lowered compared to first-generation solar cells. Therefore, it should be necessary to find an efficiency enhancement technique for the cell structure that can enhance efficiency while lowering the cost of manufacturing.

In chapter 2, the effectivity of AR coating was discussed, and that can be employed outside of the device structure. In section 3.3.3, the SnS BSF layer will be introduced with the absorber layer and back contact.

3.3.3 Introduction of SnS BSF layer for CdS/CdTe solar cell

Fig. 3.9 illustrates the Software interpretation of the solar cell with the BSF layer. At the initial stage, the thickness of the CdTe was kept at 4.65 µm. The doping concentration of the SnS layer was initialized as 1 x 10^{18} cm^{-3}, while the CdTe doping concentration was maintained at 1 x 10^{17} cm^{-3}. The thickness of the SnS layer was maintained at 0.1 µm, which was an ultra-thin layer compared to the CdTe layer. Moreover, bandgap, electron affinity and dielectric permittivity were set as 1.25 eV, 4.2 eV and 12.5 eV, respectively. Additionally, a new interface of SnS/CdTe was added to the structure.

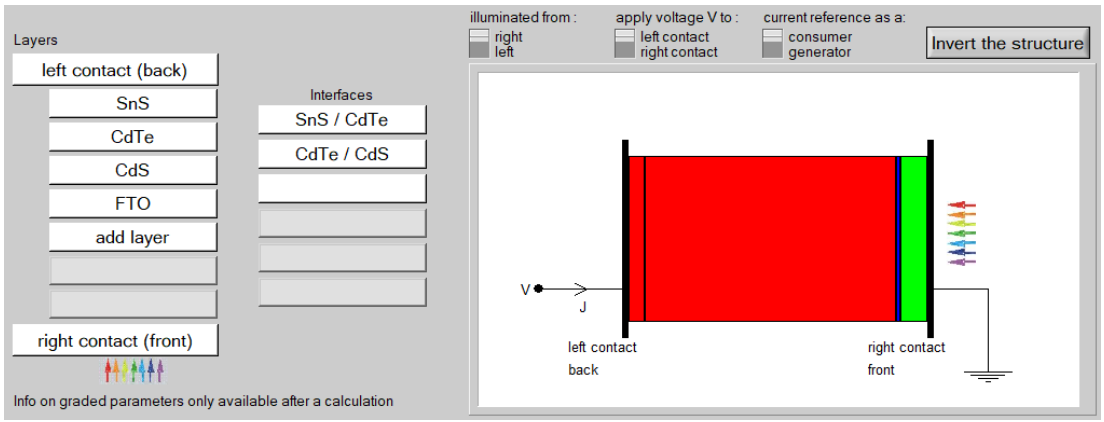

Fig. 3.9: Software interpretation of the solar cell with BSF layer

The simulated J-V characteristic curves of reference strucure (simulation of laboratory developed solar cell) and proposed structure (solar cell with BSF layer) are shown in Fig. 3.10. The *J_{SC}, V_{OC}, FF, and PCE* of the reference structure and solar cell with BSF layer were 27.7 mAcm^{-2}, 0.71 V, 77.8%, 15.2% and 29 mAcm^{-2}, 0.89 V, 80.7%, 20.9%, respectively. A lower rate of carrier recombination and more effective carrier collection reduce losses and enhance the overall current-voltage characteristics of the solar cell, as shown in Fig. 3.10.

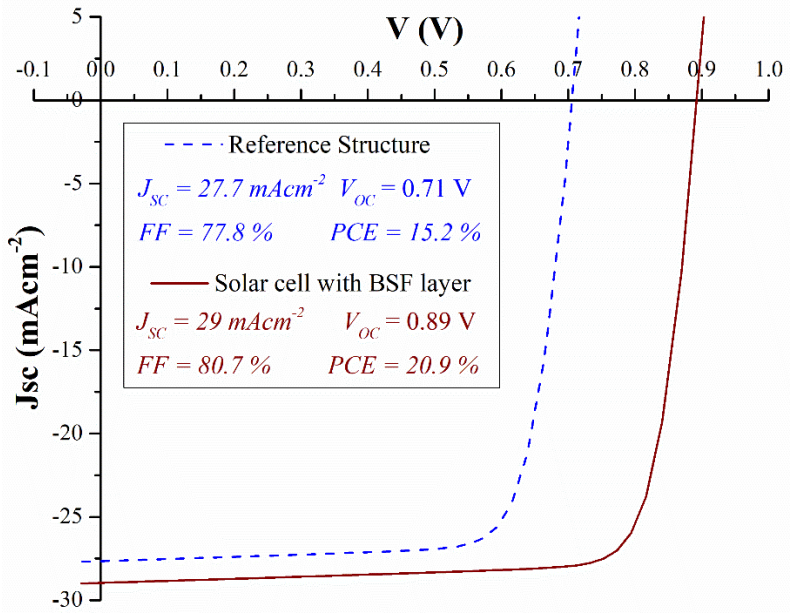

Fig. 3.10: J-V characteristic curves of reference structure and solar cell with BSF layer

As discussed in section 1.6.1, the BSF layer acts as charge extraction layer while promoting exciton dissociation and that helps for minimizing recombination. Fig. 3.11 shows the recombination current curves of reference structure and the solar cell with BSF layer. The figure illustrates a noticeable reduction in recombination current after adding the BSF layer. This reduction in recombination losses leads to a higher V_{OC}. Moreover, as this electric field encourages efficient carrier collection, especially at the rear surface, it contributes to a higher J_{SC} as more charge carriers are effectively

collected and contribute to the current. The reduction in rear surface recombination losses and the improved carrier collection efficiency contribute to a higher fill factor. The combined effect of increased V_{OC}, J_{SC}, and FF results in an overall improvement in the efficiency of the solar cell.

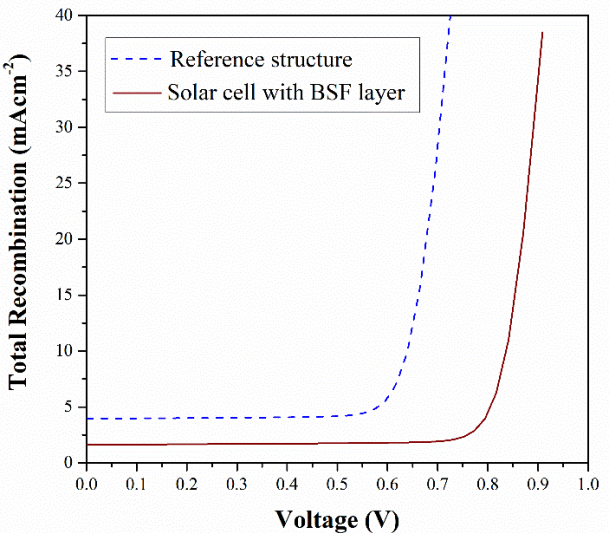

Fig. 3.21: The recombination current curves of reference structure and the solar cell with BSF layer

Henceforward, the impact of the SnS BSF layer on the performance of solar cells will be investigated. According to Fig. 3.7 and 3.12 all solar cell parameters show improvement at each CdTe thickness. Table 3.2 depicts the comparison of reference and proposed solar cell with respect to the CdTe thickness.

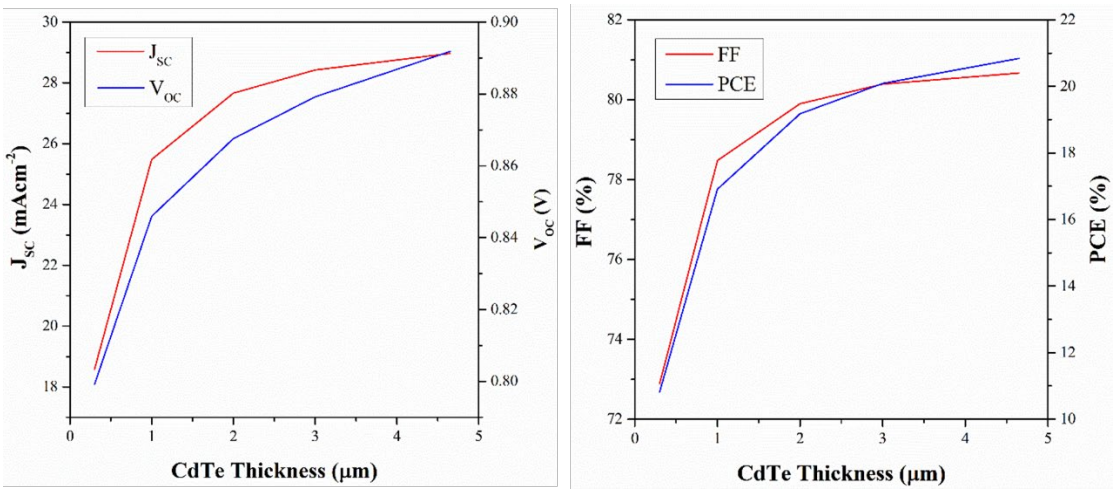

Fig. 3.12: The performance of proposed solar cell with the thickness of CdTe absorber layer

TABLE 3.2: COMPARISON OF REFERENCE AND PROPOSED SOLAR CELL WITH RESPECT TO THE CdTe THICKNESS

CdTe Thickness (µm)		J_{SC} ($mAcm^2$)	V_{OC} (V)	FF (%)	PCE (%)
0.3	Reference	16.6	0.61	71.3	7.2
	Proposed	18.6	0.80	72.9	10.8
1	Reference	24.3	0.66	76.5	12.3
	Proposed	25.5	0.85	78.5	16.9
2	Reference	26.2	0.68	77.5	13.8
	Proposed	27.7	0.87	79.9	19.2
3	Reference	27.1	0.69	77.8	14.5
	Proposed	28.4	0.88	80.4	20.1
4.65	Reference	27.7	0.70	78.1	15.2
	Proposed	29.0	0.89	80.7	20.8

According to Table 3.2, the efficiency of the reference cell with a 4.65 µm thick absorber layer is 15.2%, while the proposed cell with a 3 µm thick absorber layer and 0.1 µm thick BSF layer can reach more than 20% efficiency. Therefore, the addition of a BSF layer next to the absorber layer would be a possible and better approach to improve the device's performance.

Additionally, the enhancement of electrical properties of the proposed solar cell compared to the reference cell are shown in Table 3.3.

TABLE 3.3: ENHANCEMENT OF THE ELECTRICAL PARAMETERS OF PROPOSED SOLAR CELL WITH RESPECT TO THE REFERENCE CELL

CdTe Thickness (µm)	Improvement			
	J_{SC} (%)	V_{OC} (%)	FF (%)	PCE (%)
0.3	12.0	31.1	2.2	50.0
1	4.9	28.8	2.6	37.4
2	5.7	27.9	3.1	39.1
3	4.8	27.5	3.3	38.6
4.65	4.7	27.1	3.3	36.8

Using table 3.3, the average enhancement of J_{SC}, V_{OC}, *FF,* and *PCE* can be obtained as 5%, 27.9%, 3.1% and 38%, respectively. Note that the average value of each parameter is calculated using best fitted values (expect the parameters of solar cell with 0.3 µm CdTe thickness) in the table 3.3. Moreover, it should be mentioned that there can be slight variation of these results upon fabrication of the device as mentioned in section 3.3.1.

3.4 Summary

In this chapter, a simulation study of laboratory-developed solar cells was conducted, and a comparison of the simulated and experimental data was obtained. The main reason identified for the difference between simulated and experimental data was the possibility of the defect state in the CdTe absorber layer in the lab experiment. It would lead to higher short circuit current density than the theoretical value. In the next stage, recombination at the back surface of the solar cell was considered. The best possible solution was positioning the SnS BSF layer between the absorber layer and the back contact layer. This study was conducted via a simulation study, and the results showed that 38% (average) PCE can be obtained through the addition of BSF layer. Moreover, the possibility of a deposition environment for the SnS layer was identified via a literature review. As a result, by introducing the BSF layer, the thickness of the CdTe layer could be reduced, and that would ultimately reduce the cost of manufacturing.

CHAPTER 4

CONCLUSIONS

In conclusion, first-generation solar cells, mainly compromised with crystalline silicon, have been dominant in the solar industry for many years. On the other hand, second-generation solar cells, represented by thin-film technologies, offer flexibility in design and potential cost advantages. However, compared to the first-generation and second-generation solar cells, the power conversion efficiency of the first generation of crystalline silicon still leads. The main reason behind the low efficiency of thin film solar cells is lower broadband light absorption, which is caused by reflection at the front surface of the device and the recombination at the back surface of the absorber layer. In this research, the CdTe laboratory developed solar cells, and SCAPS-1D simulation software was selected for the experiments and simulations, respectively.

In the study, a ZnO AR coating was proposed to reduce the reflection at the front surface. The optimal condition for the growth of ZnO AR coating using the spin coating technique was identified as 3000 rpm for 15 s using the zinc acetate precursor dissolved in methanol. Furthermore, minimal reflectance (2.5%) and surface roughness (11.44 nm) confirmed the suitability of the growth ZnO as an AR coating. Additionally, after introducing the optimized ZnO AR coating, the overall current density and power conversion efficiency of the laboratory developed CdS/CdTe solar cells were enhanced by 6.7% and 9.0%, respectively. Therefore, the spin coated ZnO is an ideal AR coating for the CdS/CdTe solar cell devices.

Then, a simulation study was conducted for laboratory-developed solar cells using a measured data set. Through that, SCAPS-1D simulation software was validated. The major variation of the simulated and experimented data was short circuit current density, and therein, the experimental value shows a higher value than the theoretical value. The possible reason for that might be defects at the CdTe layer. According to the literature, it would be better to perform a "Photoluminescence" experiment to analyze the emission and excitation spectrum of the CdS/CdTe sample and identify the defect states.

Afterward, to reduce the recombination at the back surface of the CdTe/metal interface, the SnS BSF layer was proposed. It ensured that using a highly doped (1 x 10^{18} cm^{-3}) ultrathin SnS layer (0.1 µm) enables the reduction of the thickness of the CdTe absorber layer and the development of a highly efficient thin-film. The results showed that the average values of J_{SC}, V_{OC}, *FF,* and *PCE* can be improved by 5%, 27.9%, 3.1% and 38%, respectively.

To conclude, this study on designing and developing high-efficiency thin-film solar cells through enhanced broadband light absorption highlights the importance of innovation in making solar cells more efficient and sustainable. By improving anti-reflective coatings and designing better back-surface field layers, this work helps improve solar technology locally. The firstly designed Sri Lankan prototype CdTe thin

film Solar panels were exhibited in February 2024 by University of Kelaniya and University of Peradeniya. Therefore, future challenges for students continuing this work will include identifying the proper fabrication processes and material optimization required for BSF layers, as well as integrating these advancements into practical prototype solar cells.

REFERENCES

[1] "Energy Explained - U.S. Energy Information Administration (EIA)." Accessed: Jul. 28, 2024. [Online]. Available: https://www.eia.gov/energyexplained/

[2] "Energy Sources | Department of Energy." Accessed: Jul. 28, 2024. [Online]. Available: https://www.energy.gov/energy-sources

[3] "Energy demand: Three drivers | ExxonMobil." Accessed: Sep. 07, 2023. [Online]. Available: https://corporate.exxonmobil.com/what-we-do/energy-supply/global-outlook/energy-demand

[4] "Executive summary – World Energy Outlook 2022 – Analysis - IEA." Accessed: Sep. 08, 2023. [Online]. Available: https://www.iea.org/reports/world-energy-outlook-2022/executive-summary

[5] C. H. Moris, M. T. C. Guevara, A. Salmon, and A. Lorca, "Comparison between concentrated solar power and gas-based generation in terms of economic and flexibility-related aspects in chile," *Energies*, vol. 14, no. 4, Feb. 2021, doi: 10.3390/EN14041063.

[6] A. Coomaraswamy Mawatha and S. Lanka, "Sri Lanka Sustainable Energy Authority," 2019.

[7] "Sri Lanka | Climate Promise." Accessed: Sep. 08, 2023. [Online]. Available: https://climatepromise.undp.org/what-we-do/where-we-work/sri-lanka

[8] "Sooriyabala Sangaramaya | Sri Lanka Sustainable Energy Authority." Accessed: Sep. 08, 2023. [Online]. Available: https://www.energy.gov.lk/en/soorya-bala-sangramaya

[9] "Recycling | First Solar." Accessed: Jul. 28, 2024. [Online]. Available: https://www.firstsolar.com/en/Solutions/Recycling

[10] "Inzicht in Spectra van de Aarde." Accessed: Sep. 08, 2023. [Online]. Available: https://seos-project.eu/earthspectra/earthspectra-c02-p12.nl.html

[11] V. Malgras, A. Nattestad, J. H. Kim, S. X. Dou, and Y. Yamauchi, "Understanding chemically processed solar cells based on quantum dots," *Sci. Technol. Adv. Mater.*, vol. 18, no. 1, pp. 334–350, 2017, doi: 10.1080/14686996.2017.1317219.

[12] "Solar cell evolution: Past, present, future | Electronics360." Accessed: Sep. 09, 2023. [Online]. Available: https://electronics360.globalspec.com/article/15210/solar-cell-evolution-past-present-future

[13] "Best Research-Cell Efficiency Chart | Photovoltaic Research | NREL." Accessed: Sep. 10, 2023. [Online]. Available: https://www.nrel.gov/pv/cell-efficiency.html

[14] T. Saga, “Advances in crystalline silicon solar cell technology for industrial mass production,” *NPG Asia Mater.*, vol. 2, no. 3, pp. 96–102, Jul. 2010, doi: 10.1038/asiamat.2010.82.

[15] J. Pastuszak and P. Węgierek, “Photovoltaic Cell Generations and Current Research Directions for Their Development,” *Materials (Basel).*, vol. 15, no. 16, p. 5542, Aug. 2022, doi: 10.3390/ma15165542.

[16] K. L. Chopra, P. D. Paulson, and V. Dutta, “Thin-film solar cells: An overview,” *Prog. Photovoltaics Res. Appl.*, vol. 12, no. 2–3, pp. 69–92, 2004, doi: 10.1002/pip.541.

[17] M. A. Scarpulla *et al.*, “CdTe-based thin film photovoltaics: Recent advances, current challenges and future prospects,” *Sol. Energy Mater. Sol. Cells*, vol. 255, p. 112289, Jun. 2023, doi: 10.1016/j.solmat.2023.112289.

[18] S. Karthikeyan and P. Thirunavukkarasu, “Evolution of Amorphous-Si , CIGS and CdTe Solar Thin Films With a Comparative Market Analysis and Reliability Measures,” vol. 8, no. 2, pp. 1633–1646, 2019.

[19] N. Shah *et al.*, “A Review of Third Generation Solar Cells,” *Processes*, vol. 11, no. 6, p. 1852, 2023, doi: 10.3390/pr11061852.

[20] Y. Da and Y. Xuan, “Role of surface recombination in affecting the efficiency of nanostructured thin-film solar cells,” *Opt. Express*, vol. 21, no. S6, p. A1065, Nov. 2013, doi: 10.1364/OE.21.0A1065.

[21] A. ur Rehman *et al.*, “Development and prospects of surface passivation schemes for high-efficiency c-Si solar cells,” *Sol. Energy*, vol. 166, pp. 90–97, May 2018, doi: 10.1016/j.solener.2018.03.025.

[22] B. Barman and P. K. Kalita, “Influence of back surface field layer on enhancing the efficiency of CIGS solar cell,” *Sol. Energy*, vol. 216, no. October 2020, pp. 329–337, 2021, doi: 10.1016/j.solener.2021.01.032.

[23] “Anti Reflective Coating | A Brief History of AR Coatings.” Accessed: Sep. 24, 2023. [Online]. Available: https://diamondcoatings.co.uk/brief-history-anti-reflective-coatings/

[24] D. Kc, D. K. Shah, A. M. Alanazi, and M. S. Akhtar, “Impact of Different Antireflection Layers on Cadmium Telluride (CdTe) Solar Cells: a PC1D Simulation Study,” *J. Electron. Mater.*, vol. 50, no. 4, pp. 2199–2205, 2021, doi: 10.1007/s11664-020-08696-5.

[25] R. Sharma, A. Gupta, and A. Virdi, “Effect of single and double layer antireflection coating to enhance photovoltaic efficiency of silicon solar,” *J. Nano- Electron. Phys.*, vol. 9, no. 2, pp. 4–7, 2017, doi: 10.21272/jnep.9(2).02001.

[26] U. Gangopadhyay, K. Kim, D. Mangalaraj, and J. Yi, “Low cost CBD ZnS antireflection coating on large area commercial mono-crystalline silicon solar cells,” *Appl. Surf. Sci.*, vol. 230, no. 1–4, pp. 364–370, 2004, doi:

10.1016/j.apsusc.2004.02.059.

[27] A. T. Salih, A. A. Najim, M. A. H. Muhi, and K. R. Gbashi, "Single-material multilayer ZnS as anti-reflective coating for solar cell applications," *Opt. Commun.*, vol. 388, no. December, pp. 84–89, 2017, doi: 10.1016/j.optcom.2016.12.035.

[28] M. Li, H. Shen, L. Zhuang, D. Chen, and X. Liang, "SiO2antireflection coatings fabricated by electron-beam evaporation for black monocrystalline silicon solar cells," *Int. J. Photoenergy*, vol. 2014, 2014, doi: 10.1155/2014/670438.

[29] W. Zhang, J. Tu, W. Long, W. Lai, Y. Sheng, and T. Guo, "Preparation of SiO2 anti-reflection coatings by sol-gel method," *Energy Procedia*, vol. 130, pp. 72–76, 2017, doi: 10.1016/j.egypro.2017.09.398.

[30] J.-Y. Wang, C.-S. Huang, S.-L. Ou, Y.-S. Cho, and J.-J. Huang, "One-step preparation of TiO2 anti-reflection coating and cover layer by liquid phase deposition for monocrystalline Si PERC solar cell," *Sol. Energy Mater. Sol. Cells*, vol. 234, p. 111433, Jan. 2022, doi: 10.1016/j.solmat.2021.111433.

[31] R. Sagar and A. Rao, "Increasing the silicon solar cell efficiency with transition metal oxide nano-thin films as anti-reflection coatings," *Mater. Res. Express*, vol. 7, no. 1, 2020, doi: 10.1088/2053-1591/ab6ad5.

[32] K. A. Salman, K. Omar, and Z. Hassan, "Improved performance of a crystalline silicon solar cell based on ZnO/PS anti-reflection coating layers," *Superlattices Microstruct.*, vol. 50, no. 5, pp. 517–528, 2011, doi: 10.1016/j.spmi.2011.08.014.

[33] S.-H. Yi, S.-K. Choi, J.-M. Jang, J.-A. Kim, and W.-G. Jung, "Low-temperature growth of ZnO nanorods by chemical bath deposition," *J. Colloid Interface Sci.*, vol. 313, no. 2, pp. 705–710, Sep. 2007, doi: 10.1016/j.jcis.2007.05.006.

[34] N. B. Patil, A. R. Nimbalkar, and M. G. Patil, "ZnO thin film prepared by a sol-gel spin coating technique for NO 2 detection," *Mater. Sci. Eng. B*, vol. 227, pp. 53–60, Jan. 2018, doi: 10.1016/j.mseb.2017.10.011.

[35] D. Time *et al.*, "Controlling the Layer Thickness of Zinc Oxide Photoanode and," pp. 1–16, 2023.

[36] O. A. Azeez, R. S. Sabry, M. A. M. Hassan, and S. F. Madlul, "Synthesis and characteristics of screen printed ZnO thick films nanostructures grown using different methods," *J. Mater. Sci. Mater. Electron.*, vol. 26, no. 6, pp. 4051–4061, Jun. 2015, doi: 10.1007/s10854-015-2944-0.

[37] A. M. Alsaad, Q. M. Al-Bataineh, A. A. Ahmad, Z. Albataineh, and A. Telfah, "Optical band gap and refractive index dispersion parameters of boron-doped ZnO thin films: A novel derived mathematical model from the experimental transmission spectra," *Optik (Stuttg).*, vol. 211, p. 164641, Jun. 2020, doi: 10.1016/J.IJLEO.2020.164641.

[38] K. Ellmer, A. Klein, and B. Rech, Eds., *Transparent Conductive Zinc Oxide*,

vol. 104. in Springer Series in Materials Science, vol. 104. Berlin, Heidelberg: Springer Berlin Heidelberg, 2008. doi: 10.1007/978-3-540-73612-7.

[39] N. B. Patil, A. R. Nimbalkar, and M. G. Patil, "ZnO thin film prepared by a sol-gel spin coating technique for NO2 detection," *Mater. Sci. Eng. B*, vol. 227, no. 2, pp. 53–60, 2018, doi: 10.1016/j.mseb.2017.10.011.

[40] S. A. Kamaruddin, K. Y. Chan, H. K. Yow, M. Zainizan Sahdan, H. Saim, and D. Knipp, "Zinc oxide films prepared by sol-gel spin coating technique," *Appl. Phys. A Mater. Sci. Process.*, vol. 104, no. 1, pp. 263–268, 2011, doi: 10.1007/s00339-010-6121-2.

[41] Mursal, Irhamni, Bukhari, and Z. Jalil, "Structural and Optical Properties of Zinc Oxide (ZnO) based Thin Films Deposited by Sol-Gel Spin Coating Method," *J. Phys. Conf. Ser.*, vol. 1116, no. 3, 2018, doi: 10.1088/1742-6596/1116/3/032020.

[42] M. Smirnov, C. Baban, and G. I. Rusu, "Structural and optical characteristics of spin-coated ZnO thin films," *Appl. Surf. Sci.*, vol. 256, no. 8, pp. 2405–2408, 2010, doi: 10.1016/j.apsusc.2009.10.075.

[43] T. Amakali, L. S. Daniel, V. Uahengo, N. Y. Dzade, and N. H. De Leeuw, "Structural and Optical Properties of ZnO Thin Films Sol – Gel Methods," *Crystals*, vol. 10(2), p. 132, 2020.

[44] G. Womack, K. Isbilir, F. Lisco, G. Durand, A. Taylor, and J. M. Walls, "The performance and durability of single-layer sol-gel anti-reflection coatings applied to solar module cover glass," *Surf. Coatings Technol.*, vol. 358, no. October 2018, pp. 76–83, 2019, doi: 10.1016/j.surfcoat.2018.11.030.

[45] A. Kowsar, "Comparative Study on Solar Cell Simulators," pp. 23–24, 2019.

[46] K. C. Devendra *et al.*, "Numerical investigation of graphene as a back surface field layer on the performance of cadmium telluride solar cell," *Molecules*, vol. 26, no. 11, pp. 1–10, 2021, doi: 10.3390/molecules26113275.

[47] V. Shukla and G. Panda, "Effect of BSF layer on the performance of CdTe solar cell," *Mater. Today Proc.*, vol. 44, pp. 2300–2303, 2021, doi: 10.1016/j.matpr.2020.12.394.

[48] A. Haddout, A. Raidou, and M. Fahoume, "Influence of the layer parameters on the performance of the CdTe solar cells," *Optoelectron. Lett.*, vol. 14, no. 2, pp. 98–103, Mar. 2018, doi: 10.1007/s11801-018-7229-4.

[49] S. R. I. Biplab, M. H. Ali, M. M. A. Moon, M. F. Pervez, M. F. Rahman, and J. Hossain, "Performance enhancement of CIGS-based solar cells by incorporating an ultrathin BaSi2 BSF layer," *J. Comput. Electron.*, vol. 19, no. 1, pp. 342–352, 2020, doi: 10.1007/s10825-019-01433-0.

[50] N. Amin, K. Sopian, and M. Konagai, "Numerical modeling of CdS/CdTe and CdS/CdTe/ZnTe solar cells as a function of CdTe thickness," *Sol. Energy Mater. Sol. Cells*, vol. 91, no. 13, pp. 1202–1208, 2007, doi:

10.1016/j.solmat.2007.04.006.

[51] N. Amin, T. Isaka, A. Yamada, and M. Konagai, “Highly efficient 1μm thick CdTe solar cells with textured TCOs,” *Sol. Energy Mater. Sol. Cells*, vol. 67, no. 1–4, pp. 195–201, Mar. 2001, doi: 10.1016/S0927-0248(00)00281-6.

[52] S. Benabbas, Z. Rouabah, N. Bouarissa, and N. Chelali, “The role of back surface field SnS layer in improvement of efficiency of CdTe thin film solar cells,” *Optik (Stuttg).*, vol. 127, no. 15, pp. 6210–6217, Aug. 2016, doi: 10.1016/j.ijleo.2016.04.050.

[53] X. Yang, B. Chen, J. Chen, Y. Zhang, W. Liu, and Y. Sun, “ZnS thin film functionalized as back surface field in Si solar cells,” *Mater. Sci. Semicond. Process.*, vol. 74, no. April 2017, pp. 309–312, 2018, doi: 10.1016/j.mssp.2017.08.011.

[54] Y. Liu, Y. Sun, W. Liu, and J. Yao, “Novel high-efficiency crystalline-silicon-based compound heterojunction solar cells: HCT (heterojunction with compound thin-layer),” *Phys. Chem. Chem. Phys.*, vol. 16, no. 29, pp. 15400–15410, 2014, doi: 10.1039/C4CP00668B.

[55] A. Kaminski *et al.*, “Aluminium BSF in silicon solar cells,” *Sol. Energy Mater. Sol. Cells*, vol. 72, no. 1–4, pp. 373–379, Apr. 2002, doi: 10.1016/S0927-0248(01)00185-4.

[56] L. D. S. Yadav, “Ultraviolet (UV) and Visible Spectroscopy,” in *Organic Spectroscopy*, Dordrecht: Springer Netherlands, 2005, pp. 7–51. doi: 10.1007/978-1-4020-2575-4_2.

[57] “PVE300 Photovoltaic EQE (IPCE) and IQE solution - Bentham Instruments.” Accessed: Oct. 12, 2023. [Online]. Available: https://www.bentham.co.uk/products/systems/pve300-photovoltaic-eqe-ipce-and-iqe-solution-16/

[58] “DTR6 Integrating Sphere (300-2000nm) - Bentham Instruments.” Accessed: Oct. 12, 2023. [Online]. Available: https://www.bentham.co.uk/products/components/dtr6-integrating-sphere-300-2000nm-100/

[59] “Scanning Electron Microscopy | Nanoscience Instruments.” Accessed: Dec. 07, 2023. [Online]. Available: https://www.nanoscience.com/techniques/scanning-electron-microscopy/

[60] “Principles of Operation: Stylus Profiler — Australia Surface Metrology Lab.” Accessed: Oct. 13, 2023. [Online]. Available: https://australiasurfacemetrologylab.org/new-page

[61] “MST | [SEM-EDX] Energy Dispersive X-ray Spectroscopy (SEM).” Accessed: Oct. 13, 2023. [Online]. Available: https://www.mst.or.jp/Portals/0/en/en_sem-edx.htm

[62] T. A. Gessert, R. G. Dhere, J. N. Duenow, J. V. Li, S. E. Asher, and M. R.

Young, “Comparison of CdS/CdTe superstrate and substrate devices fabricated with a ZnTe:Cu contact interface,” in *2010 35th IEEE Photovoltaic Specialists Conference*, IEEE, Jun. 2010, pp. 000335–000339. doi: 10.1109/PVSC.2010.5616922.

[63] G. K. U. P. Gajanayake, A. A. I. Lakmal, D. S. M. De Silva, and B. S. Dassanayake, “Chemical Bath Deposited CdS Along with Electrodeposited and Closed Space Sublimated CdTe for Solar Cell Fabrication,” 2022, pp. 7–12. doi: 10.1007/978-981-16-9280-2_2.

[64] G. K. U. P. Gajanayake, D. S. M. De Silva, and H. Y. R. Atapattu, “Altering NH4OH concentration in producing chemical bath deposited CdS to steadily support electrodeposited CdTe,” *Mater. Sci. Eng. B*, vol. 265, no. April 2020, p. 114952, 2021, doi: 10.1016/j.mseb.2020.114952.

[65] G. K. U. P. Gajanayake, A. A. I. Lakmal, D. S. M. De Silva, and B. S. Dassanayake, “Effect of CdTe nucleation layer on the performance of CdS/CdTe thin film solar cells,” *J. Mater. Sci. Mater. Electron.*, vol. 34, no. 6, p. 508, Feb. 2023, doi: 10.1007/s10854-023-09895-6.

[66] “PC1D | PVEducation.” Accessed: Nov. 01, 2023. [Online]. Available: https://www.pveducation.org/pvcdrom/welcome-to-pvcdrom/pc1d

[67] B. Ganesh, K. Y. Rani, B. Satyavathi, and K. S. K. R. Patnaik, “Experimental analysis in different batch operating units for process intensification: methyl acetate production case study,” *Int. J. Ind. Chem.*, vol. 5, no. 3–4, pp. 85–93, Dec. 2014, doi: 10.1007/s40090-014-0023-7.

[68] V. N. Jafarova and G. S. Orudzhev, “Structural and electronic properties of ZnO: A first-principles density-functional theory study within LDA(GGA) and LDA(GGA)+U methods,” *Solid State Commun.*, vol. 325, p. 114166, Feb. 2021, doi: 10.1016/j.ssc.2020.114166.

[69] T. A. Saleh, “Overview of surface and interface science,” *Interface Sci. Technol.*, vol. 34, pp. 1–38, Jan. 2022, doi: 10.1016/B978-0-12-849876-7.00001-4.

[70] K. Decock, A. Niemegeers, and J. Verschraegen, “SCAPS manual.” Accessed: Nov. 01, 2023. [Online]. Available:https://scaps.elis.ugent.be/SCAPS%20manual%20most%20recent.pdf.

[71] A. M. M. Ul Akhir and M. T. Imam, “Numerical Simulation of an Improved CZTS/WS2 PV Cell by SCAPS 1-D,” *GUB J. Sci. Eng.*, vol. 8, no. 1, pp. 41–48, Nov. 2022, doi: 10.3329/gubjse.v8i1.62331.

[72] H. Dang, E. Ososanya, N. Zhang, and V. Singh, “Numerical modeling and simulation of stable nanowire CdS-CdTe solar cells,” in *2017 IEEE 17th International Conference on Nanotechnology (IEEE-NANO)*, IEEE, Jul. 2017, pp. 171–176. doi: 10.1109/NANO.2017.8117357.

[73] S. Ahmmed, A. Aktar, M. F. Rahman, J. Hossain, and A. B. M. Ismail, “A numerical simulation of high efficiency CdS/CdTe based solar cell using NiO

HTL and ZnO TCO," *Optik (Stuttg).*, vol. 223, p. 165625, Dec. 2020, doi: 10.1016/j.ijleo.2020.165625.

[74] B. Z. Bhari, K. S. Rahman, P. Chelvanathan, and M. A. Ibrahim, "Numerical Simulation of Ultrathin CdTe Solar Cell by SCAPS-1D," *IOP Conf. Ser. Mater. Sci. Eng.*, vol. 1278, no. 1, p. 012002, Feb. 2023, doi: 10.1088/1757-899X/1278/1/012002.

[75] D. Parashar, V. S. G. Krishna, S. N. Moger, R. Keshav, and M. G. Mahesha, "Thickness Optimization of ZnO/CdS/CdTe Solar Cell by Numerical Simulation," *Trans. Electr. Electron. Mater.*, vol. 21, no. 6, pp. 587–593, Dec. 2020, doi: 10.1007/s42341-020-00209-9.

[76] H. Dang, E. Ososanya, N. Zhang, and V. Singh, "Numerical modeling and simulation of stable nanowire CdS-CdTe solar cells," in *2017 IEEE 17th International Conference on Nanotechnology (IEEE-NANO)*, IEEE, Jul. 2017, pp. 171–176. doi: 10.1109/NANO.2017.8117357.

[77] V. K. Arepalli, Y. Shin, and J. Kim, "Influence of working pressure on the structural, optical, and electrical properties of RF-sputtered SnS thin films," *Superlattices Microstruct.*, vol. 122, pp. 253–261, Oct. 2018, doi: 10.1016/j.spmi.2018.08.001.

[78] T. D. Nguyen *et al.*, "Synthesis of Ag-embedded SnS films by the RF method for photovoltaic applications," *Surfaces and Interfaces*, vol. 25, p. 101151, Aug. 2021, doi: 10.1016/j.surfin.2021.101151.

[79] J. Y. Cho, S. Sinha, M. G. Gang, and J. Heo, "Controlled thickness of a chemical-bath-deposited CdS buffer layer for a SnS thin film solar cell with more than 3% efficiency," *J. Alloys Compd.*, vol. 796, pp. 160–166, Aug. 2019, doi: 10.1016/j.jallcom.2019.05.035.

[80] J. Vidal *et al.*, "Band-structure, optical properties, and defect physics of the photovoltaic semiconductor SnS," *Appl. Phys. Lett.*, vol. 100, no. 3, Jan. 2012, doi: 10.1063/1.3675880.

[81] I. Ammar, A. Gassoumi, A. Akkari, F. Delpech, S. Ammar, and N. Turki-Kamoun, "Deposition of SnS thin films by chemical bath deposition method: Effect of surfactants," *Eur. Phys. J. Plus*, vol. 134, no. 10, p. 505, Oct. 2019, doi: 10.1140/epjp/i2019-12976-3.

[82] H. Kafashan, M. Azizieh, and H. Nasiri Vatan, "Ultrasound-assisted electrodeposition of SnS: Effect of ultrasound waves on the physical properties of nanostructured SnS thin films," *J. Alloys Compd.*, vol. 686, pp. 962–968, Nov. 2016, doi: 10.1016/j.jallcom.2016.06.201.

[83] T. Garmim *et al.*, "Optical, electrical and electronic properties of SnS thin films deposited by sol gel spin coating technique for photovoltaic applications," *J. Mater. Sci. Mater. Electron.*, vol. 31, no. 23, pp. 20730–20741, Dec. 2020, doi: 10.1007/s10854-020-04586-y.

[84] F. Aslan, F. Arslan, A. Tumbul, and A. Goktas, "Synthesis and characterization

of solution processed p-SnS and n-SnS2 thin films: Effect of starting chemicals," *Opt. Mater. (Amst).*, vol. 127, p. 112270, May 2022, doi: 10.1016/j.optmat.2022.112270.

[85] R. M. Geisthardt, M. Topic, and J. R. Sites, "Status and Potential of CdTe Solar-Cell Efficiency," *IEEE J. Photovoltaics*, vol. 5, no. 4, pp. 1217–1221, Jul. 2015, doi: 10.1109/JPHOTOV.2015.2434594.

[86] M. Isah *et al.*, "Exploring the impact of defect energy levels in CdTe/Si dual-junction solar cells using wxAMPS," *Sci. Rep.*, vol. 14, no. 1, p. 4804, Feb. 2024, doi: 10.1038/s41598-024-55616-2.